Assessment and Improvement of Current Computational Spark Ignition Engine NOx Formation Models for Auto Industry Development and Design Use

by

Patia Jean McGrath

B. S. Mechanical Engineering, Columbia University, 1993.
S. M. Aeronautics and Astronautics, Massachusetts Institute of Technology, 1995.

Submitted in Partial Fulfillment of the Requirements for the Degree of

Mechanical Engineer

at the

MASSACHUSETTS INSTITUTE OF TECHNOLOGY

November 1996
[February 1997]

Author ..... Patia J. McGrath .....
Department of Mechanical Engineering
November 27, 1996

Certified by ..... John B. Heywood .....
Professor John B. Heywood
Sun Jae Professor of Mechanical Engineering

Accepted by ....
Professor Ain A. Sonin
Chairman, Department Graduate Committee

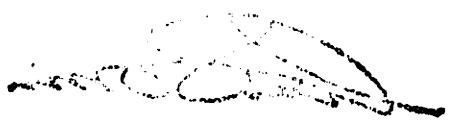

Assessment and Improvement of Current Computational Spark Ignition Engine NOx Formation Models for Auto Industry Development and Design Use

by

Patia Jean McGrath

The objective of this thesis is to assess where current simulation codes which predict NOx formation in spark-ignition engines are deficient when used in engine design and how they can be improved. Such computational codes increasingly are used as predictive design tools for automotive manufacturers, enabling engine development and design decisions to be made with greater expediency, fewer experiments, and hence less cost. NOx formation, restricted by stringent Federal regulation, is a crucial issue for the next generation of production engines. Current NOx models are not yet accurate enough to cut development times substantially. The automotive industry requires a NOx generation model that provides accurate, reliable results over the complete range of engine operating conditions.

The two critical factors governing NOx formation are the "thermal state" of the engine in-cylinder burned gases and NOx chemical kinetics. The thermal state is defined by the composition and thermodynamic properties of the in-cylinder gases and is determined by the rate and completeness of the combustion process. Corresponding modeling issues are: combustion chamber crevices and similar mechanisms by which a fraction of the fuel does not burn, the thermal boundary layer that results from heat transfer to the walls, and the sequential or layered charge burning process that flame propagation produces. NOx formation chemistry is modeled through the appropriate set of chemical reactions and their associated rate constants. This thesis evaluates the effects on NOx predictions due to the improvements in the models used for each of these phenomena.

Key to this procedure and unique to this thesis is a significant sensitivity analysis. This sensitivity analysis quantifies the effect of these model improvements and their contributing factors on NOx predictions. The impact of known model uncertainties is assessed; this information is used to recommend how to make these models more practical. Model areas that must be improved are identified and prioritized; these recommendations are critical to the next phase of computational modeling development.

To further illustrate the practical utility of accurate NOx formation models, examples of use in industrial practice are discussed. Automotive manufacturers want these computational tools to play a major role in the engine design process; these tools will reduce the required amount of design prototyping and testing (both being expensive and time consuming) by a significant amount. This thesis discusses engine design and development and explains how these tools can be integrated into and facilitate these processes. Clearly, as these models are more widely used in engine development, their accuracy becomes of critical importance. This thesis work contributes to this essential "design tool development" by identifying those areas where model improvements must be made.

Thesis supervisor: Professor John B. Heywood
Title: Sun Jae Professor of Mechanical Engineering

Acknowledgments

The completion of this thesis would not have been possible without the help of a number of people.

Foremost, I would like to thank Prof. John Heywood for giving me the opportunity to work with him. His exemplary teaching (and patience) made my MIT experience meaningful and worthwhile. Prof. Wai Cheng and Prof. Simone Hochgreb also provided many helpful insights and suggestions.

Karla Stryker and Nancy Cooke deserve special kudos for keeping things running so smoothly.

I would like to thank my friends and officemates in the Sloan Automotive Lab. I am especially grateful to J.R. Linna, Robert Meyer, and Chris O'Brien for their help and kindness.

Sonia Bhambani, Becky Ramer, and Erik Pitchal have known me since the beginning and helped me make it through to the end.

Many thanks to my aunt for the care packages and her concern.

Lastly, I would like to dedicate this thesis to two people: my dad, who provided unwavering support (through hundreds of phone calls); and David Tew, who taught me how to smile again.

Table of Contents

List of Figures

List of Tables

Nomenclature

Roman

A/F	Air/fuel
CO	Carbon Monoxide
E	Internal energy
EGR	Exhaust gas recirculation
h	Specific Enthalpy
HC	Hydrocarbon
m	mass
NOx	Oxides of Nitrogen
p	Pressure
Q	Heat transfer from system
R	Gas constant
SI	Spark-ignition
T	Temperature
t	Time
W	Work done by system

Greek

ϕ Fuel-air equivalence ratio

ρ Density

Superscripts

. d / dt

Subscripts

w Walls

j Stream

1. Introduction

1.1 Background

Recent Federal legislation requires by the year 2001 a nationwide marketing of cars that are to be 60% less polluting than present regulations mandate [36]. This stipulation is the most recent result of an adversarial dialogue between the auto industry and government that began in 1965. As regulations, particularly of emissions, have become increasingly more stringent in the past three decades, significant effects on auto manufacturers -- in terms of product, profit, and corporate strategy -- have followed suit. The task of complying with government standards while fulfilling consumer demands has presented a formidable, unavoidable challenge to the auto industry. Manufacturers feel that a timely, economical response to these measures is possible only through the integration of computational design tools into their engine development processes. This thesis focuses on a crucial part of one of these design tools : nitric oxide formation predictive models in spark-ignition engine cycle simulations.

1.2 Formation of Nitrogen Oxides in Spark-Ignition Engines

The term "nitrogen oxides" (NOx) collectively refers to nitric oxide (NO) and nitrogen dioxide (NO_2). Though both pollutants are irritants and are inherently toxic, they pose their greatest threat as primary participants in smog formation. Automobiles are not the only source of NOx; stationary combustion devices ranging from electricity generation

plants to gas cooking stoves[11] are also responsible for NOx production. However, since autos account for a large fraction of NOx generation, the regulation and control of NOx emissions from vehicles is merited.

The process of NOx formation in the spark-ignition engine cylinder of an automobile can be broken down into several steps (Figure 1.1). The first step is triggered by the ignition of the gases in the engine cylinder by the spark plug. These gases are a compressed mixture of fuel and air (Section 2.3). As the flame front propagates through the unburned mixture across the cylinder, the flame leaves high-temperature combustion products in its wake. NO is formed in these burned gases through a set of kinetic reactions involving the oxygen and nitrogen in the air. At this initial stage, these non-equilibrium reactions are highly temperature dependent. Hotter combustion products will produce larger amounts of NO (Section 2.4). If the reactions were allowed to proceed and reach equilibrium at these high temperatures, the NO would be removed by subsequent chemical reactions. However, in the second step, the piston is receding, enabling the combustion products to expand and thereby significantly decrease in temperature. Consequently, the NO reactions slow down, unfortunately allowing the NO levels in the engine cylinder to "freeze" at their high, non-equilibrium levels established before the rapid expansion of the gases. In the third step, the exhaust valve opens, releasing the polluted chamber gases into the atmosphere. NO_2 is formed from reactions between the oxygen in the surrounding air and the NO from the exhausted cylinder gases. The concentrations of NO are much more significant than those of NO_2.

It should be noted that there are other NOx production mechanisms in addition to the process described above, such as the oxidation of nitrogen contained within certain fuels.

For the spark-ignition engine, oxidation of atmospheric nitrogen is the most important mechanism – its consideration is sufficient for this research.

1.3 The Challenge of NOx Control

Federal regulatory mandates are the motivation for auto manufacturers to develop methods of NOx control. An uncontrolled vehicle (i.e. one that does not employ any pollution control devices) emits approximately 4 g/NOx per mile. In 1973, the first legally imposed NOx formation limit was set at nearly 3 g/NOx per mile [8]. Legislation has become increasingly more stringent, with 0.4 g/NOx per mile being the current standard in California. This is to be restricted nationally to a level of 0.2 g/ NOx per mile in 1998, slated to be reduced even further in subsequent years. Industrial response to these aggressive pollution reduction tactics are best summarized in the words of John Riccardo, past President of Chrysler Corporation in his 1973 response to the Clean Air Act of 1970 [24]:

> First, the Clean Air Act of 1970 set emissions standards for automobiles which...are more stringent than necessary for protection of public health. Second, the Act, in effect, demanded the invention of totally new hardware to meet the ... standards which were then, and still are, beyond the capabilities of known technology. And third, the Act established a wholly unrealistic timetable for the introduction of this non-existent new technology.

The issues of time, expense, and technological capability have been and are still the major points of contention between industry and government, and continue to remain the greatest hurdle for industry to overcome.

There are additional factors which make manufacturer compliance with Federal legislation so difficult. The auto industry is engaged in a multi-front regulatory battle: fuel economy restrictions, safety requirements, and on the pollutant side, standards for not only NOx but also hydrocarbons (HC) and carbon monoxide (CO). Oftentimes, designing and operating an engine to adhere to one of these seemingly independent regulations results in an inability to fulfill another one. Figure 1.2 clearly demonstrates the tradeoff between fuel consumption and pollution formation. Conditions for maximum fuel economy directly conflict with those for NOx emissions. Likewise, as illustrated in Figure 1.3, the range of minimum HC production concurrently results in nearly maximum NO formation.

The primary, traditional method of NOx control has been through the use of a catalytic converter, which directs the exhaust gas through a casing which houses the catalytic material [16]. A significant disadvantage of catalytic converters is that their functionality is limited to specific temperature ranges and engine conditions. Even within their optimal operational window, catalytic converters are only approximately 90% effective (within a ~100,000 mile limit) ; though this level far surpasses those of other hardware pollution control technologies for spark-ignition engines, it is not sufficient to meet the government regulations which will soon be imposed. These issues, coupled with the severity of the government pollutant regulations, has forced auto manufacturers to seek a new approach to NOx reduction -- prevention of NOx at its source, within the engine cylinder.

Advanced control of engine operation is another method of NO production reduction. Auto manufacturers are very interested in the effects of the air/fuel (A/F) ratio and the quantity of exhaust gas recirculation (EGR) of the intake mixture. As illustrated in Figure 1.4, as the A/F ratio increases, less NO will be formed. The more the fuel is diluted by air (termed lean operation), the lower the peak burned product temperatures will be during combustion. This translates into lower NO levels. The two major disadvantages to lean operation are poor combustion stability and decreased fuel economy. Though low NO formation is seen with extremely rich operation (i.e. a very low A/F ratio), this adversely affects other requirements of engine performance. In the case of EGR, it is not fresh air, but burned exhaust gases which are added to the F/A mixture. EGR also dilutes the mixture, likewise reducing NO formation (Figure 1.4). The diluting effect of EGR, however, hurts combustion quality and adversely affects effects power(Figure 1.5). Despite their disadvantages, the reduced NO formation associated with dilution from both lean engine operation and high EGR levels continue to interest auto manufactures. Evaluation of the tradeoffs of one NOx formation prevention method as compared to another is extremely complex. A seemingly minor adjustment to intake mixture composition may have deleterious effects on other exhaust products and engine performance variables. Manufacturers are fast running out of the time and the money required to engage in the extensive experimental testing required to properly examine the complete range of these tradeoffs and to find an optimal solution.

1.4 The Role of Computational Models in the Control of NOx

As discussed in the previous section, auto manufacturers are forced to cope with the pollutant control problem under the constraints of time, expense, and technological capability. The extensive time required for experimentation, design validation, and subsequent engine development is in direct conflict with the immediacy of the Federal mandates. Cost is also a major issue, particularly with respect to experimental programs. Additionally, each manufacturer must comply with these standards as expediently and inexpensively as possible, in order to remain competitive and retain consumer market share. The question of technological capability refers to a manufacturer's ability to develop an optimized solution that meets federal regulations, when faced with an infinite combination of engine operation conditions and design geometries.

Auto manufacturers are unified in their belief that there is no alternative but to restructure their engine design processes, giving computational tools the primary role. Computational tools such as finite element analysis (FEA), computational fluid dynamics (CFD), and engine cycle simulations (which are the tools of interest for this thesis) have previously been employed in the design process, but only in an auxiliary fashion. Experimentation and "engineer experience" still provide the foundation of engine design programs. Pressured by legislation, cutbacks and increased competition, auto manufacturers now maintain that the expense and time associated with the traditional design process are no longer acceptable. As the billions of dollars that are being poured into model development and validation indicate, the auto industry fully intends to use computational tools as the main mechanisms of their design processes. Computational tools are hoped to provide, through their speed, reliability and flexibility: minimization of

experimentation, reduction of the length and expense of each design step, and elimination of "feedback loop" redesigns, as illustrated in Figure 1.6. Hence, computational modeling tools are expected to optimize not only the design process, but the product itself. Ford Motor Company is one such corporation which is aggressively pursing the implementation of engine cycle simulations in their design processes.

Companies like Ford feel that at least three major advantages from investment in computational models [3]:

1) *Identification of the key controlling variables*

This allows engineers to establish meaningful experimental program plans, without the cost and time involved with "preliminary assessment" experimentation.

2) *Ability to predict behavior over a wide range of design and engine operation parameters*

This enables designers to screen concepts prior to major hardware undertakings. Importantly, trends and tradeoffs are easily established, thus proving the viability of a design in meeting program objectives and eliminating "feedback loop" redesigns. Since behavior is reliably known over complete ranges, engine designs may be optimized accordingly.

3) *More complete understanding of the physical system*

Creation of a reliable model requires that the components and processes being represented are properly understood. The more details known about the entities and their interactions, the better the model can represent the physical reality. Hence, such "physically based" modeling motivates advanced, detailed thought, oftentimes neglected.

This in turn could yield new ideas – either as improvements to current technologies or as the generation of innovative ones.

1.5 Specific Objectives of this Research

The foremost objective of this thesis is to develop NOx formation models into reliable, cost-effective design tools. Therefore, the models must attain greater accuracy than is currently possible, with the stringency of the Federal regulations setting the required accuracy level. These models also have to be reliable over the complete range of engine operating conditions, in order that they may play the central roles which the auto industry intends. As there is significant interest in the lean and dilute limits of operation (Section 1.3), this investigation accordingly emphasizes those regions. The models themselves must be able to be easily integrated into the design process, in order that they may be fully utilized as design tools. Consequently, these models are required to provide enough flexibility such that they may be used with a variety of different "inputs," including engine geometries and operating conditions.

Ford Motor Company, who assisted with this study, is actively seeking to improve their own cycle simulation. Accordingly, an objective of this thesis is to provide industry modeling teams with evidenced, detailed advice concerning the next steps of their model development.

Based upon these requirements, three benchmarks were established to monitor the development of the NOx formation models: identification of the relevant physics and

chemistry; determination of the areas where current models are deficient; and, upon this foundation, development of the improved models.

1.6 Modeling Approach

The purpose of this section is to provide an overview of how the modeling problem was approached; these issues are thoroughly addressed in the subsequent chapters of this thesis. The computational tool used throughout this work is the MIT Quasi-Dimensional Cycle Simulation (Section 2.1). A "physically based" modeling approach is taken to ensure the flexibility of the final model. In order to establish some boundaries to the scope of the investigation, it is assumed that NO formation rates depend mainly on pressure, burned product gas temperature, and mixture composition – these factors define the "thermal state" of the gas involved with NO formation. Additionally, kinetic considerations encompass only "post-flame" NO formation mechanisms. Hence, there are two critical components of the modeling approach: the kinetics of NO formation and the thermal state of the burned gas (Figure 1.7). Both the kinetic mechanisms themselves and their associated rates of reaction comprise the kinetic modeling methodology. Physically-based representation of the thermal state of the burned gas is achieved through the development and implementation of the thermal boundary layer, sequential or layered burn, and crevice models (Chapter 4). Each of these three models affects the representation of the combustion process in the engine cylinder.

Discussions with the modeling team of Ford Motor Company also proved extremely beneficial. Ford's cycle simulation, GESIM, is fundamentally the same as the MIT cycle

simulation, but has been significantly enhanced. Most notable are their extensive engine geometry routines which enable them to perform detailed design analysis.

1.7 Project Strategy

The project strategy may be presented as follows:

1) Physics analysis and improved model development
2) Obtained the data from Ford Motor Company (A/F ratio and EGR ranges) to be used as the basis for model validation
3) Model validation and consistency check
4) Compare data and predictions with step-by-step improvements in models
5) Complete assessment and identify the modeling additions needed to accurately predict NOx emissions with engine cycle simulations

1.8 Outline of Thesis

Chapter Two presents an overview of the cycle simulation and investigates the kinetic issues mentioned above. The "base" version of the cycle simulation was thus defined for the analysis of this thesis. Chapter Three deals with the thermal-state approach to the problem, treating both the boundary layer and layered representation of the combustion process. Chapter Four discusses the crevice model and the means by which it was implemented in detail. Chapter Five analyzes the results of this thesis, along with some

preliminary design recommendations. The conclusions of this work are presented in Chapter Six.

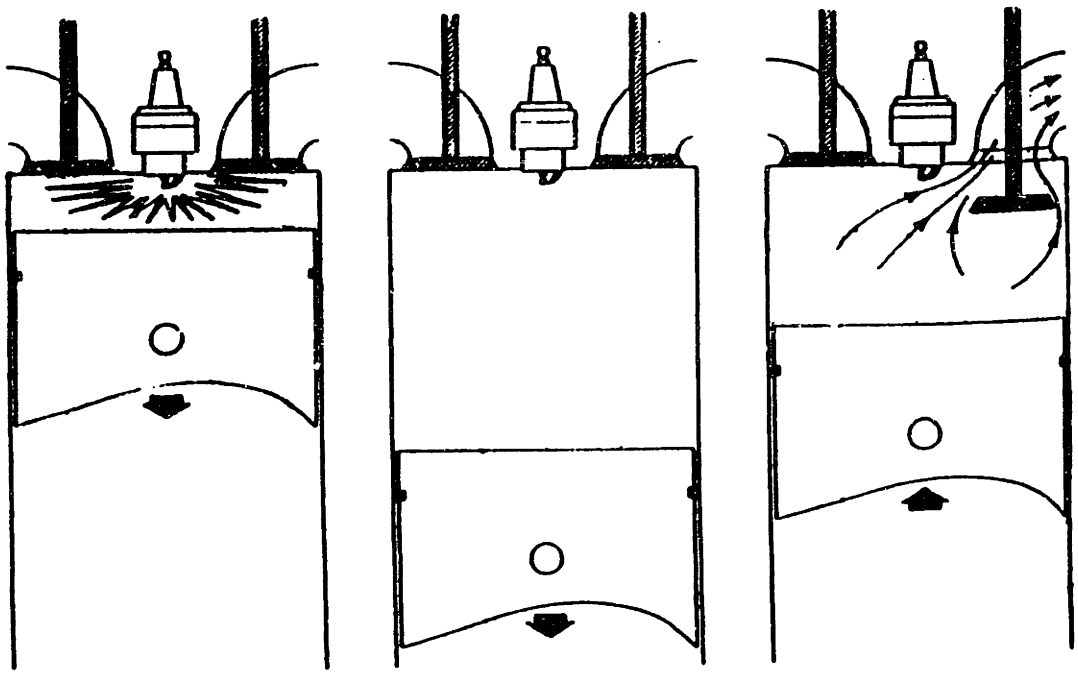

Figure 1.1: NO formation in the spark-ignition engine cylinder

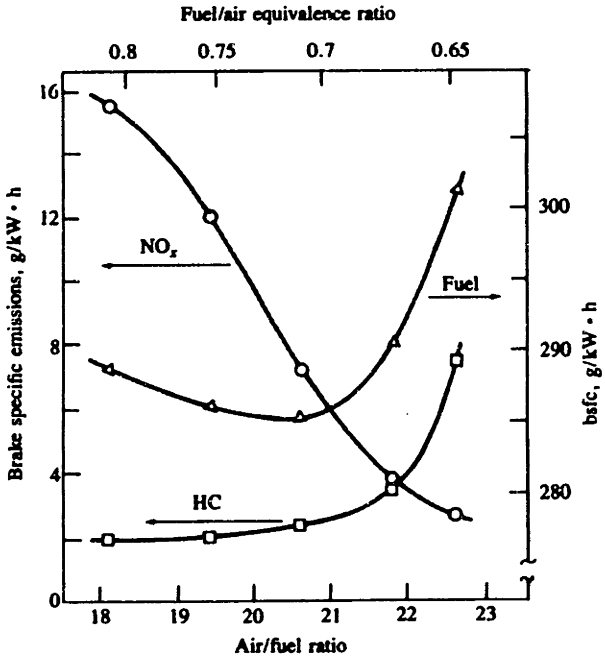

Figure 1.2: Trade-off between fuel consumption and NOx formation [16]

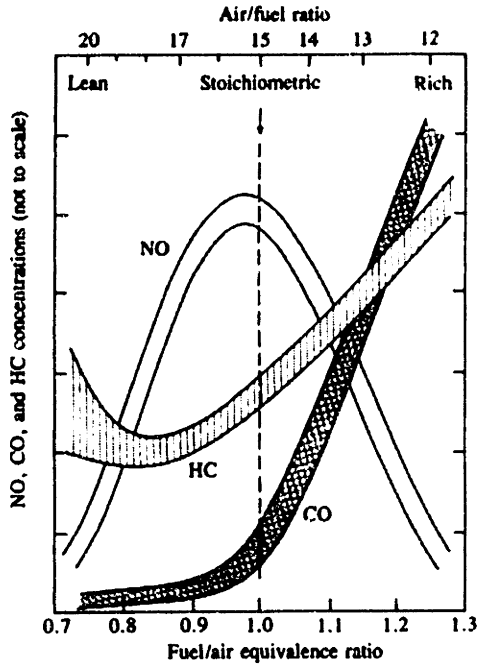

Figure 1.3: Pollutant concentration variations with fuel/air equivalence ratio in a conventional spark-ignition engine exhaust [16]

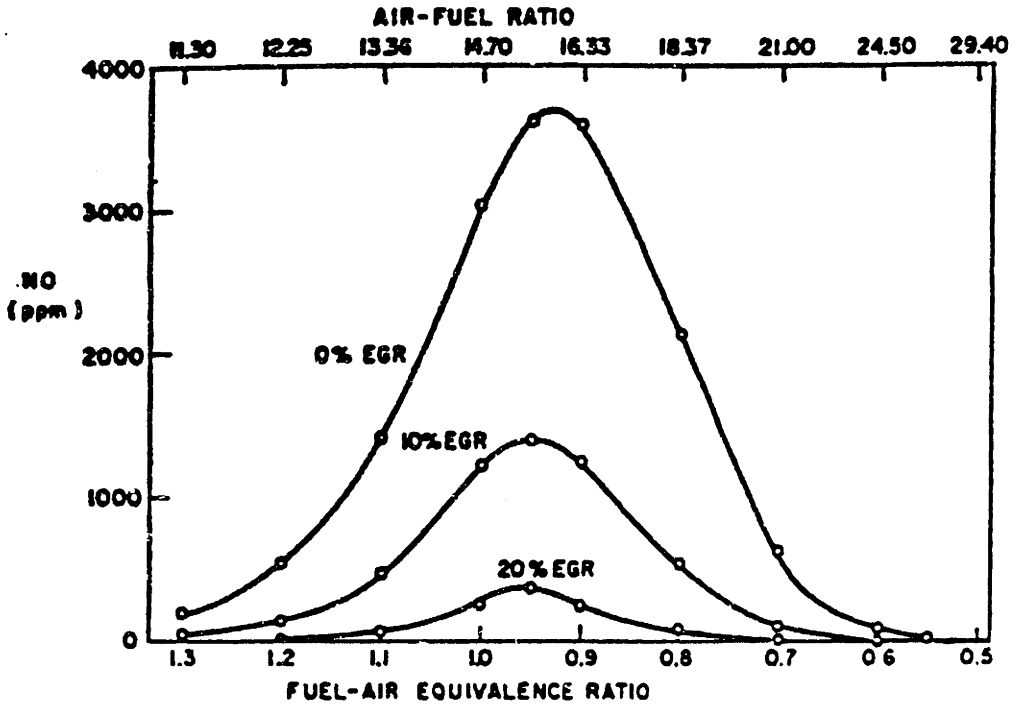

Figure 1.4: Variation of exhaust NO concentrations with EGR and equivalence ratio (Computations)

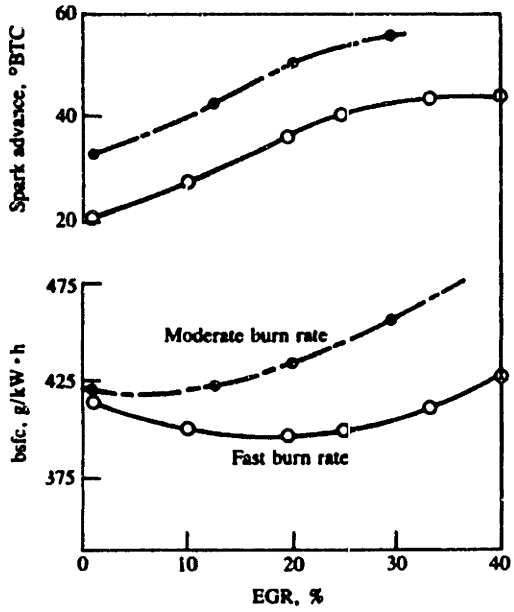

Figure 1.5: Trade-off between fuel consumption and NO formation—EGR sweep [16]

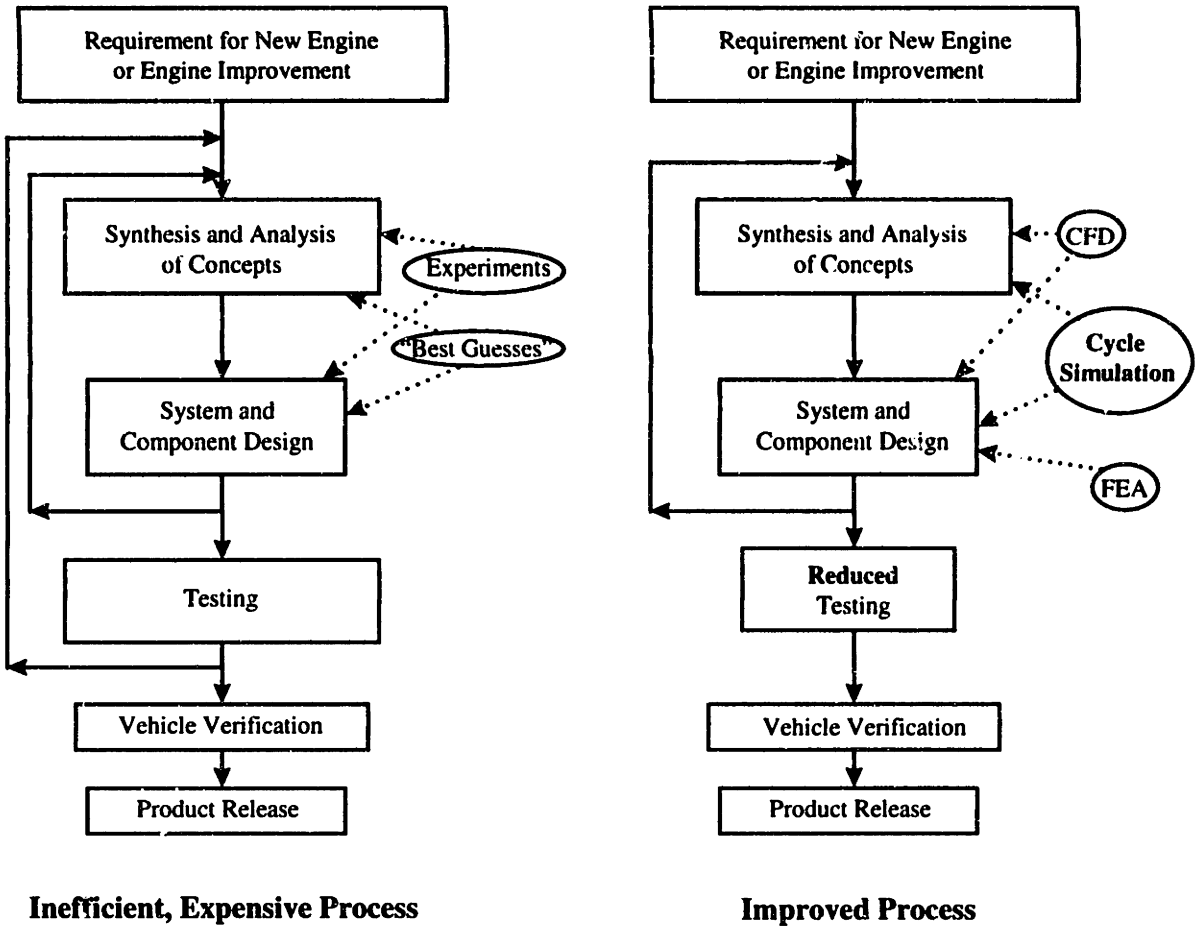

Figure 1.6: Engine Design Process

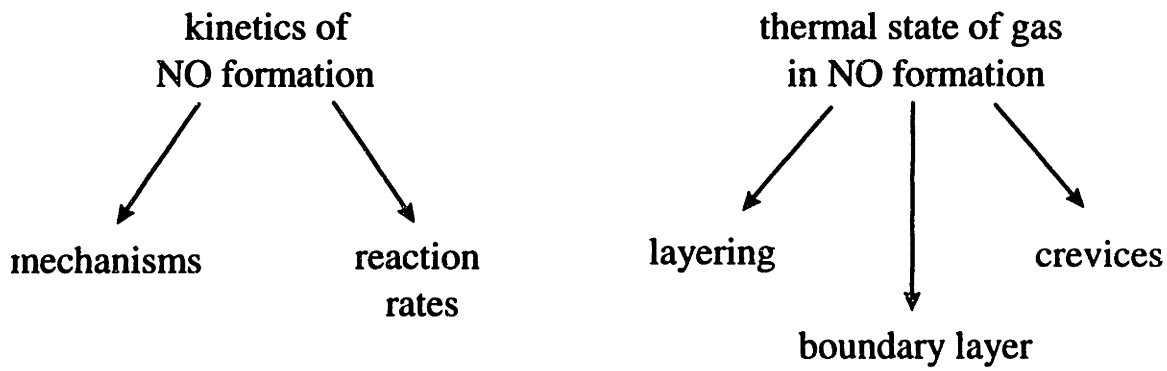

Figure 1.7: Overview of Modeling Approach

2. Computational Modeling of NO Kinetics

2.1 The MIT Cycle Simulation

The computational work of this investigation was performed using the MIT Spark Ignition Engine Cycle Simulation. This model has been used and documented extensively in the past [12, 29]. A brief discussion of its framework and operation will be provided here so that modeling improvements and additions may be put in perspective.

The cycle simulation is divided into four parts; each represents one of the major spark-ignition engine cycle processes (intake, compression, combustion with expansion, and exhaust). The contents of a single engine cylinder, which comprise the thermodynamic system of the simulation, are treated throughout the entire 720 degree four-stroke cycle. The model is able to predict crank-angle resolved information for several variables including cylinder pressure and both unburned and burned gas temperatures, in addition to performance parameters such as torque, fuel consumption, heat transfer, and nitric oxide emissions.

The key to the operation of the cycle simulation lies in the construction and the subsequent solution of a group of differential equations which are based on energy and mass conservation. These equations are used to model critical features of engine operation. The specific set of differential equations which needs to be solved varies with

the portion of the cycle which is being treated. At each step in the simulation, the active equations are simultaneously solved by a numerical integrator (detailed in [29]).

Simulation operation proceeds as follows. To start, the required inputs must be specified. These may be grouped into three areas: geometric features of the engine, such as bore size and cylinder volume; engine operating conditions, such as speed and load; and data for the numerical routines, such as tolerance values. The simulation is then initiated at intake valve opening once the initial in-cylinder gas conditions are defined. The expressions modeling intake stroke phenomena, such as mass flow though the intake valve, are evaluated. Eventually the information necessary to arrive at the equations for mass and energy transfer is complete and the differential equations may be solved. This procedure, performed at every time-step, is repeated for compression, combustion/expansion, and exhaust. Again, the phenomena and active equations for each stroke vary according to modeling requirements. At the end of the cycle, the final in-cylinder conditions are compared with the assumed starting values to ensure that they agree within specified tolerances. If they do not, another iteration of the cycle will occur. Once appropriate solutions are found, the engine's performance is calculated and the simulation is complete.

2.2 Governing Equations of the Cycle

This section presents the governing differential equations required to solve for the thermodynamic state of the cylinder contents at any time during the operating cycle. For a complete derivation, the reader is referenced to Ref. [29]. The analysis of this section

does not include the effects of crevices, which are small regions connected to the combustion chamber that cause fuel to escape normal combustion and oxidation processes. The restructuring of the differential equations required to account for the crevice phenomenon is fully derived in Chapter Four.

The combustion chamber system, illustrated in Figure 2.1, is open to the transfer of mass, energy (through work and heat), and enthalpy as dictated by cycle requirements at the instant of analysis. The system is of variable volume, but is always of uniform pressure. The cylinder contents are treated as ideal gases, enabling the application of the familiar law,

$$p = \rho RT. \tag{2.1}$$

During the intake stroke, fresh fuel-air mixture (defined as component 1) is added to the burned residual gas (component 2). With differentiation of the ideal gas law with respect to time and with appropriate substitutions and algebra, the rate of change of pressure for the two-component cylinder system may be expressed as:

$$\dot{p} = \frac{\rho}{\partial\rho/\partial p}\left[\left(\frac{R_1 - R_2}{R}\right)\dot{x}_1 + \frac{\dot{m}}{m} - \frac{\dot{V}}{V} - \frac{\partial\rho}{\partial T}\frac{\dot{T}}{\rho}\right] \tag{2.2}$$

The next task is to obtain an expression for the rate of change of temperature from the standard open-system energy equation,

$$\dot{E} = \sum \dot{m}_j h_j - \dot{Q}_W - \dot{W} \tag{2.3}$$

wherein:

$\dot{Q}_W$ = rate of heat transfer to the walls, loss is defined as positive

$\dot{W} = p\dot{V} =$ rate of work done by the system, defined as positive

$\sum \dot{m}_j h_j =$ net rate of enthalpy flux; j represents a flow stream in or out of the system

$\dot{E} = \frac{d}{dt}(mh - pV) =$ rate of change of internal energy.

It is most appropriate to express the rate of change of temperature equation independently of the rate of change of cylinder pressure (Eqn. 2.2), since both quantities are unknown and computational requirements must be maintained at a reasonable level. By making the appropriate substitutions and operations, the rate of change of temperature is found to be:

$$\dot{T} = \frac{B}{A}[\dot{x}_1(\frac{R_1 - R_2}{R} + \frac{h_2 - h_1}{B}) + \frac{\dot{m}}{m}(1 - \frac{h}{B}) - \frac{\dot{V}}{V} + \frac{1}{mB}(\sum \dot{m}_j h_j - \dot{Q}_w)] \quad (2.4)$$

wherein the aggregate variables A and B are:

$$A = C_p + \frac{(\frac{\partial \rho}{\partial T})_p}{(\frac{\partial \rho}{\partial p})_T}[\frac{1}{\rho} - C_T] \quad (2.5)$$

$$B = \frac{(1 - \rho C_T)}{(\frac{\partial \rho}{\partial p})_T} \quad (2.6)$$

The above equations are for a system that does not account for the crevice effect. The presence of crevices causes the amount of mass in the cylinder, and likewise the mass fraction of fresh charge in the cylinder, to depend on pressure. This issue is addressed in Chapter 4.

Clearly, engine processes such as heat transfer to the combustion chamber walls, gas exchange, and flame propagation must all be modeled before solution of the governing equations is possible. In addition, the thermodynamic properties of the cylinder system must be evaluated throughout the cycle. Towards this end, the reader is again referenced to [29] for a full explanation of these modeling procedures. For the NO formation topic at hand, the combustion and pollutant formation submodels are most pertinent and will be discussed in subsequent sections of this thesis.

2.3 Modeling The Combustion Process

Complete discussion of the NOx production model requires a presentation of the combustion model itself. Conditions in the engine cylinder during combustion are illustrated in Figure 2.2. At its simplest representation, the cylinder contents are distributed into two zones – one which contains the unburned charge mixture and one which contains the burned charge. The volume where reaction is actually occurring, the flame, is negligible in size (~0.2 mm thick) in comparison with the entire cylinder volume and may be neglected [16]. The contents in the unburned zone are treated in the same manner as the cylinder mixture during intake and compression – as a homogeneous mixture of fuel, air, residual gas, and EGR – and are uniform in temperature and pressure. The same property calculation subroutines are employed. The burned zone is also treated as a homogeneous mixture of gases, with the products of combustion in chemical equilibrium. Thermodynamic property calculation routines specific to the burned zone are applied.

As the flame front propagates through the unburned mixture in the engine cylinder, additional burned charge is created. This increase in burned charge over time is modeled by the Wiebe function, which relates the mass fraction burned in the cylinder to crank angle. This method has been employed several times previously (Poulos, Heywood text, Raine, Heywood and Watts]. This burned mass fraction (x_b) relationship is represented as follows:

$$x_b = 1 - \exp[-a(\frac{\theta - \theta_o}{\Delta\theta_c})^{m+1}] \qquad (2.7)$$

where "m" and "a" are constants, θ represents crank angle, $\Delta\theta_c$ is the total combustion duration, and θ_o is the start of combustion (Figure 2.3). The equation which is integrated in the cycle simulation is merely the derivative of the Wiebe function with respect to θ,

$$\frac{dx_b}{d\theta} = a(m+1)(\frac{\theta - \theta_o}{\Delta\theta_c})(1 - \exp[-a(\frac{\theta - \theta_o}{\Delta\theta_c})^{m+1}]) \qquad (2.8)$$

Changing the constants "a" and "m" significantly alters the shape of the curve (Figure 2.4 and Figure 2.5), thereby allowing accurate portrayal of different burn profile types.

2.4 Modeling NO Production

It is important to define precisely what constitutes "NO_x" emissions. "NO_x" refers to both NO (nitric oxide) and NO_2 (nitrogen dioxide). However, it is NO which is predominantly formed in the engine cylinder. Accordingly, this research explicitly considers the formation of NO, but "NO_x" and "NO" are sometimes used interchangeably.

Previously, the process of nitric oxide formation under the conditions typical in a spark ignition engine had been assumed to be governed by the following set of reactions, known as the extended Zeldovich Mechanism:

$$\begin{aligned} N_2 + O &\xleftrightarrow{1} N + NO \\ N + O_2 &\xleftrightarrow{2} NO + O \\ N + OH &\xleftrightarrow{3} NO + H \end{aligned} \qquad (2.9)$$

The associated forward and backwards rate constants (k_i^+ and k_i^-, where "i" refers to the reaction number), in units of cm^3/mol-s, were taken to be as follows:

reaction	k_i^+	k_i^-
1	$7.6 \times 10^{13} \exp[-38{,}000/T]$	1.6×10^{13}
2	$6.4 \times 10^{9} T \exp[-3150/T]$	$1.5 \times 10^{9} T \exp[-19{,}500/T]$
3	4.1×10^{13}	$2.0 \times 10^{14} \exp[-23{,}650/T]$

These reaction rates are experimentally determined. As experimental techniques improve, updated values of these reaction rates are published. Rather than attempting to assess the validity of different sets of rates, the most recent set of rates recommended by Miller and Bowman [25, 34] in an extensive review was used. These reaction rate constants are:

reaction	k_i^+	k_i^-
1	$7.6 \times 10^{13} \exp[-38{,}000/T]$	$3.3 \times 10^{12}\ T^{0.3}$
2	$6.4 \times 10^{9}\ T \exp[-3160/T]$	$1.5 \times 10^{9}\ T \exp[-19{,}500/T]$
3	3.8×10^{13}	$2.0 \times 10^{14} \exp[-23{,}650/T]$

However, as indicated, there is some disparity in the literature concerning the values of these reaction rate constants. Consequently, rather than trying to attempt to determine which is the "correct" set of reaction rate constants, an analysis which examined the sensitivity of the NO_x predictions to these rate constants was performed. The above rate constants were both multiplied and divided by a factor of two, first all together and then each individually. The results were analyzed over a range of equivalence ratios and EGR values. In this way, the sensitivity of the NO_x results to the likely uncertainty in reaction rate constant values was assessed. Performing the same calculations for each reaction in turn allowing for the examination of the sensitivity of the individual reactions. Results are shown in Figures 2.6-2.9 and 2.10-2.14. Clearly, the first reaction is seen to be the critical rate-limiting step, as expected [11]. It should be noted that these calculations were performed using the "Base Case" set of reactions (Section 2.5).

For both the equivalence ratio sweep and the EGR sweep, an exact relationship does not exist between the amount the rate constants of Zeldovich reactions 1, 2, and 3 were changed and the resulting change in NO formation. Doubling the reaction rates over the equivalence ratio sweep caused NO formation to be ~1.8 to 1.3 times larger than its original predictions; halving the rates had an ~0.7x effect. The lean operation regimes

demonstrates the greatest sensitivity to the change in reaction rates. Over the EGR sweep, doubling the reaction rates caused a corresponding change in NO predictions ranging from ~1.1x to ~2x. Halving the rates affected the computation correspondingly, by ~0.5x lower NO formation. Largest sensitivity is seen with an EGR dilution of 20%.

These calculations highlight the importance of obtaining reasonably accurate reaction rate values. NO formation sensitivity to the reaction rates of equations 1, 2, and 3 of the extended Zeldovich mechanism should not be ignored.

The extended thermal Zeldovich mechanism presented above was originally proposed to govern the formation of NO from the oxidation of atmospheric (molecular) nitrogen, believed to be the primary source of NO formation. For the purposes of this research, in which indolene fuel (gasoline) was employed in calculations, it was not necessary to consider the oxidation of nitrogen-containing compounds in the fuel. Several investigators [6], however, have suggested that the inclusion of the "N_2O Mechanism" is necessary to complete the NO formation mechanism, particularly for fuel-lean and dilute conditions. The N_2O mechanism of NO formation is as follows:

$$\begin{aligned} H + N_2O &\xleftrightarrow{4} N_2 + OH \\ O + N_2O &\xleftrightarrow{5} N_2 + O_2 \\ O + N_2O &\xleftrightarrow{6} NO + NO \\ N_2O + N_2 &\xleftrightarrow{7} N_2 + O + N_2 \end{aligned} \qquad (2.10)$$

with associated rate constants from Baruah, et al., again in units of cm^3/mole-cm, being:

$$k_4^+ = 3.0 \times 10^{13} \exp [-5350/T]$$

$$k_5^+ = 3.2 \times 10^{15} \exp [-18{,}900/T]$$

$$k_6^+ = k_5^+$$

$$k_7^+ = 1.0 \times 10^{15} \exp [-30{,}500/T]$$

With these mechanisms and their corresponding reaction rate constants, an expression for the time rate of change of NO formation may be developed. It is meaningful to present this derivation for two reasons: first, the inclusion of this N_2O mechanism is a new addition; second, the derivation highlights two noteworthy assumptions -- the "equilibrium assumption" and the "steady-state" assumption of species formation.

First, consider the simple reaction

$$A + B \xrightarrow{k} C \qquad (2.11)$$

for which the rate of change of concentration of specie A may be determined from:

$$\rho \frac{d}{dt}\left(\frac{[A]}{\rho}\right) = -k[A][B] \qquad (2.12)$$

where ρ represents the density of the constant-mass system. Such an equation is required to determine the rates of change of species in the burned gas zone. A relationship of this form is required in order to separate concentration changes due only to chemical kinetics and not volume change. Derivation of a simple expression is possible by assuming the concentrations of O_2, O, H, OH, and N_2 to be their equilibrium values:

$$[O_2] = [O_2]_e$$

$$[O] = [O]_e$$

$$[H] = [H]_e \qquad (2.13)$$

$$[OH] = [OH]_e$$

$$[N_2] = [N_2]_e$$

and by defining the equilibrium, one-way rates of reaction as:

$$R_1 = k_{+1}[N_2]_e[O]_e = k_{-1}[N]_e[NO]_e$$

$$R_2 = k_{+2}[N]_e[O_2]_e = k_{-2}[NO]_e[O]_e$$

$$R_3 = k_{+3}[N]_e[OH]_e = k_{-3}[NO]_e[H]_e$$

$$R_4 = k_{+4}[H]_e[N_2O]_e = k_{-4}[N_2]_e[OH]_e \qquad (2.14)$$

$$R_5 = k_{+5}[O]_e[N_2O]_e = k_{-5}[N_2]_e[O_2]_e$$

$$R_6 = k_{+6}[O]_e[N_2O]_e = k_{-6}[NO]_e[NO]_e$$

$$R_7 = k_{+7}[N_2O]_e[N_2]_e = k_{-7}[N_2]_e[O]_e[N_2]_e$$

This assumption is reasonable since the overall rate of NO formation by the Zeldovich mechanism (the thermal mechanism) is much slower than the rates of the fuel oxidation reactions. Therefore, formation of NO by the Zeldovich reaction mechanism may be decoupled from the fuel oxidation mechanism and equilibrium concentrations assumed for the C-O-H system species. Next, the rate equations for NO, N, and N_2O may be written as:

$$\frac{1}{V}\frac{d[NO]V}{dt} = -\alpha(\beta R_1 + R_2 + R_3 + 2\alpha R_6) + R_1 + \beta(R_2 + R_3) + 2\gamma R_6$$
$$\frac{1}{V}\frac{d[N]V}{dt} = -\beta(\alpha R_1 + R_2 + R_3) + R_1 + \alpha(R_2 + R_3) \qquad (2.15)$$
$$\frac{1}{V}\frac{d[N_2O]V}{dt} = -\gamma(R_4 + R_5 + R_6 + R_7) + R_4 + R_5 + \alpha^2 R_6 + R_7$$

wherein

$$\alpha = \frac{[NO]}{[NO]_e}$$
$$\beta = \frac{[N]}{[N]_e} \qquad (2.16)$$
$$\gamma = \frac{[N_2O]}{[N_2O]_e}$$

The definition of V varies with the type of combustion model used. With the fully mixed model (Section 2.2), in which the burned zone gases are treated as a homogeneous mixture characterized by an average temperature, V refers to the total volume of burned gas. When the unmixed model is employed (Section 3.2), wherein the newest layer of burned gas does not mix or exchange heat with previously burned gas layers each retaining an individual temperature and composition, V is the volume of one such layer of burned gas.

The relaxation times for the N and N_2O species are several orders of magnitude shorter than for NO [22]. Hence, it is reasonable to assume steady-state concentrations for N and N_2O; therefore the right hand side of their rate of change of concentration equations above (Eqn. 2.15) may be set equal to zero and expressions for β and γ may be found in terms of the R's. These values may be substituted into the equation for the rate of change of NO concentration, which may then be written as:

$$\frac{1}{V}\frac{d[NO]V}{dt} = 2(1-\alpha^2)\left[\frac{R_1}{1+\alpha\left[\frac{R_1}{R_2+R_3}\right]} + \frac{R_6}{1+\left[\frac{R_6}{R_4+R_5+R_7}\right]}\right] \quad (2.17)$$

The strong dependence of NO formation on temperature is clear. As temperatures rise, the NO formation rate does as well. This fact was a major motivation to assess the accuracy of the thermal state predictions of the burned charge and to improve these predictions (Chapters 3 and 4).

It is important to note that the above discussion assumes NO is produced only in the post-flame gases. Strictly speaking, NO is also produced in the flame front region. However, residence time in the flame front is extremely short since the flame volume is very small with respect to the burned zone volume, so an analysis which focuses only on NO formation in the post-flame gases is reasonable. An additional justification results from the fact that the burned gases will reach temperatures higher than they experienced during the combustion reaction itself because the cylinder pressure is still rising for most of the combustion process. Since NO formation increases with increasing temperature, the NO formation rates in the post-flame gases will dominate those in the reaction zone. For further information concerning the formation of NO in the flame zone, termed "prompt NO," the reader is referred to [16, 25].

The impact of the inclusion of the N_2O mechanism is shown in Figures 2.6 to 2.9. As indicated in Figure 2.6, inclusion of the N_2O mechanism increases NO formation predictions by ~20% at the fuel lean operating points of $\phi = 0.623$ and $\phi = 0.73$. Figure 2.7 illustrates the diminishing impact of the N_2O mechanism as equivalence ratio is increased. For the fuel-rich point investigated ($\phi = 1.15$), the N_2O mechanism

demonstrated no effect at all. This is as expected – the additional fresh air makes available more of the necessary constituents needed for the N_2O mechanism to become significant.

The N_2O mechanism had a negligible impact over the entire EGR sweep (Figures 2.8 and 2.9). While some effect may have been expected at the very dilute conditions, there are at least two possible explanations for its absence. First, the increase in NO formation expected with dilute mixture could very well be present, but the small scale of the quantity of NO formation calculated combined with expected sensitivity levels present such a small change from being detected. Second, while addition of EGR does indeed dilute the cylinder mixture, it does so using gas assumed to be composed completely of burned products. This is in sharp contrast to the case of dilution by adding more fresh air to the intake mixture (the lean condition). As the N_2O mechanism requires the radicals O and N_2 (among others) for completion, it follows that the mechanism would be more important for a mixture diluted with air than one with combustion product gas.

2.5 Definition of the "Base Case"

The above sections have summarized the fundamental physics and operation of the MIT cycle simulation. Effectively, the "base case" of the cycle simulation operation has been defined. Specifically, this entails: governing equations as outlined in Section 2.2, the burn profile represented by the Wiebe function, an NO formation mechanism consisting of both the Zeldovich reactions and the N_2O reactions, and use of the updated

reaction rates proposed by Miller and Bowman. All modifications to the MIT cycle simulation will be discussed relative to this base case.

2.6 Model Development Goals

As stated previously, the two critical factors governing NO formation are NOx chemical kinetics and the "thermal state" of the engine in-cylinder burned gases. The thermal state is defined by the composition and thermodynamic properties of the in-cylinder gases and is determined by the rate and completeness of the combustion process. Corresponding modeling issues are: combustion chamber crevices and similar mechanisms by which a fraction of the fuel does not burn, the thermal boundary layer that results from heat transfer to the walls, and the sequential or layers charge burning process that flame propagation produces.

The next two chapters discuss each of these phenomena in turn – first on a physical level, and then on a computational model one. The impact that these models have on the NO predictive capabilities of the cycle simulation is then assessed.

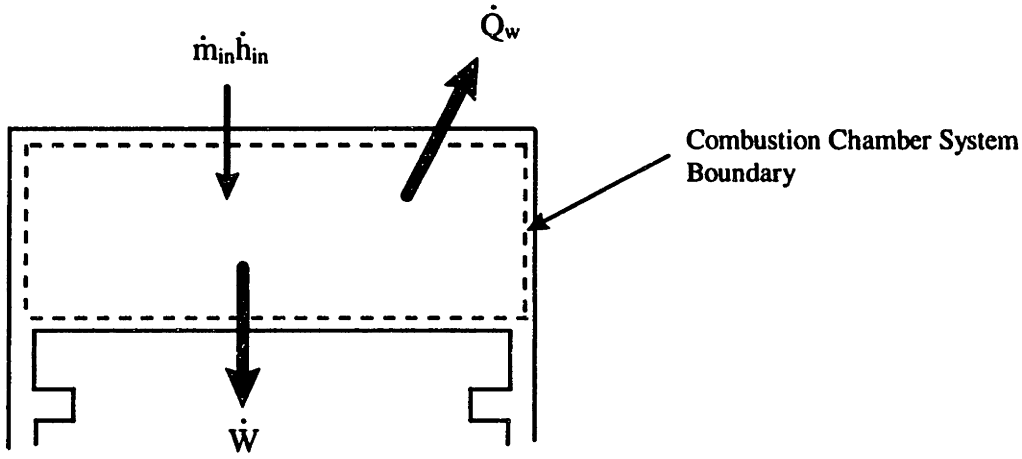

Figure 2.1: Definition of combustion chamber system

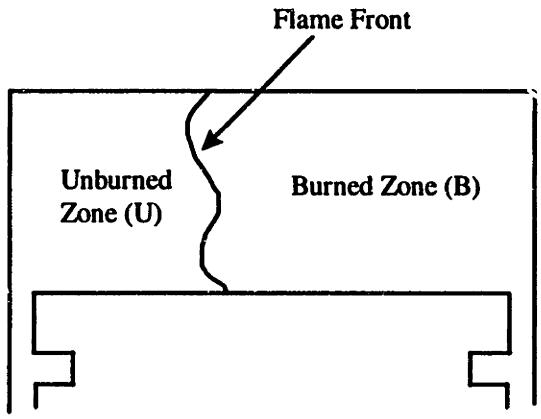

Figure 2.2: Two zone representation of cylinder contents during combustion

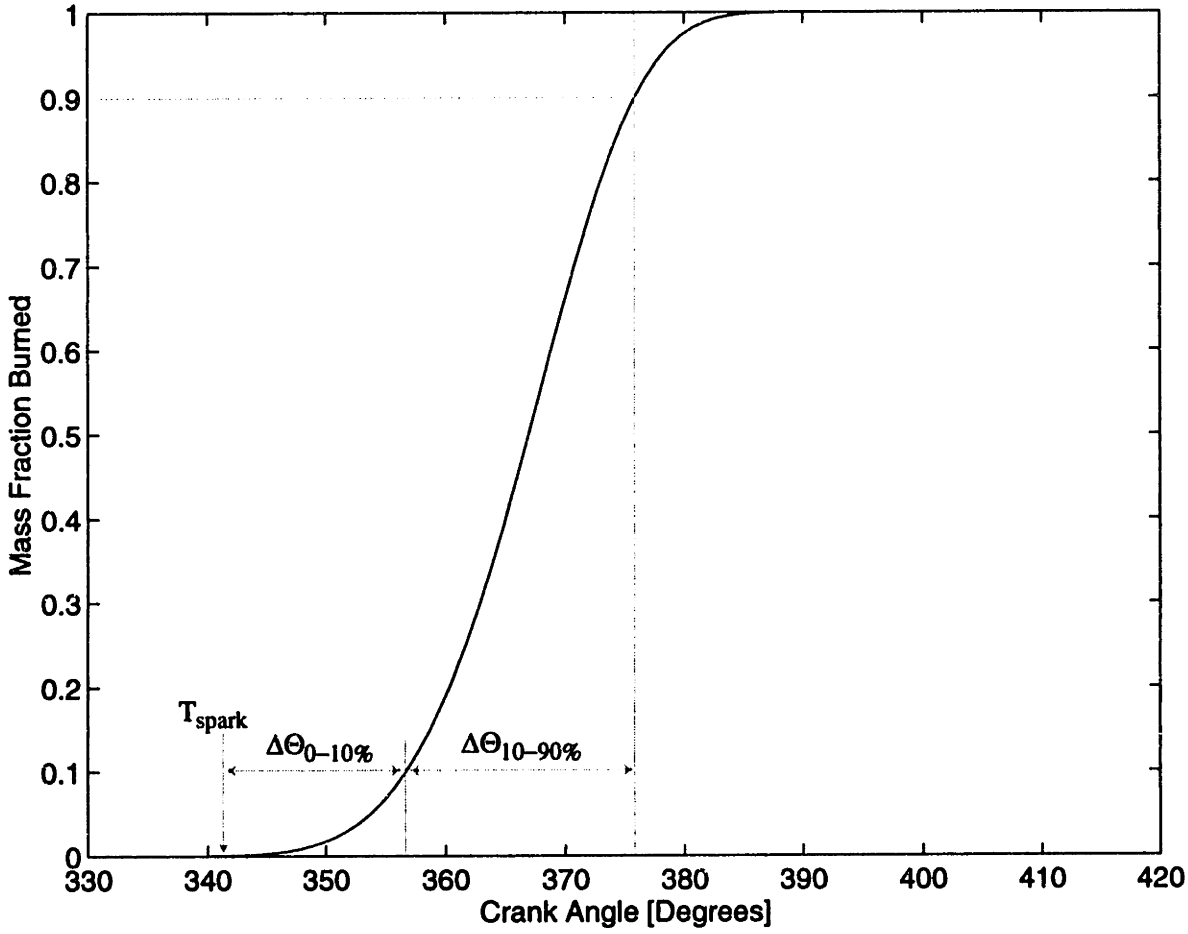

Figure 2.3: Wiebe function definition

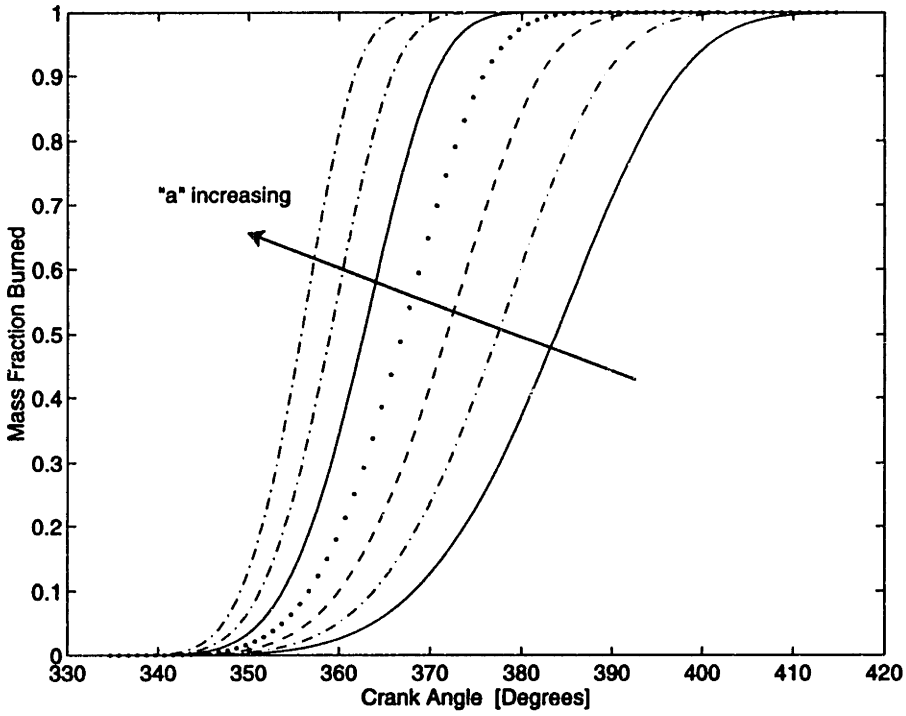

Figure 2.4: Effect of changing the "a" constant in the Wiebe function

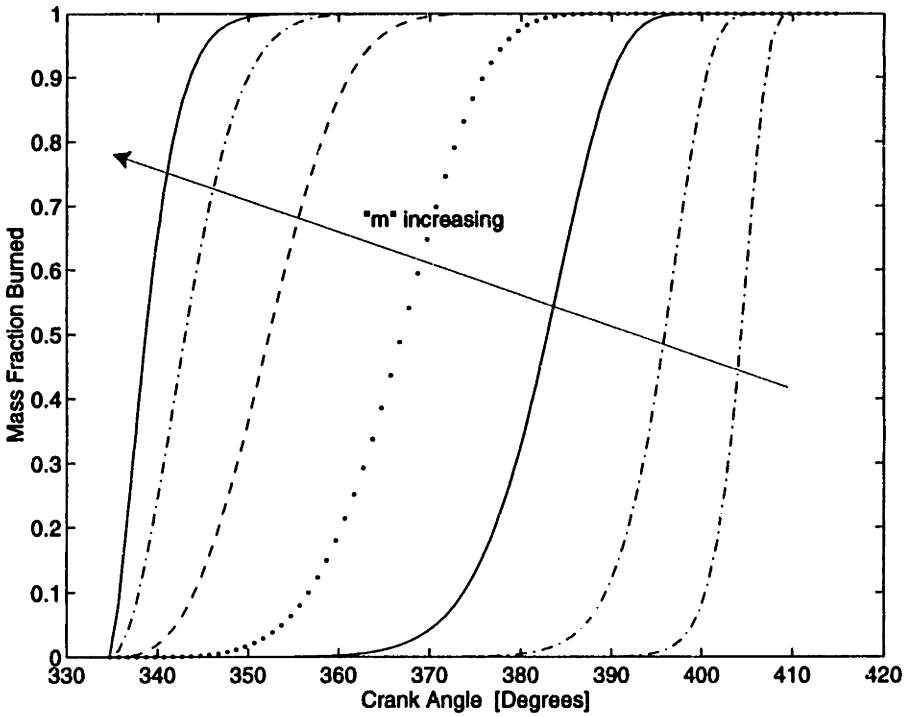

Figure 2.5: Effect of changing the "m" constant in the Wiebe function

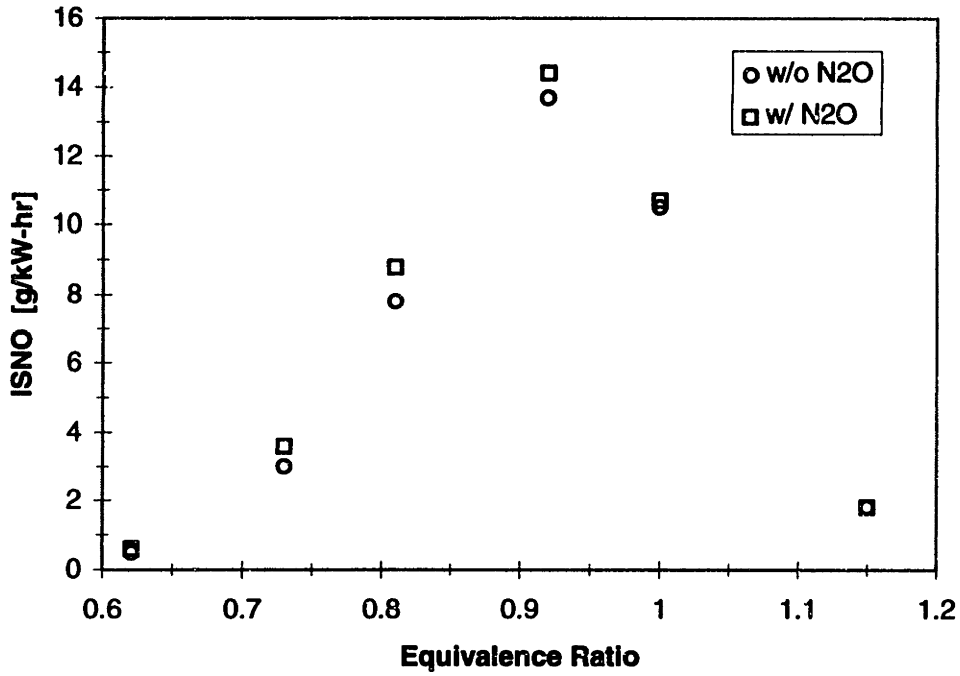

Figure 2.6: Computational NO formation results for cases with and without N_2O mechanism for equivalence ratio sweep

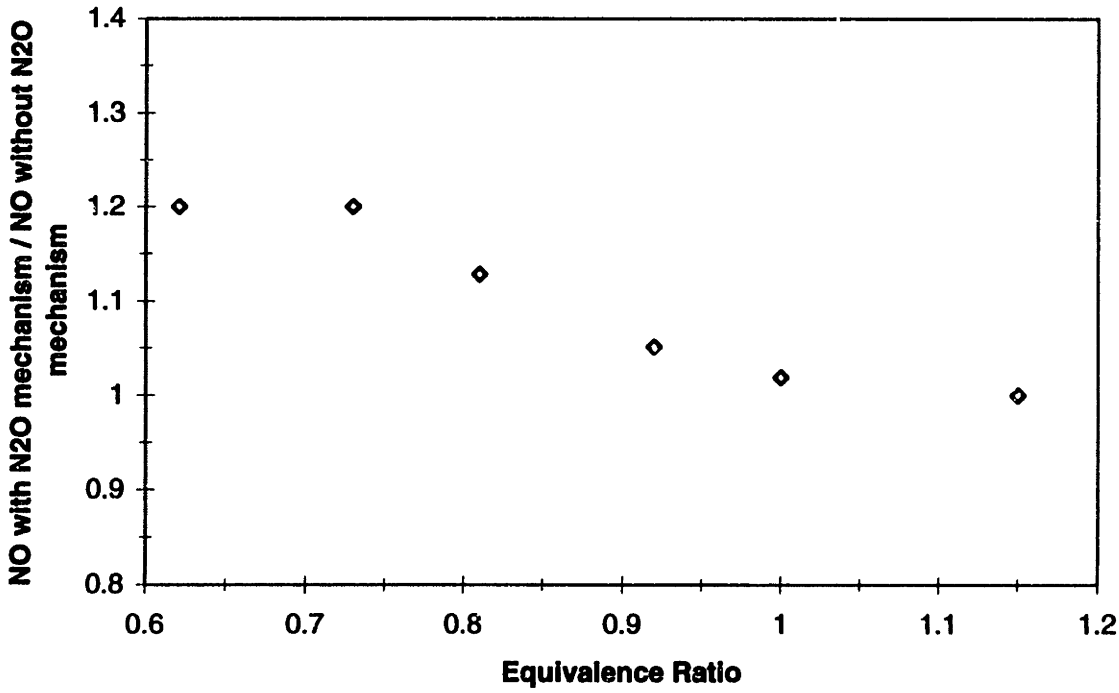

Figure 2.7: Impact of N_2O mechanism -- equivalence ratio sweep

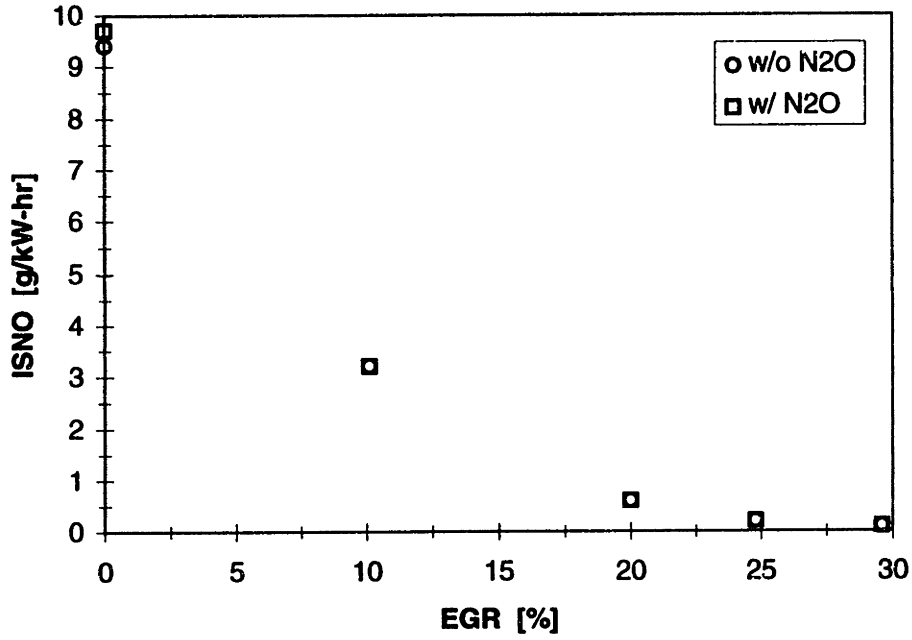

Figure 2.8: Computational NO formation results for cases with and without N_2O mechanism for equivalence ratio sweep -- EGR sweep

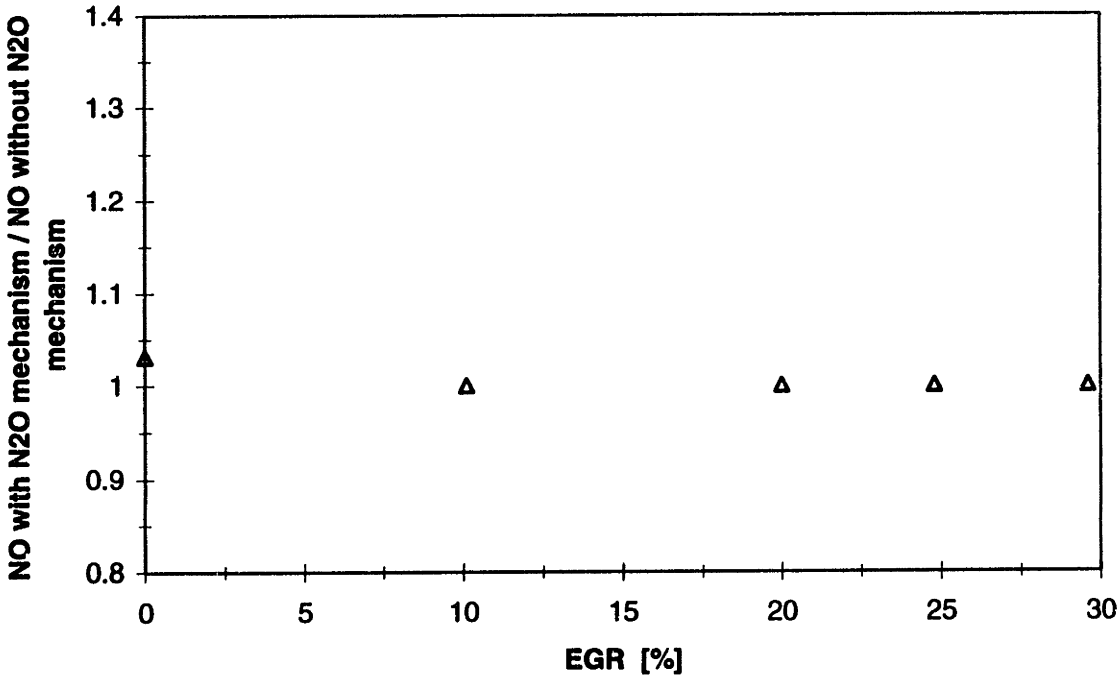

Figure 2.9: Impact of N_2O mechanism -- EGR sweep

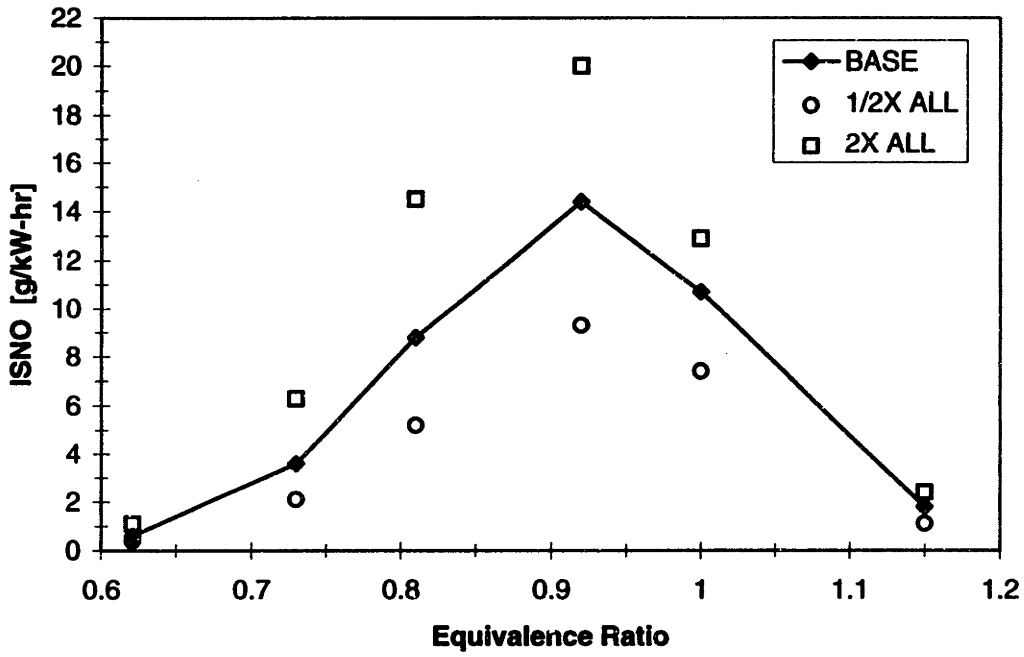

Figure 2.10: Effect of changing the reaction rates of the complete Zeldovich mechanism on NO formation -- equivalence ratio sweep

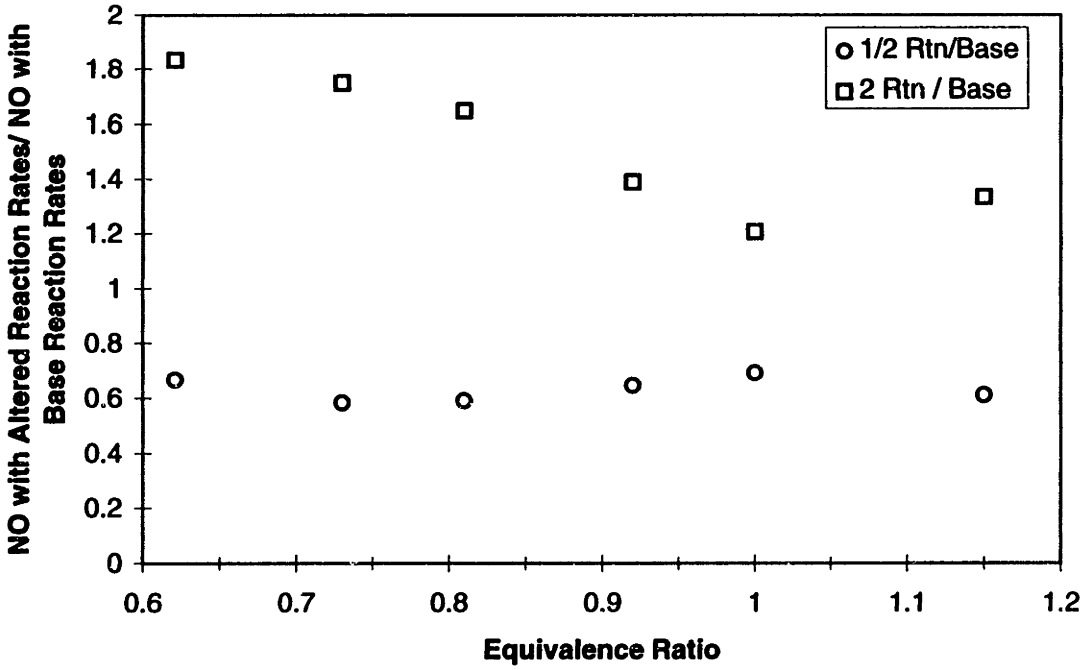

Figure 2.11: Sensitivity of NO formation rate to reaction rate over equivalence ratio

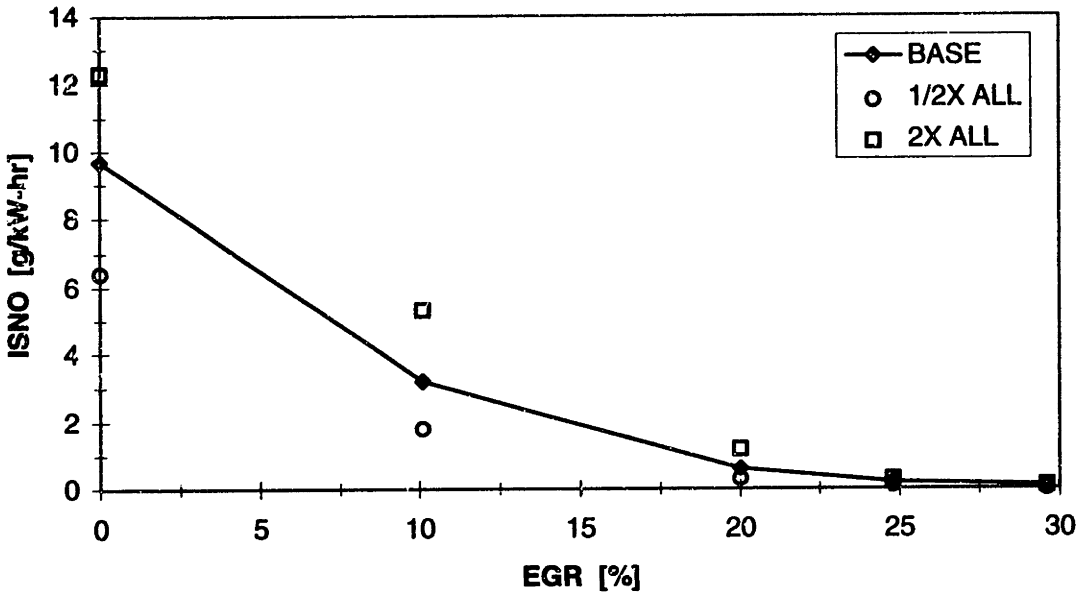

Figure 2.12: Effect of changing the reaction rates of the complete Zeldovich mechanism on NO formation -- EGR sweep

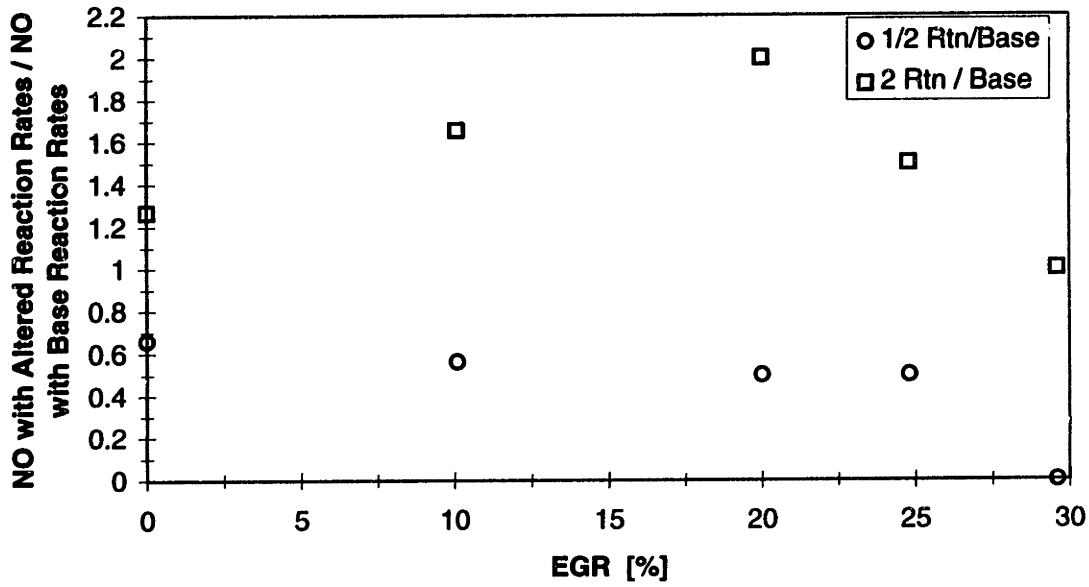

Figure 2.13: Sensitivity of NO formation rate to reaction rate—EGR sweep

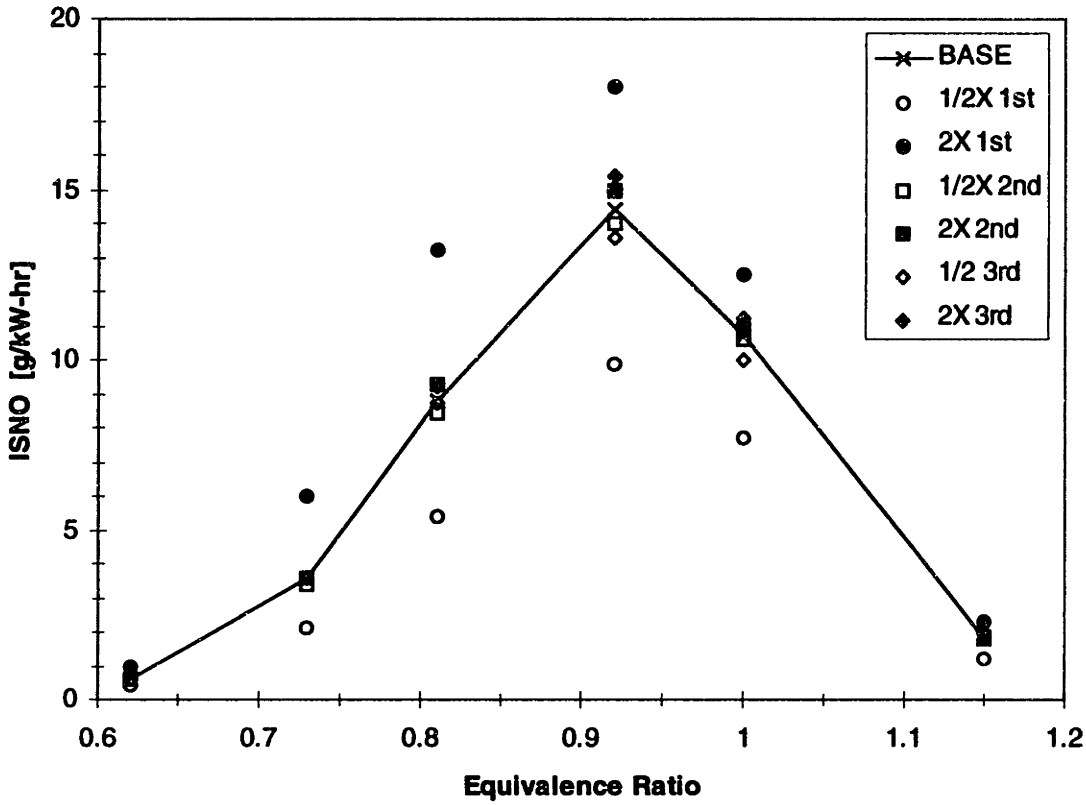

Figure 2.14: Examination of the effect of changing the reaction rate for individual reactions of the Zeldovich mechanism

3. Thermal State Modeling

3.1 Development of Adiabatic Core and Boundary Layer Models

The two-zone combustion model, in which the cylinder charge during combustion is divided into burned and unburned zones, assumes that the corresponding temperatures within each zone are uniform and therefore may be calculated as average values. While this assumption is adequate for the unburned zone, the treatment of burned zone temperature requires further attention. Additionally, with the two-zone combustion model, heat is transferred to the cylinder walls uniformly from the entire burned gas zone. A closer representation of the physical reality would be a model which allows heat transfer from only those burned gases located in the region bordering the cooler cylinder walls. The charge in the center of the burned zone would be considered to be unaffected directly by the heat transfer.

The above considerations justify the implementation of a "three-zone" model. The unburned zone would be present as before, but what was previously treated as a homogeneous burned zone is now divided into an adiabatic core and a thermal boundary layer. This is illustrated in Figure 3.1. The adiabatic core contains the hot cylinder gases and, by definition, does not undergo any heat transfer. As the heat transfer interaction occurs, the cooler thermal boundary layer grows with time by absorbing mass from the core. The temperature of the thermal boundary layer is determined according to:

$$T_{bl} = \frac{T_b + T_{wb}}{2} \tag{3.1}$$

wherein T_b is the temperature of the burned zone and T_{wb} is an area weighted mean temperature derived from the wall temperatures in the burned zone. The temperature of the adiabatic core is found using the relationship:

$$x_b h_b = x_{bl} h_{bl} + x_{ac} h_{ac} \tag{3.2}$$

wherein x_i represents the mass fraction of that particular zone. The value of h_{ac} determined in this way is used in conjunction with the cylinder pressure and the composition of the adiabatic core to solve for T_{ac}. Results are illustrated in Figure 3.2

It is important to note that the thermal boundary layer is frozen in composition, while the adiabatic core consists of products of combustion in thermodynamic equilibrium. This is crucial to the NO formation analysis. This thermal boundary layer grows with time, as illustrated in Figure 3.3, according to:

$$\dot{x}_{bl} = \frac{(1-\frac{x_{bl}}{x_b})(A_{bl} x_{bl} (\dot{T}_{bl} - \frac{B_{bl}}{\rho_{bl} A_{bl}} [\frac{\partial \rho_{bl}}{\partial T_{bl}} \dot{T}_{bl} + \frac{\partial \rho_{bl}}{\partial p_{bl}} \dot{p}] + \frac{\dot{Q}_{wb}}{m}))}{h_b - h_{bl}} \tag{3.3}$$

where the variables A_{bl} and B_{bl} are as defined as in Equations 2.5 and 2.6.

For the adiabatic core, the NO formation equation has the same form as Equation 2.12 presented before, but with the properties and concentrations specific to the adiabatic core region, i.e.:

$$\frac{d\{NO\}_{ac}}{dt} = \frac{2 M_{NO} R_1 (1-\alpha^2)}{\rho_{ac} (1+K\alpha)} \tag{3.4}$$

The quantity $\{NO\}_{ac}$ refers to the mass fraction of NO in the adiabatic core. Please refer to Equation 2.16 for the explicit definition of the other variables.

NO formation in the thermal boundary layer is not modeled in the same way due to its low temperature. For the thermal boundary layer case, the composition is assumed to be frozen, and therefore its NO concentration is due entirely to the mass transferred from the adiabatic core as the boundary layer grows. Hence,:

$$\frac{d\{NO\}_{bl}}{dt} = \frac{\dot{m}}{m_{bl}}\{NO\}_{ac} \qquad (3.5)$$

wherein $\{NO\}_{bl}$ is the mass fraction of NO in the thermal boundary layer.

The mass fraction of NO in the entire cylinder mixture, including both the burned and unburned zones, is determined by:

$$\{NO\} = \frac{\{NO\}_{ac} m_{ac} + \{NO\}_{bl} m_{bl}}{m_{ac} + m_{bl} + m_u} \qquad (3.6)$$

The results of this analysis are illustrated and discussed further in Section 5.2.

3.2 Unmixed Modeling of the Burned Charge

An unmixed, or layered, representation of the burned charge was implemented in order to more appropriately match actual conditions in the cylinder gases. It has been previously documented in the literature [22] that temperature gradients exist in the burned gases, with regions burning early in the combustion process obtaining temperatures 400 K higher than those of the final burning regions. The "fully mixed model" used previously does not account for this stratification; rather, in this case the burned zone is assumed to be uniform in temperature and is characterized as such by $T_b = \overline{T}_b$. Hence, as charge

burns, it is assumed to instantaneously mix with the previously burned gas. The "unmixed model," on the other hand, does not treat the burned zone as a homogeneous mixture of gases. Instead, the unmixed model works upon the assumption that no mixing occurs between the layers or shells of sequentially burning gas elements. The amount of charge that burns within a specified time interval (such as a crank angle) remains a discrete layer which does not mix with the other layers in the burned zone. Of course, the true reality of burned zone behavior lies somewhere in between these limits of complete mixing and no mixing. However, the layered model captures the documented progressive nature of burned zone growth (Figure 3.5).

Figure 3.6 outlines the specifics of unmixed burned zone modeling. As the flamefront moves through the cylinder charge between time t_j and time t_k, a layer (labeled B) composed of the newly burned mass, is formed. Layer B will experience no heat or mass transfer with layer A which formed before it, or with layer C which will develop after it. These layers will undergo isentropic compression or expansion according to the rising or falling of the cylinder pressure, thereby maintaining their independent temperature and composition identities. For convenience, it is the time duration in which burning mass which may contribute to a developing layer which is kept constant. As with the fully mixed model, cylinder pressure is assumed to be constant throughout the cylinder gases. The supporting equation for the layered burn process is as follows:

$$\frac{T_b(t_i, t_j)}{T_b(t_i)} = \left[\frac{p(t_j)}{p(t_i)}\right]^{\frac{\gamma_b - 1}{\gamma_b}} \qquad (3.7)$$

where $T_b(t_i,t_j)$ is the temperature of the element at pressure $p(t_j)$ which had burned at pressure $p(t_i)$. For simplicity, the specific heat ratio γ_b is the average value for the burned zone at that time. The temperature of the newly burned element $T_b(t_i,t_i)$ is obtained from the relationship:

$$h_b(T_b, p) = h_u(T_u, p) \tag{3.8}$$

Since the enthalpy of the unburned zone h_u, the cylinder pressure p, and charge composition is known, sufficient information is available to utilize the thermodynamic property routines of the cycle simulation in order to calculate $T_b(t_i,t_i)$. Use of the unmixed model in the burned zone does not affect the calculation procedures of unburned zone temperature and properties which are performed as discussed in Chapter 2.

Corresponding to the temperature gradient that develops in the unmixed burned zone model, a species concentration gradient forms as well (Figure 3.7). As explained in Chapter 2, NO production is a function of temperature. Therefore, since each layer has a distinct temperature, it also has a distinct NO concentration. The overall mass fraction of NO in the burned zone, $\{NO\}_b$,at a particular instant in time is determined from:

$$\{NO\}_b = \frac{\sum_i m_i \{NO\}_i}{\sum_i m_i} \tag{3.9}$$

wherein m_i and $\{NO\}_i$ represent the mass and mass fraction of NO in slice i , respectively. The summation of all of the m_i comprises the entire burned zone mass at that particular time step. The calculation of $\{NO\}_i$ merits some explanation. As it

would be impractical to numerically integrate the NO formation equations for each layer due to their large, variable number, the approach presented in Chapter 2 had to be modified. The differential equation for the rate of change of NO mass fraction in the burned zone was discretized according to:

$$\frac{d\{NO\}_b}{dt} = \frac{\{NO\}_b{}^{t_n} - \{NO\}_b{}^{t_{n-1}}}{t_n - t_{n-1}} \qquad (3.10)$$

By setting $\Delta t = t_n - t_{n-1}$ and by algebra, one may write:

$$\{NO\}_b{}^{t_n} = \{NO\}_b{}^{t_{n-1}} + \frac{d\{NO\}_b}{dt}\Delta t \qquad (3.11)$$

where $\{NO\}^{tn}$ is the mass fraction of NO in a particular slice at time t_n. This calculation is performed for every slice. The equation for the time rate of change of {NO}is the same as Eqn. 3.4, discussed previously.

It is important to recognize that though the unmixed model does more properly capture the physics of the combustion process in the engine cylinder, it is truly applicable to the burned gas located away from the cylinder walls. Since a major assumption of the unmixed model as presented above is the isentropic compression and expansion of the burned zone gases, it fails to account for the significant heat transfer between the cooler cylinder walls and hotter combustion gases near them. Hence, the layered model is physically justifiable only if used in conjunction with the adiabatic core and thermal boundary layer model discussed in Section 3.3.

3.3 Issues Associated with Combining Three-Zone and Unmixed Burned Zone Models

The key to the union of these models -- the three-zone representation of the cylinder gases (i.e. unburned, adiabatic core, and thermal boundary layer zones) and the unmixed burned zone model -- is that while the boundary layer and adiabatic core growth proceeds as before, with the inclusion of the unmixed model, the adiabatic core is now layered. Equations for boundary layer growth remain the same, as well as those governing boundary layer temperature. Now, however, temperature and NO concentration profiles in the adiabatic core are calculated according to the unmixed model equations. Note that the amount of mass in each layer decreases as the boundary layer grows. Care had to be taken to develop a procedure to determine how much mass from each layer was lost to the boundary layer for each time interval. Since the layers are not of equal mass (instead for programming convenience, they are generated in equal time intervals), an extra degree of difficulty is added to the problem. Too simplistic a procedure, such as removing equal amount of mass from each layer, could result in erroneously taking more mass from a layer than available. The calculation procedure is as follows:

for slice i at time n,

$$m_i|_n = m_i|_{n-1} - \Delta m_i \qquad (3.12)$$

$$\sum \Delta m_i = m_{out} \qquad (3.13)$$

$$\sum m_i|_{n-1} = m|_{n-1} \qquad (3.14)$$

$$C = \Delta m_i / m_i|_{n-1} \quad (3.15)$$

$$\sum (\Delta m_i = C\, m_i|_{n-1}) \quad (3.16)$$

$$\sum \Delta m_i = C \sum m_i|_{n-1} \quad (3.17)$$

$$C = \sum \Delta m_i / \sum m_i|_{n-1} = m_{out} / m|_{n-1} \quad (3.18)$$

$$\Delta m_i = (m_{out} / m|_{n-1})\, m_i|_{n-1} \quad (3.19)$$

$$m_i|_n = m_i|_{n-1} (1 - [m_{out} / m|_{n-1}]) \quad (3.20)$$

Calculation of NO mass fraction in the adiabatic core proceeds as discussed in Section 3.2, except, of course, with the only mass being treated in this manner being that of the adiabatic core. To determine NO concentration in the boundary layer, the NO mass fraction pertaining to a particular slice is correspondingly transferred with the mass of that slice which is lost to the boundary layer. The total NO concentration in the boundary layer is found by adding the products of the masses contributed by each slice and their associated NO mass fractions. This is illustrated and discussed further in Chapter Five.

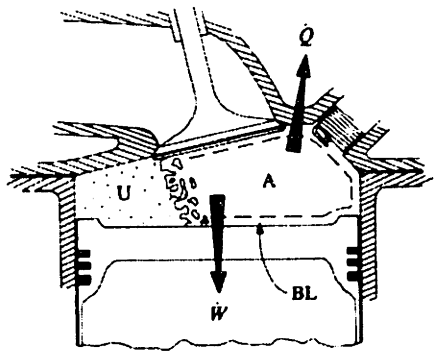

Figure 3.1: Three zone representation of cylinder contents during combustion [16]

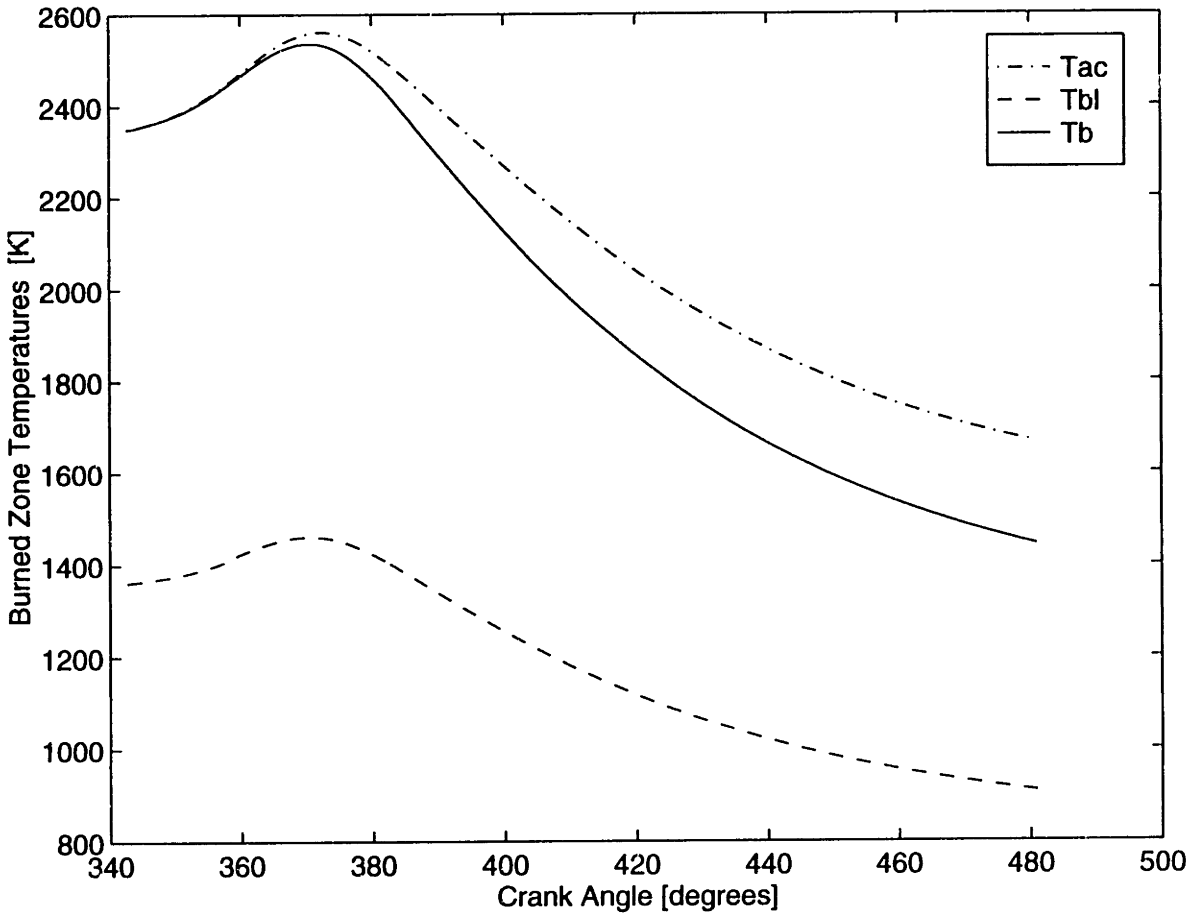

Figure 3.2: Temperature distribution in the burned zone

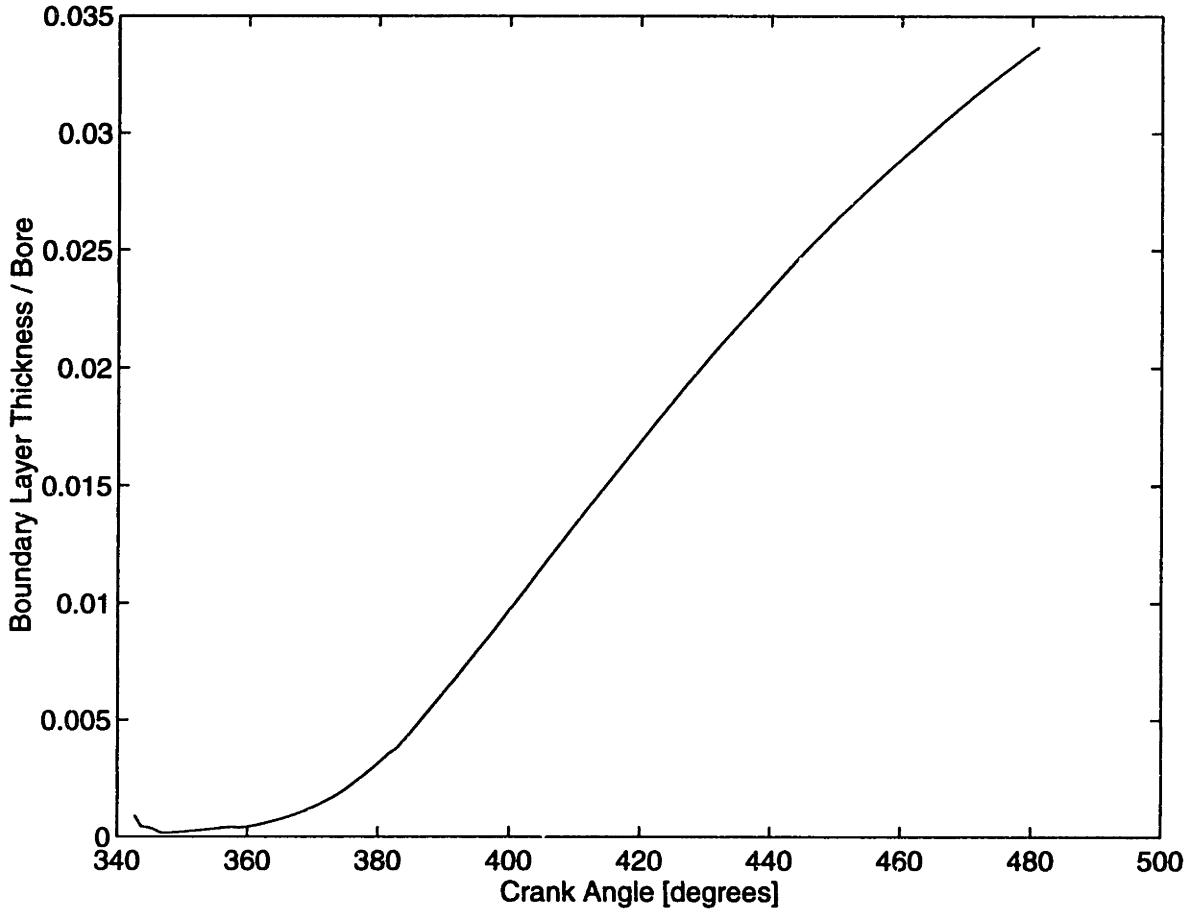

Figure 3.3: Thermal boundary layer development

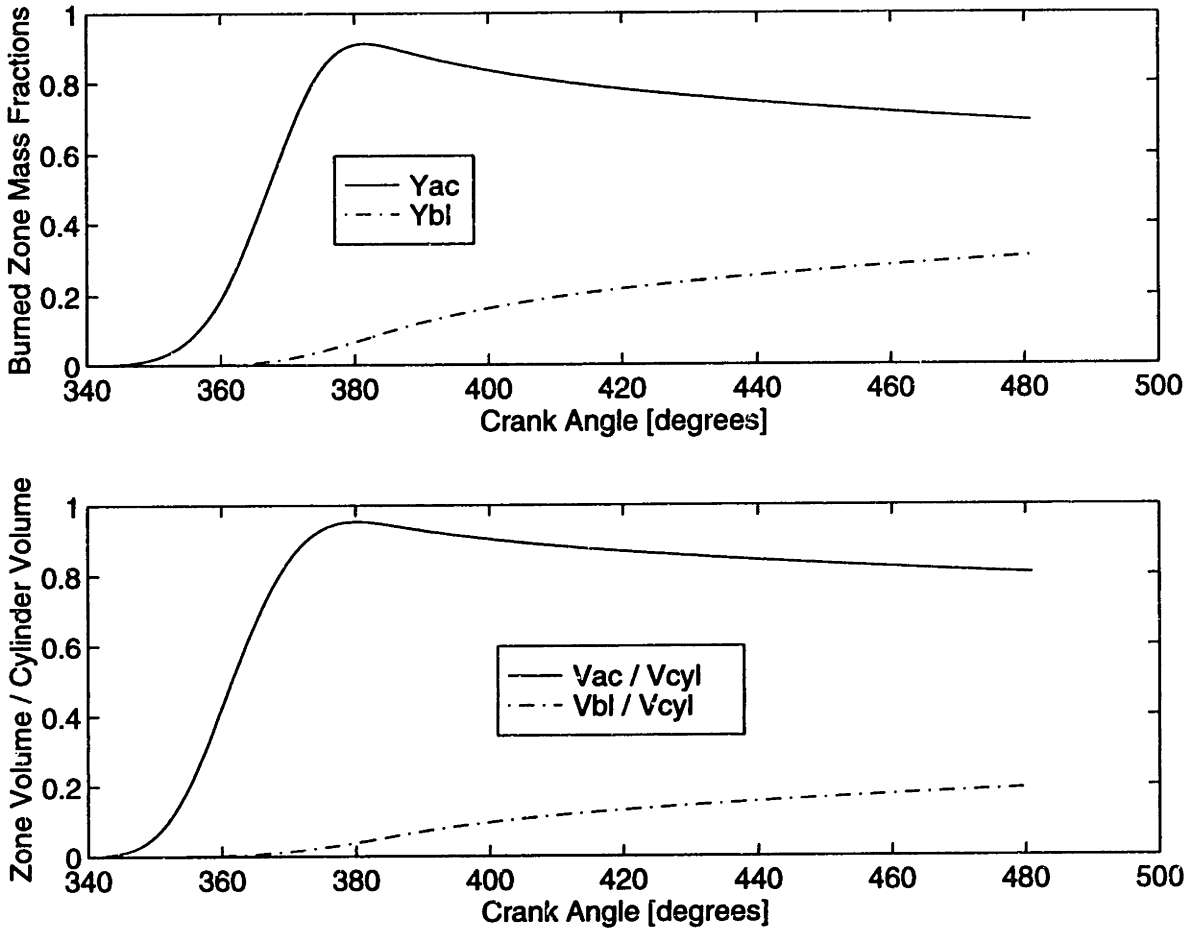

Figure 3.4: Growth of the thermal boundary layer illustrated through boundary layer thickness and volume

BASE

BOUNDARY LAYER MODEL

BOUNDARY LAYER AND
LAYERED BURN MODEL

Figure 3.5: Model definition and evolution

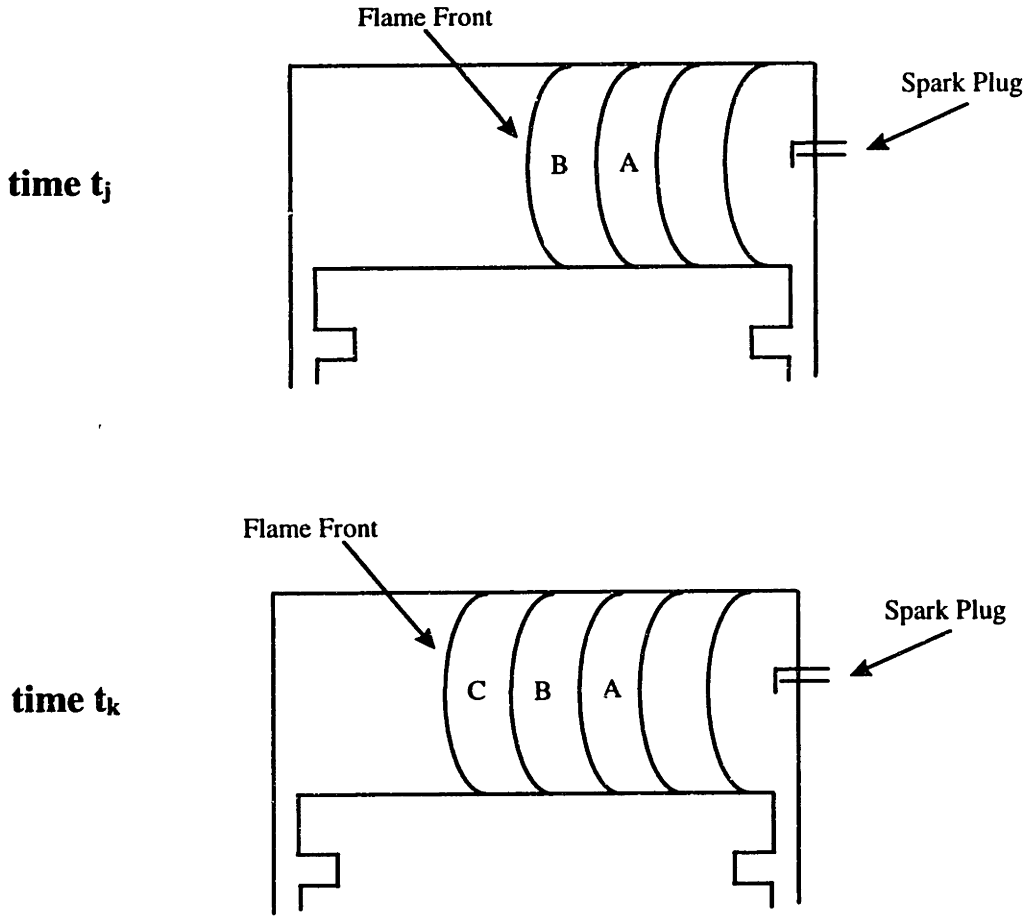

Figure 3.6: Unmixed burned zone modeling

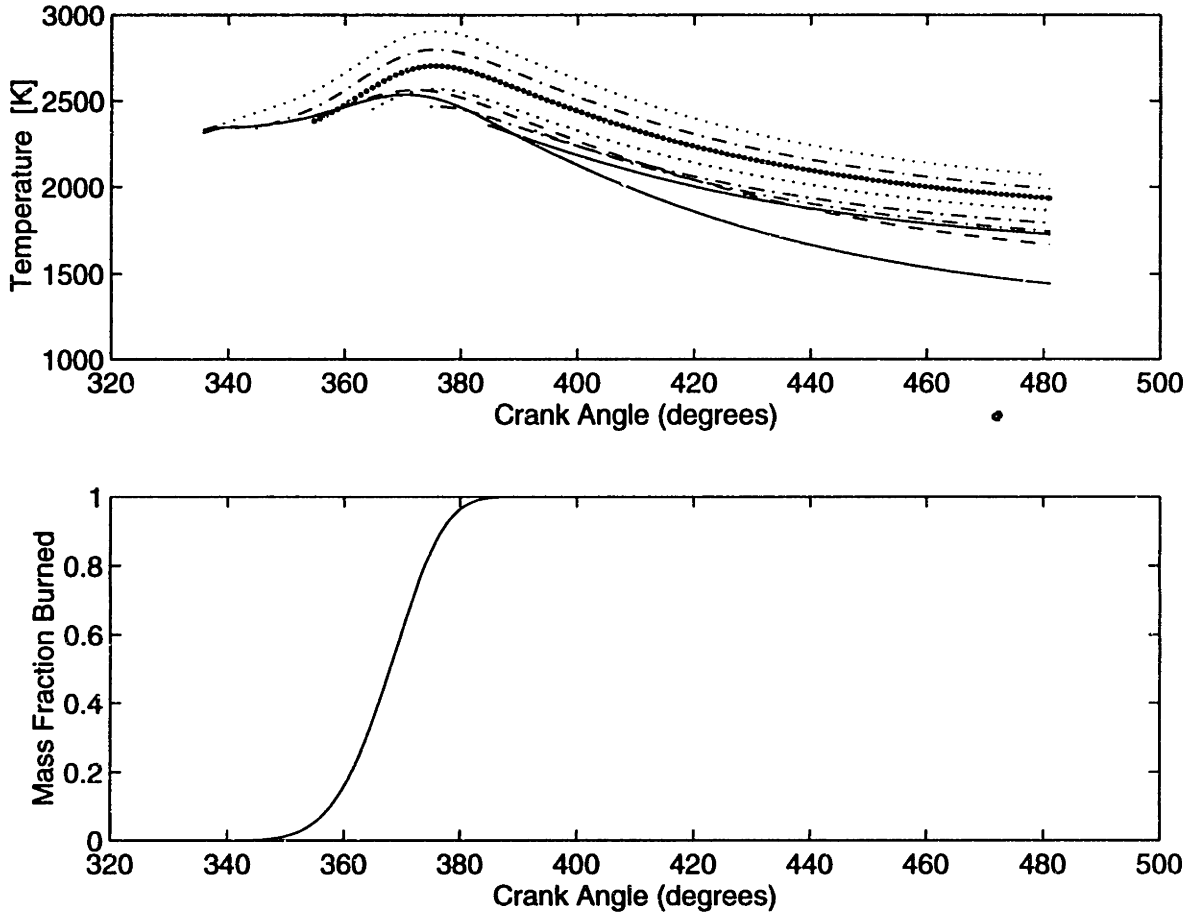

Figure 3.7: Temperature Distribution in the Engine Cylinder Due to Layered Burn Combustion Modeling of the Adiabatic Core

4. The Crevice Gas Model

4.1 Crevice Definition

Crevices are narrow regions in the engine combustion chamber into which charge may enter but the flame is unable to penetrate. As cylinder pressure rises, charge mixture is pushed into these crevices; likewise, as cylinder pressure decreases, crevice gases will reenter the combustion chamber. Due to the quenching of the flame at the crevice entrance, unburned mixture which enters the crevices escapes the normal combustion process. This phenomenon results in reduced pressures and burned gas temperatures in the combustion chamber, since the amount of charge participating in the combustion process has been affected. An increase in hydrocarbon emissions and a decrease in power and efficiency due to the crevice effect has been documented [7, 26].

Overall, crevices are located in several areas of the combustion chamber, which include the piston top-land region, spark plug thread, and head gasket. These locations are illustrated in Figure 4.1. Though crevices comprise only 1-2% of the cylinder clearance volume, crevices contain between 4-6% of the cylinder fuel-air mixture at peak pressure. Crevices are able to house such a significant portion of mass since crevice gases are cooler than those in the cylinder and therefore have a higher density. The composition of the crevice gases changes throughout the cycle. Before combustion, the gas flowing into the crevices is the same mixture of fuel, air, residual gas, and EGR that is present in the engine cylinder. After combustion begins and before cylinder peak

pressure, crevice gas flow will be some combination of unburned and burned charge, depending upon spark plug location (see Section 4.3). The maximum amount of mass in the crevices corresponds to the time of peak pressure in the cylinder. After peak pressure, the direction of crevice gas flow reverses, returning the crevice gas to the engine cylinder.

4.2 Model Assumptions

The piston top-land crevice region is the largest, accounting for more than 35% of the total crevice volume. As a result, for computational simplicity, this crevice type was selected to represent all combustion chamber crevice locations in this modeling effort; the physical phenomena modeled correspond directly to the top-land crevice.

The crevice volume is assumed to remain constant throughout the entire cycle. Though the crevice volume will decrease as the walls expand with increasing wall temperature, the constant-volume assumption is sufficient for the level of detail required for this model.

Gas in the crevice is assumed to be ideal and isothermal, with temperature as defined by the average of the piston and cylinder wall temperatures, i.e.:

$$T_{crv} = \frac{T_{piston} + T_{wall}}{2} \tag{4.1}$$

This definition is not strictly true, but the small size of the crevice makes this a legitimate assumption. The crevice gas pressure is usually almost equal to the cylinder gas pressure and is therefore also always uniform at any instant in time.

Unlike the cylinder gases during combustion, the crevice gas is not divided into burned and unburned regions. Any element of gas that enters the crevice zone is assumed

to mix instantaneously with the gases already present in the crevice. The computations behind this "fully mixed" crevice gas assumption are discussed further in Section 4.4. Though the crevice gases are assumed to be fully mixed, a strict accounting of crevice gas composition is still required in order to properly model the crevice phenomenon. This procedure, in addition to other modeling requirements, are discussed in the following sections of this chapter.

4.3 The Effect of Spark Plug Location on Crevice Gas Composition

The degree of the effect that crevices have on NO formation lies in the amount of unburned fuel which resides in the crevice during the combustion process; the location of the spark plug in the combustion chamber largely determines crevice gas composition. Figure 4.2, which depicts a center spark plug location, shows that as the cylinder pressure rises, unburned fuel will enter the crevices. If the flamefront moves quickly enough to reach the opposite end of the chamber while the cylinder pressure is still rising, then burned fuel will also be pushed into the crevices before they begin to empty. The specific combination of burned and unburned fuel amounts will change with a different spark plug position. A plug located on the side of the combustion chamber, for example, will cause some portion of the crevice inflow to be burned gas almost immediately after combustion begins. Hence, as the spark plug is moved away from the center position, the unburned fraction of gas entering the crevices decreases (Figure 4.3). This affects the NO formation calculation, since previously burned gas which enters the crevices has already participated in the combustion process and contributed to NO formation in the engine

cylinder. It is the unburned portion of crevice gas which escapes normal combustion and does not contribute to NO formation as would have been the case with a non-crevice model.

Three spark plug locations consisting of center, midway, and side (Figure 4.4) were selected to represent the entire range of effects spark plug location has on NO formation. A simple routine was developed to determine the change in crevice gas composition as a function of spark plug location. With this information, NO formation calculations could be performed with the appropriate concentration of unburned gas remaining in the engine cylinder. The crevice gas composition calculations were built upon a procedure developed by Namazian and Heywood [27].

4.4 Determination of Crevice Gas Flow Composition

A simple planar representation of a flamefront propagating in a combustion chamber with a "midway" spark plug location is illustrated in Figure 4.5. The flamefront traverses the chamber in circular "shells." A shell representing the flamefront early in the combustion stroke will have a smaller flame radius (r_f) than a flamefront which models conditions later in the combustion stroke. Note, however, that all shells emanate from the same origin – the spark plug location. The chamber circumference (L) is the entrance to the crevice regions.

At a particular instant during the combustion stroke, the portions of the circumferential crevice entrance bordered by burned gas and unburned gas are labeled L_b and L_u, respectively. Assuming that the mass flow rate per unit area into the crevice is uniform

over its entirety, the amount of burned gas entering the crevice region at this instant in time is:

$$\dot{m}_{b_{crv}} = \dot{m}_{crv} \frac{L_b}{L} \tag{4.2}$$

wherein

$$\dot{m}_{crv} = \dot{m}_{b_{crv}} + \dot{m}_{u_{crv}} \tag{4.3}$$

is the total mass flow into the crevice entrance plane. Similarly, the unburned gas flow into the crevice plane is:

$$\dot{m}_{u_{crv}} = \dot{m}_{crv} \frac{Lu}{L} \tag{4.4}$$

since

$$L = L_b + L_u \tag{4.5}$$

From these relationships, the fraction of crevice mass flow entering the crevices which is burned ($x_{b\ flow}$) and the fraction which is unburned ($x_{u\ flow}$) at a particular instant in time may be defined as:

$$x_{bflow} = \frac{L_b}{L} \tag{4.6}$$

$$x_{uflow} = \frac{L_u}{L} \tag{4.7}$$

As combustion progresses, the value of $x_{u\ flow}$ will decrease and the value of $x_{b\ flow}$ will increase. These values are needed at each relevant timestep during combustion in order to calculate the amounts of burned and unburned gases in the crevices. Additionally, this information is also needed for the "center" and "midway" spark plug location geometries.

The methodology employed, though only a simplification, correctly captures the physical realities for each of the plug geometries.

Using the burned gas volume (V_b) calculated in the cycle simulation, and estimating that

$$V_b = \pi r_f^2 \bar{h} \tag{4.8}$$

where $\bar{h}$, a calculated geometric parameter, is the mean clearance height between the piston top and the cylinder chamber end. It is assumed to be constant throughout combustion. Through algebra:

$$r_f = \sqrt{\frac{V_b}{\pi \bar{h}}} \tag{4.9}$$

Hence, r_f is now known for each time step.

With simple geometric relations, the length of arc segment L_b in Figure 4.5 may be calculated once r_f and angle θ are known. Angle θ, and therefore length L_b were determined for a number of values of r_f within the appropriate range for the side plug case, i.e.: $0 \leq r_f \leq 2r_o$. A fourth order polynomial equation was used to model the relationship between r_f and $x_{b\ flow}$ which is equivalent to L_b/L). Hence, since the value of r_f is known at each time step, the value of $x_{b\ flow}$ is also known.

The same procedure was employed for the center and midway spark plug location cases, with limits on r_f corresponding to the individual geometries. Hence, for the center plug location:

for $r_f < r_o$, then $L_b = 0$ and $x_{b\ flow} = 0$

for $r_f = r_o$, then $L_b = L$ and $x_{b\ flow} = 1$

and for the midway spark plug location:

for $r_f < r_o/2$, then $L_b = 0$ and $x_{b\ flow} = 0$

for $r_o/2 \leq r_f \leq 3r_o/2$, then $0 < L_b \leq L$ and $0 < x_{b\ flow} \leq 1$

Before leaving this topic, it is worthwhile to reiterate that the calculation procedure presented only defines the burned and unburned portions of the crevice mass flow stream into the crevices for a particular timestep. This procedure applies to crevice flow only before peak pressure, since the burned and unburned fractions of crevice outflow are determined by the contents of the crevices themselves. This calculation of the burned and unburned mass fractions of the gas within the crevice itself (the "crevice gas") is another matter, discussed in Section 4.5.

4.5 Determination of Crevice Mass Composition

As discussed in Section 4.4, the burned fraction of gas flow entering the crevice region before peak pressure is a function of spark plug location and flamefront position. As a result, the burned mass fraction of the crevice gas ($x_{b\ crv}$) is by no means constant or equivalent to the mass fraction burned of the cylinder gases ($x_{b\ cyl}$). A differential equation was developed to determine the rate of change of burned mass fraction in the crevices.

Starting with the definition of burned gas fraction in the crevices ($x_{b\ crv}$):

$$x_{b_{crv}} = \frac{m_{b_{crv}}}{m_{crv}} \tag{4.10}$$

and differentiating, using the quotient rule:

$$\dot{x}_{b_{crv}} = \frac{\dot{m}_{b_{crv}} - \dot{m}_{crv} x_{b_{crv}}}{m_{crv}} \tag{4.11}$$

From Section 4.4, before peak pressure:

$$\dot{m}_{b_{crv}} = \dot{m}_{crv} x_{bflow} \tag{4.12}$$

and therefore with substitution of Eqn. 4.13 into Eqn. 4.12,

$$\dot{x}_{b_{crv}} = \frac{\dot{m}_{crv} x_{bflow} - \dot{m}_{crv} x_{b_{crv}}}{m_{crv}} \tag{4.13}$$

This equation is solved simultaneously at every timestep. Note that after peak pressure the burned crevice mass is constant, i.e.:

$$\dot{x}_{b_{crv}} = 0 \tag{4.14}$$

It remains at its peak pressure value since gases then begin to exit the crevices at this fixed composition.

4.6 Determination of Crevice Gas Properties

The same thermodynamic property calculation subroutines are used for the crevice gases as they are for the cylinder contents, with appropriate temperatures, enthalpies, etc., for crevice conditions. A unique situation arises with the case of combustion/expansion, since during this interval, the crevice gases are not separated into burned and unburned zones as the chamber gases are. This difference adds complexity to the modeling task

because the selection of an appropriate thermodynamic property calculation routine is based upon whether or not the gases under analysis are burned or unburned.

To circumvent this issue, only the unburned gas property routines are employed in crevice gas property calculations. For all plug locations considered, the large majority of crevice gas is unburned. This simplification is in keeping with the physically-based modeling approach of this research effort, while at the same time it avoids the unwarranted computational difficulty required to separate the crevice gas into two zones.

4.7 Crevice Model Construction

As is the physical reality, the crevice model is active during the entire cycle. During the intake and compression strokes, the crevices fill with the appropriate amount and combination of fuel, air, residual gas, and EGR. During exhaust, any gas remaining in the crevices is treated as completely burned, as this had already been assumed for the cylinder charge. A critical focus of the crevice model development was that the model be able to operate in conjunction with the other combustion submodels already in place (e.g. the thermal boundary layer/adiabatic core division and layered burn representation). This union occurs in several steps during combustion. First, at each crank angle, crevice inflow and outflow operates with the burned and unburned zones in the cylinder before division into adiabatic core and thermal boundary layer occurs. The necessary calculations required to set up the differential equations for crevice mass flow and composition are therefore performed with average cylinder properties, such as burned zone temperature. Only after this procedure is completed does the development of a

thermal boundary layer begin and combustion continues as described in Section 3.2, with the adiabatic core modeled with a layered burn representation.

As had been indicted above, the source (before peak pressure) and the recipient (after peak pressure) of crevice mass flow during combustion are the burned and unburned zones in the cylinder. Once the appropriate combination of burned and unburned mass flowing into the crevices has been determined (see Section 4.4), the burned and unburned zones in the cylinder are reduced accordingly. The mixture in the crevices is assumed to be homogeneous and hence no separation into burned and unburned zones occurs. A differential equation was constructed, however, to account for the changing composition of the crevice gases. Once crevice outflow into the combustion chamber begins, the unburned fraction of the stream will recombine with the unburned zone in the cylinder; the burned mass fraction of the stream will likewise go to the burned zone in the cylinder. This created a computational problem – at the end of combustion with all of the charge burnt, the unburned mass returning from the crevices no longer had a zone with which it could combine. Hence, to avoid a calculation error, the unburned zone volume in the cylinder could not be allowed to ever equal exactly zero. Consequently, an upper limit on the burned mass fraction ($x_{b\,comb}$) in the cylinder had to be imposed; the value was defined to be $x_{b\,comb} = 0.9995$. This limitation enables a small unburned zone to exist without impeding the physical representation of the combustion process.

4.8 Governing Equations Including Crevice Effects

The fundamental principles presented earlier still apply when crevice effects are included; the crucial difference is that as a result of the crevice model, cylinder mass

flows may no longer be treated as independent of pressure. As cylinder pressure rises, cylinder mass will be forced into the crevices; as it decreases, crevice mass will return to the chamber. Accordingly, the composition of this crevice mass flow (and hence the cylinder mass) will be changing as well. The differential equations used for the non-crevice case had to be modified and additional differential equations had to be added. To understand the transition of the system of equations to be solved, the unknown variables pertaining to combustion without the crevice effect should first be examined. These unknown variables may be placed in a vector:

$$\eta_{\text{no crevice}} = [p_{cyl}, T_{cyl}, V_{cyl}, x_{b\ comb}] \tag{4.15}$$

where $x_{b\ comb}$ refers to the mass fraction burned in the cylinder due to combustion. With the inclusion of the crevice effect, new variables had to be included in the unknown variable vector, i.e.:

$$\eta_{\text{with crevice}} = [p_{cyl}, T_{cyl}, V_{cyl},, x_b, m_{crv}, x_{b\ crv}, x_{b\ total}] \tag{4.16}$$

where m_{crv} refers to the mass in the crevice, $x_{b\ crv}$ refers to the burned mass fraction in the crevices, and $x_{b\ total}$ refers to the burned mass fraction in the cylinder due to combustion, crevice inflow, and crevice outflow. Hence the solution methodology is now:

$$\frac{\partial \eta}{\partial t}[\eta] = [b] \tag{4.17}$$

$$\eta = [b][\frac{\partial \eta}{\partial t}]^{-1} \tag{4.18}$$

The development and solution of these equations will now be discussed in detail. Recall that an important requirement of the derivation is to obtain a rate of change of temperature equation which is independent of the unknown rate of change of pressure.

First, the crevice gas is treated as ideal and uniform in composition. This enables one to write:

$$m_{crv} = (\frac{pV}{RT})_{crv} \tag{4.19}$$

and, since it is assumed that the pressure in the cylinder (p) is equal to the pressure in the crevice (p_{crv}), then this expression becomes:

$$m_{crv} = p(\frac{V}{RT})_{crv} \tag{4.20}$$

Assuming that the rate of change of the gas constant R_{crv} may be neglected, and because the crevice temperature T_{crv} and volume V_{crv} are constant,

$$\dot{m}_{crv} = (\frac{\dot{p}}{p})m_{crv} \tag{4.21}$$

Crevice mass flow is defined as positive when the crevice mass flow is leaving the cylinder and entering the crevice. The cylinder mass flow expression must now include the crevice flow, hence:

$$\begin{aligned} \dot{m} &= \dot{m}_{in} - \dot{m}_{out} - \dot{m}_{crv} \\ &= \dot{m}_{in} - \dot{m}_{out} - (\frac{\dot{p}}{p})m_{crv} \\ &= d^* - c^* \dot{p} \end{aligned} \tag{4.22}$$

The substitutions with the * terms are made to maintain clarity as the complexity of the derivation increases. Note that the selection of the * terms highlights the dependency of mass flow on the rate of change of pressure.

The equation for x_1, the mass fraction of fresh charge in the cylinder,

$$x_1 = \frac{m_1}{m} \tag{4.23}$$

when differentiated gives:

$$\dot{x}_1 = \frac{\dot{m}_1 - \dot{m}x_1}{m}. \tag{4.24}$$

Let us examine this equation term by term. First, the mass flow of fresh charge entering the system is:

$$\dot{m}_1 = \sum \dot{m}_j x_{1\,j} \tag{4.25}$$

where x_{ij} is the mass fraction of fresh charge in the jth flow. Hence, the equation may be expressed as:

$$\dot{m}_1 = \dot{m}_{in}[(1 - \frac{EGR}{100})(flag) + x_1(1 - flag)] - \dot{m}_{out}x_1 - \dot{m}_{crv}x_1 \tag{4.26}$$

where flag = 1 represents fresh charge (air, fuel, EGR) and flag = 0 refers to the cylinder gases in the intake manifold returning into the cylinder. The mass fraction of fresh charge for flows both entering and leaving the crevice is assumed to be the equivalent to the cylinder fresh charge fraction during intake.

Since the crevice mass flow rate depends on the rate of change of pressure, this equation may also be written as:

$$\dot{m}_1 = \dot{m}_{in}[(1 - \frac{EGR}{100})(flag) + x_1(1 - flag)] - \dot{m}_{out}x_1 - \frac{\dot{p}}{p}m_{crv}x_1 \tag{4.27}$$

By substituting Eqns. 4.26 and 4.27 into the expression for the rate of change of fresh charge fraction (Eqn. 4.24) , one obtains:

$$\dot{x}_1 = \frac{\dot{m}_{in}[(1-\frac{EGR}{100})(flag)+x_1(1-flag)]-\dot{m}_{out}x_1-\frac{\dot{p}}{p}m_{crv}x_1-(\dot{m}_{in}-\dot{m}_{out}-\frac{\dot{p}}{p}m_{crv})x_1}{m}$$

(4.28)

and using the dummy variables a* and b*, this my be written as:

$$\dot{x}_1 = a^* - b^* \dot{p} \tag{4.29}$$

but it is clear with algebra that:

$$\dot{x}_1 = \frac{\dot{m}_{in}[(1-\frac{EGR}{100})-x_1](flag)}{m} \tag{4.30}$$

Therefore, b* = 0 since the only time x_1 is changing is when fresh charge is entering the cylinder. The crevice flow is always assumed to be the same composition as the cylinder gases; further, at the start of compression the composition of the crevice gas is the same as the cylinder gas composition.

Recall Equation 2.2, rewritten here:

$$\dot{p} = \frac{\rho}{\partial\rho/\partial p}[(\frac{R_1-R_2}{R})\dot{x}_1+\frac{\dot{m}}{m}-\frac{\dot{V}}{V}-\frac{\partial\rho}{\partial T}\frac{\dot{T}}{\rho}] \tag{4.31}$$

Inclusion of the crevice model causes the mass flow rate and the rate of change of fresh charge fraction to depend on the rate of change of pressure. The equation must be restructured so that all of the rate of change of pressure terms are isolated. So, from:

$$\dot{p} = \frac{\rho}{\partial\rho/\partial p}[(\frac{R_1-R_2}{R})(a^*-b^*\dot{p})+(\frac{d^*-c^*\dot{p}}{m})-\frac{\dot{V}}{V}-\frac{\dot{T}}{\rho}\frac{\partial\rho}{\partial T}] \tag{4.32}$$

and with algebra:

$$\dot{p} = \frac{[(\frac{R_1 - R_2}{R})a^* - \frac{\dot{V}}{V} - \frac{\dot{T}}{\rho}\frac{\partial \rho}{\partial T} + \frac{d^*}{m}]}{\frac{\partial \rho / \partial p}{\rho} + b^*(\frac{R_1 - R_2}{R}) + \frac{c^*}{m}} \quad (4.33)$$

Defining z* to be:

$$z^* = \frac{1}{\frac{\partial \rho / \partial p}{\rho} + b^*(\frac{R_1 - R_2}{R}) + \frac{c^*}{m}} \quad (4.34)$$

the rate of change of cylinder pressure may be written as:

$$\dot{p} = z^*[(\frac{R_1 - R_2}{R})a^* - \frac{\dot{V}}{V} - \frac{\dot{T}}{\rho}\frac{\partial \rho}{\partial T} + \frac{d^*}{m}] \quad (4.35)$$

Likewise, recall Equation 2.4 which is rewritten here:

$$\dot{T} = \frac{B}{A}\left[\dot{x}_1\left(\frac{R_1 - R_2}{R} + \frac{h_2 - h_1}{B}\right) + \frac{\dot{m}}{m}\left(1 - \frac{h}{B}\right) - \frac{\dot{V}}{V} + \frac{1}{mB}\left(\sum \dot{m}_j h_j - \dot{Q}_w\right)\right] \quad (4.36)$$

Again, the expressions for the mass flow rate and the rate of change of fresh charge fraction depend on the rate of change of pressure now that the crevices are being included in the model. A new equation that account for this dependency must be developed. Returning to the First Law of Thermodynamics, using the nomenclature defined in Chapter 2,

$$\dot{m}h = \sum \dot{m}_j h_j - h\sum \dot{m}_j + V\dot{p} - \dot{Q}_w \quad (4.37)$$

The enthalpy flux term contains depends on the rate of change of pressure, i.e.:

$$\sum \dot{m}_j h_j = \dot{m}_{in} h_{in} - \dot{m}_{out} h_{cyl} - [\dot{m}_{crv} h_{cyl}(crvflag) + \dot{m}_{crv} h_{crv}(1 - crvflag)] \quad (4.38)$$

The condition crvflag = 0 indicates that flow is exiting from the crevices into the cylinder, and therefore the flow carries the enthalpy of the crevices. Likewise, crvflag = 1 represents that flow is entering the crevices from the cylinder with the enthalpy of the chamber contents. Writing this equation in terms of its pressure dependencies:

$$\sum \dot{m}_j h_j = \dot{m}_{in} h_{in} - \dot{m}_{out} h_{cyl} - \frac{\dot{p}}{p}[m_{crv} h_{cyl}(crvflag) + m_{crv} h_{crv}(1 - crvflag)] \quad (4.39)$$

$$\sum \dot{m}_j h_j = e^* - f^* \dot{p} \quad (4.40)$$

Using these definitions of a*, b*, c*, d*, e*, f*, and z* (Equations 4.22, 4.29, 4.34, 4.40), the energy balance of Eqn. 4.37 may now be written as:

$$m[(h_1 - h_2)a^* + [c_T - b^*(h_1 - h_2)]\dot{p} + c_p \dot{T}] = (e^* - f^* \dot{p}) - \dot{h}(d^* - c^* \dot{p}) + V\dot{p} - \dot{Q}_w \quad (4.41)$$

and therefore by algebra:

$$\dot{T} = \frac{\dot{p}[V - f^* + hc^* + mb^*(h_1 - h_2) - c_T m] - ma^*(h_1 - h_2) - hd^* + e^* - \dot{Q}_w}{mc_p} \quad (4.42)$$

Substituting Eqn. 4.37 for the rate of change of pressure in this equation (Eqn. 4.41) gives:

$$\dot{T} = \frac{z^*[(\frac{R_1 - R_2}{R})a^* - \frac{\dot{V}}{V} - \frac{\dot{T}}{\rho}\frac{\partial \rho}{\partial T} + \frac{d^*}{m}][V - f^* + hc^* + mb^*(h_1 - h_2) - c_T m] - ma^*(h_1 - h_2) - hd^* + e^* - \dot{Q}_w]}{mc_p} \quad (4.43)$$

In order to simplify this equation, the variable w* was defined:

$$w^* = V - f^* + hc^* + mb^*(h_1 - h_2) - c_T m \quad (4.44)$$

so now the rate of change of temperature may be expressed as:

$$\dot{T} = \frac{w*z*[(\frac{R_1 - R_2}{R})a* - \frac{\dot{V}}{V} + \frac{d*}{m}] - ma*(h_1 - h_2) - hd* + e* - \dot{Q}_w}{mc_p + \frac{w*z*}{\rho}\frac{\partial \rho}{\partial T}} \quad (4.45)$$

While this equation is valid for computations during the intake, compression, and exhaust strokes, an alternative expression needs to be developed for combustion/expansion, since this portion of the cycle brings additional complexity to the modeling task. As was the case for the "no-crevice" model, the chamber contents are divided into burned and unburned zones, with a common pressure but individual temperatures and composition. Returning again to :

$$\dot{m}h = \sum \dot{m}_j h_j - h\sum \dot{m}_j + V\dot{p} - \dot{Q}_w \quad (4.46)$$

and now using the definition:

$$\dot{m}h = mc_p\dot{T} + mc_T\dot{p} \quad (4.47)$$

These expressions apply to both the unburned zone and the burned zone in the cylinder, so:

$$\dot{m}_u h_u = m_u c_{pu}\dot{T}_u + m_u c_{Tu}\dot{p} = \sum \dot{m}_{j_u} h_{ju} - h_u \sum \dot{m}_{j_u} + V_u\dot{p} - \dot{Q}_{wu} \quad (4.48)$$

$$\dot{m}_b h_b = m_b c_{pb}\dot{T}_b + m_b c_{Tb}\dot{p} = \sum \dot{m}_{j_b} h_{jb} - h_b \sum \dot{m}_{j_b} + V_b\dot{p} - \dot{Q}_{wb} \quad (4.49)$$

and solving for the rate of change of temperature in each equation results in:

$$\dot{T}_u = \frac{\sum \dot{m}_{ju} h_{ju} - h_u \sum \dot{m}_{ju} + V_u\dot{p} - \dot{Q}_{wu}}{m_u c_{pu}} \quad (4.50)$$

$$\dot{T}_b = \frac{\sum \dot{m}_{jb} h_{jb} - h_b \sum \dot{m}_{jb} + V_b\dot{p} - \dot{Q}_{wb}}{m_b c_{pb}} \quad (4.51)$$

Expressions for the rate of change of volume for the unburned and burned zones are also needed. Since the rate of change of chamber volume is known and my be expressed as:

$$\dot{V} = \dot{V}_u + \dot{V}_b \tag{4.52}$$

and therefore through algebra, one may write:

$$\frac{\dot{V}_b}{V_b} = \frac{\dot{V} - \dot{V}_u}{V_b} = \frac{\dot{V}}{V_b} - \frac{\dot{V}_u}{V_u}\frac{V_u}{V_b} \tag{4.53}$$

the rate of change of chamber volume may also be expressed in terms of density:

$$V = \frac{m}{\rho} \tag{4.54}$$

and differentiating:

$$\frac{\dot{V}}{V} = \frac{\dot{m}}{m} - \frac{\dot{\rho}}{\rho} \tag{4.55}$$

with substitution for ρ, the expression becomes:

$$\frac{\dot{V}}{V} = \frac{\dot{m}}{m} - \frac{\dot{T}(\frac{\partial \rho}{\partial T}) + \dot{p}(\frac{\partial \rho}{\partial p})}{\rho} \tag{4.56}$$

Therefore, for the unburned zone:

$$\frac{\dot{V}_u}{V_u} = \frac{\dot{m}_u}{m_u} - \frac{\dot{T}_u(\frac{\partial \rho}{\partial T})_u + \dot{p}(\frac{\partial \rho}{\partial p})_u}{\rho_u} \tag{4.57}$$

and likewise Eqn. 4.56 also applies to the burned zone:

$$\frac{\dot{V}_b}{V_b} = \frac{\dot{m}_b}{m_b} - \frac{\dot{T}_b(\frac{\partial \rho}{\partial T})_b + \dot{p}(\frac{\partial \rho}{\partial p})_b}{\rho_b} \qquad (4.58)$$

Equating the Eqns. 4.53 and 4.58 to eliminate the V_b terms and solving for the rate of change of unburned volume:

$$\frac{\dot{V}_u}{V_u} = \frac{V_b}{V_u}[\frac{(\frac{\partial \rho}{\partial T})_b \dot{T}_b + (\frac{\partial \rho}{\partial p})_b \dot{p}}{\rho_b} - \frac{m_b}{m_b} + \frac{\dot{V}}{V_b}] \qquad (4.59)$$

An expression for the rate of change of pressure still needs to be found. Therefore equating the two expressions for V˙u/Vu (Eqns. 4.57 and 4.59) , one obtains:

$$\frac{\dot{m}_u}{m_u} - \frac{\dot{T}_u(\frac{\partial \rho}{\partial T})_u + \dot{p}(\frac{\partial \rho}{\partial p})_u}{\rho_u} = \frac{V_b}{V_u}[\frac{(\frac{\partial \rho}{\partial T})_b \dot{T}_b + (\frac{\partial \rho}{\partial p})_b \dot{p}}{\rho_b} - \frac{m_b}{m_b} + \frac{\dot{V}}{V_b}] \qquad (4.60)$$

Next, the expressions for the rate of change of temperature for the burned and unburned zones (Eqns. 4.50 and 4.51), may be substituted into the above equation. Additionally, the mass flow rate terms are functions of the rate of change of pressure. Hence,

$$\sum \dot{m}_{j_u} = \dot{m}_{crv_u} - \dot{m}_{comb} = m_{crv_u} \frac{\dot{p}}{p} - \dot{m}_{comb} \qquad (4.61)$$

and defining dummy variables similar to those defined in Eqn 4.22,

$$\sum \dot{m}_{j_u} = d_u^* - c_u^* \dot{p} \qquad (4.62)$$

Note that m_{comb} is the mass flow rate of burned gas due to combustion, as defined by the Wiebe function (Chapter 2). Likewise for the burned zone:

$$\sum \dot{m}_{jb} = \dot{m}_{crvb} + \dot{m}_{comb} = m_{crvb} \frac{\dot{p}}{p} + \dot{m}_{comb} \qquad (4.63)$$

$$\sum \dot{m}_{jb} = d_b^* - c_b^* \dot{p} \qquad (4.64)$$

Note the sign change on the mass flow rate due to combustion term. This results because as more charge burns, mass flow is being removed form the unburned zone and added to the burned zone. The enthalpy flux terms also depend on pressure:

$$\sum \dot{m}_{ju} h_{ju} = \frac{\dot{p}}{p} m_{crv_u} [h_{u_{cyl}} (crvflag) + h_{u_{crv}} (1 - crvflag)] - \dot{m}_{comb} h_{u_{cyl}} \qquad (4.65)$$

$$\sum \dot{m}_{ju} h_{ju} = e_u^* - f_u^* \dot{p} \qquad (4.66)$$

$$\sum \dot{m}_{jb} h_{jb} = \frac{\dot{p}}{p} m_{crv_b} [h_{b_{cyl}} (crvflag) + h_{b_{crv}} (1 - crvflag)] + \dot{m}_{comb} h_{b_{cyl}} \qquad (4.67)$$

$$\sum \dot{m}_{jb} h_{jb} = e_b^* - f_b^* \dot{p} \qquad (4.68)$$

Substituting these expressions for the mass and enthalpy fluxes and solving for the rate of change of pressure:

$$\dot{p} = \frac{\frac{d_u^*}{m_u} + \frac{(\frac{\partial \rho}{\partial T})_u}{(\rho m c_p)_u}\left(d_u^* h_u - e_u^* + \dot{Q}_u\right) - \frac{\dot{V}}{V_u} + \frac{d_b^*}{m_b}\frac{V_b}{V_u} + \frac{V_b}{V_u}\frac{(\frac{\partial \rho}{\partial T})_b}{(\rho m c_p)_b}\left(d_b^* h_b - e_b^* + \dot{Q}_b\right)}{\frac{c_u^*}{m_u} + \frac{(\frac{\partial \rho}{\partial T})_u}{(\rho m c_p)_u}\left(c_u^* h_u - f_u^* + V_u\right) + \frac{(\frac{\partial \rho}{\partial p})_u}{\rho_u} + \frac{V_b}{V_u}\left(\frac{(\frac{\partial \rho}{\partial p})_b}{\rho_b} + \frac{c_b^*}{m_b} + \frac{(\frac{\partial \rho}{\partial T})_b}{(\rho m c_p)_b}\left(c_b^* h_b - f_b^* + V_b\right)\right)} \qquad (4.69)$$

The definitions of the burned and unburned crevice mass flow rates are critical to the above analysis. The background explanation is presented formally in Sections 4.3 and 4.4, but for the purposes of this section it is sufficient to reiterate that when the crevice mass flow is entering the crevices (i.e. when crvflag =1) , the composition of the flow is

determined by the chamber composition. When the crevice mass flow stream is leaving the crevices (i.e. when crvflag = 0) the flow composition is determined by crevice composition. Hence, when programmed, the following expressions were used:

$$\dot{m}_{crv_u} = \dot{m}_{crv} x_{uflow}(crvflag) + \dot{m}_{crv} x_{crv_u}(1 - crvflag) \qquad (4.70)$$

$$\dot{m}_{crv_b} = \dot{m}_{crv} x_{bflow}(crvflag) + \dot{m}_{crv} x_{crv_b}(1 - crvflag) \qquad (4.71)$$

These terms were not explicitly written in the equations of this section in order to preserve clarity.

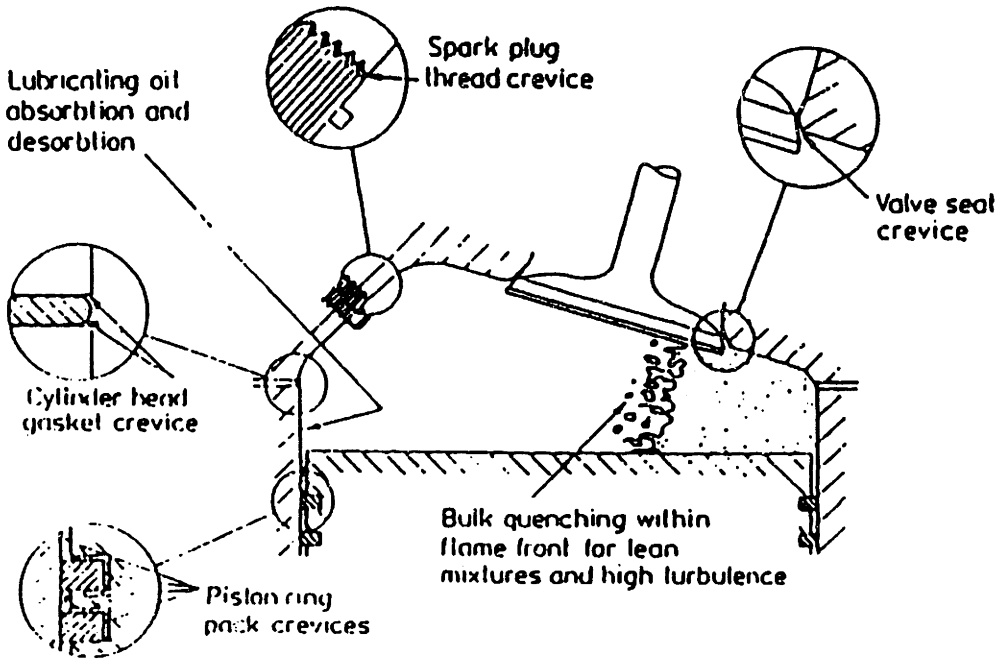

Figure 4.1: Crevice locations [7]

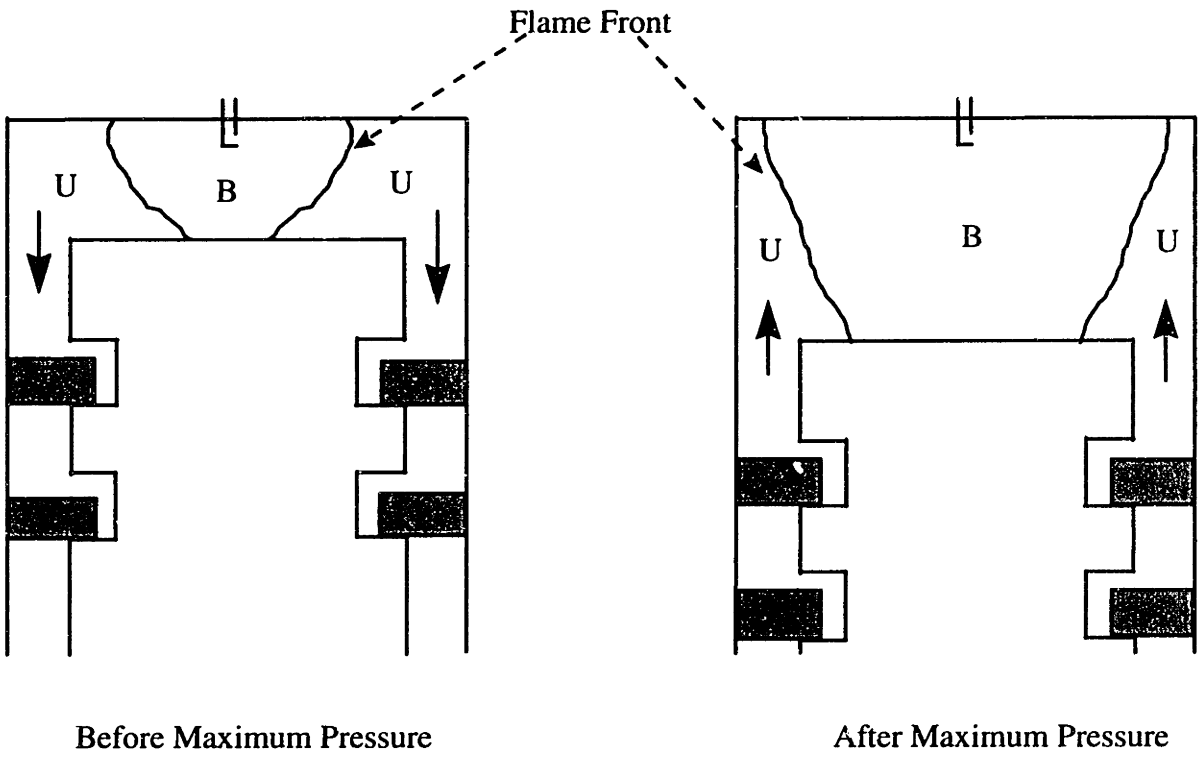

Figure 4.2: Center Spark Plug Location

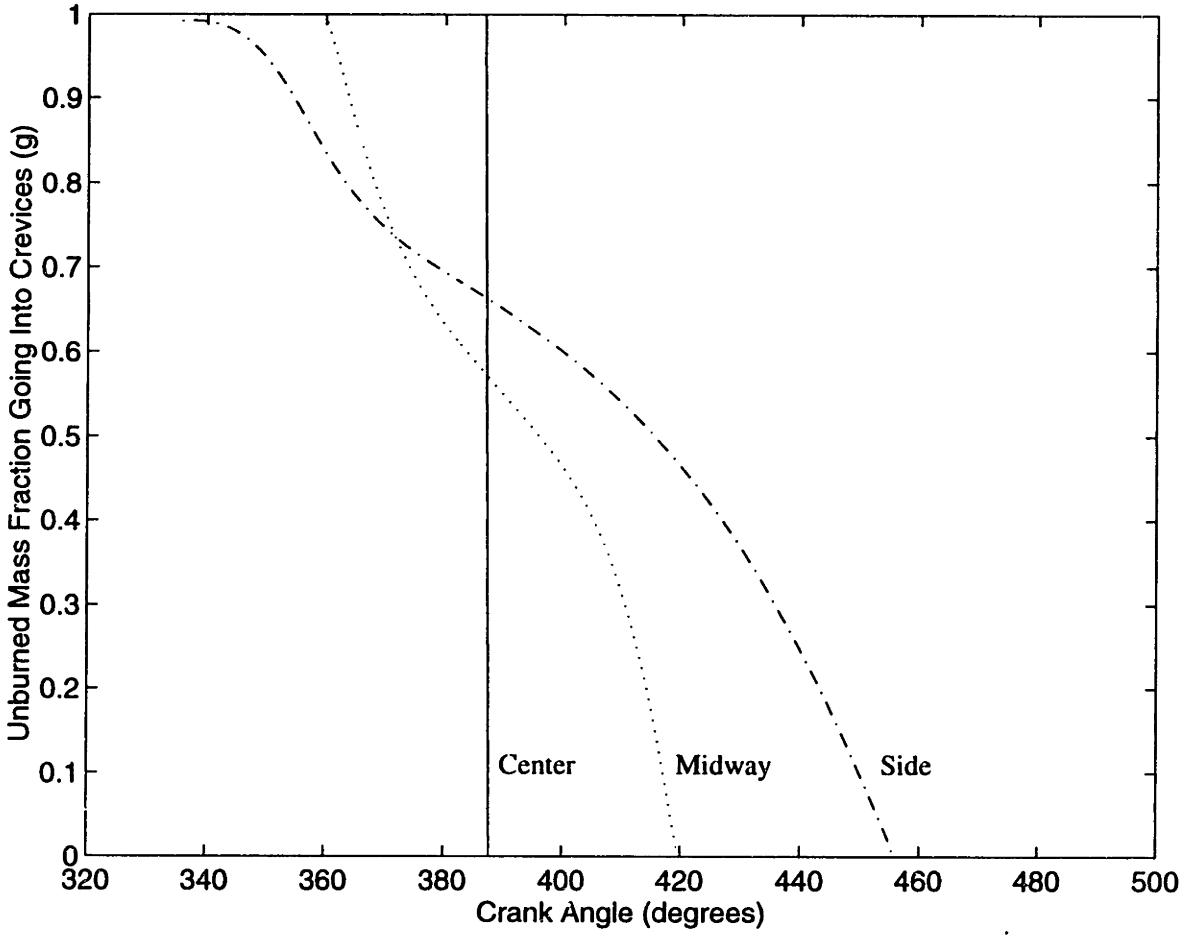

Figure 4.3: Variation of Burned Mass Fraction Entering Crevices with Various Spark Plug Locations

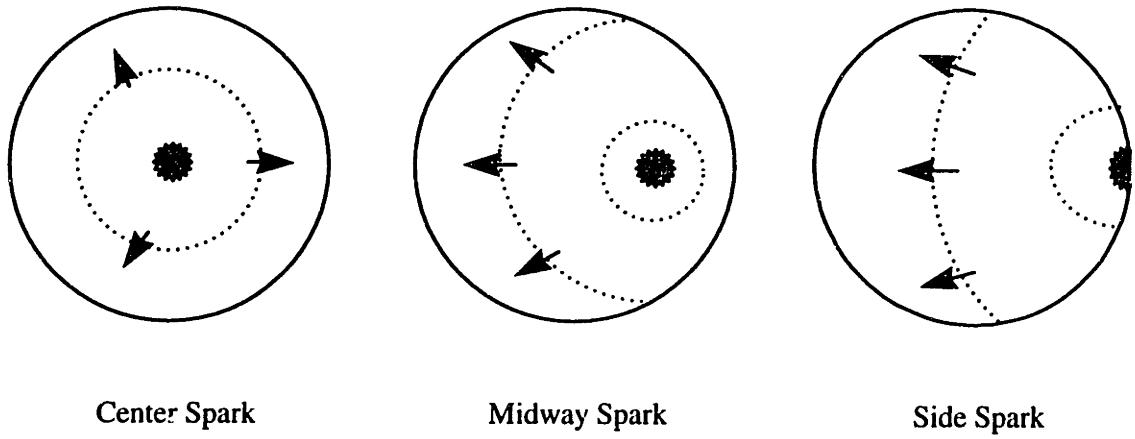

Figure 4.4: Illustration of Three Spark Plug Locations

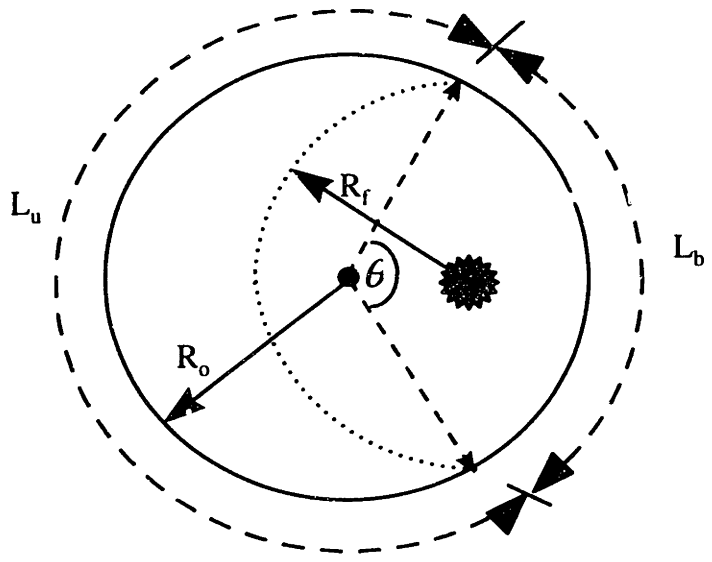

R_o = Bore / 2

R_f = Flame front position

Figure 4.5: Determination of Crevice Gas Flow Composition

5. Results

5.1 Cycle Simulation Validation

Ford Motor Company provided the data which was used to examine the impact of the modeling strategies behind NO_x emissions predictions. Data points over a range of equivalence ratios and EGR values were supplied from tests performed with a 1.6L Nissan engine. Geometric features of this engine, such as bore size and displacement volume, were matched. The fuel used was indolene; the cycle simulation was likewise performed with this fuel type. All valve opening and closing events, as well as spark timing, were matched. A complete list of these parameters is given in Table 5.1. Particular care was taken to match the burn profile of each data point as closely as possible. Accordingly, Wiebe function constants (explained in Section 2.3) were calculated for every point. Results of this procedure are displayed in Figure 5.1. For each test point, the inlet manifold pressure in the cycle simulation was varied until the IMEP value of the engine data and the cycle simulation matched. This was necessary to ensure that key engine operation parameters, such as the location of peak cylinder pressure, were in reasonable agreement.

Table 5.1: Engine Geometry and Operation Input Parameters for the Engine Cycle Simulation

Bore	7.8 cm
Clearance Volume at TDC	44.3857 cm^3
Cylinder Rod Length	
RPM	
Fuel Type	Indolene
Equivalence Ratio ϕ	
EGR	
EGR Temperature	
Fresh Charge Temperature	325 K
Piston Temperature	403 K
Head Temperature	373 K
Cylinder Wall Temperature	363 K
IVO	-15 °CA
IVC	233 °CA
EVO	481 °CA
EVC	729 °CA
Spark Timing	
Combustion Duration	
Inlet Manifold Pressure	
Exhaust Manifold Pressure	1.00 atm

N.B. Blank entries in Table 5.1 indicate that these entries varied from one run of the simulation to another. The entries that are filled in indicate that these values remained fixed throughout this research.

One objective of this thesis was to examine NOx formation over a range of equivalence ratios. The maximum equivalence ratio data point available from Ford was $\phi = 1$ (i.e. at stoichiometric operation). Rich operation data ($\phi > 1$) from a number of published sources was used in order to obtain a legitimate NOx value at $\phi = 1.15$ for comparison with the cycle simulation result. From references [18, 19, 33], the following data was obtained:

Group #1 (Hulls and Nickol [18]):

A/F	NOx [ppm]
14.6	1900
12.7	1000

Group #2 (Hulls and Nickol [18]):

A/F	NOx [ppm]
14.6	4000
12.7	1500

Group #3 (Komiyama [19]):

ϕ	NOx [ppm]
1.0	4000
1.15	1300

Group #4 (Quader [33]):

A/F	NO [g/hour]
15.1	40
13.5	12

For each set, the ratio of NOx formation from lean operation to rich operation was determined – 0.53, 0.38, 0.33, 0.3 for Group #1 through #4 correspondingly. The average of these values was calculated to be 0.39. Using the NOx data point at $\phi = 1$ from Ford and the average ratio of 0.39, an approximate NOx value at $\phi = 1.15$ was found to be 4.3 g/kW-hr. The burn profile (and hence Wiebe constants) for $\phi = 1$ was assumed to be valid for $\phi = 1.15$. Reasonable spark timing and IMEP values for $\phi = 1.15$ were estimated by extrapolating from the existing Ford data set.

5.1.1 Issues Concerning the Cycle Simulation Validation

There are several issues associated with the engine data, the cycle simulation, and the validation procedure which should be considered when determining expectations of, and limitations on, levels of accuracy for ISNO calculations.

1) The engine data set used did not include points in the fuel-rich region. The procedure described in Section 5.1 does provide a rich data point suitable for validation; however, it does not have the "stand-alone" precision expected of a data point which was experimentally obtained along with the rest of the supplied set.
2) Two data sets were provided: an A/F ratio sweep with EGR held constant at 0%, and an EGR sweep with constant A/F ratio at 14.6. Though the same engine was used to obtain these sets, the 14.6 A/F, 0% EGR point had different results – including ISNO – in both sets (10.95 for the A/F sweep and 9.11 for the EGR sweep).
3) Each data set included both tumble and swirl data (i.e.: the cylinder charge was forced to undergo either a tumbling or a swirling motion in the chamber, for more information see [16]). The tumble data points were used since it was decided that this motion was closer to the modeled physics of the cylinder charge in the cycle simulation. However, it is worthwhile to note that the tumble points typically had higher NOx values than those for swirl (Figures 5.3 and 5.4). At ϕ=0.65, the percent difference between the tumble and swirl values was 52%; at EGR=15%, the percent difference was 23% and at EGR=22%, the percent difference was 21%.
4) The cycle simulation has a significant number of input parameters available, in order that a particular run of the cycle simulation may be customized to match the geometric features of the engine of interest (see Table 5.1). The simulation has the

functionality to use a "geometric data file" which allows for advanced correspondence to the engine design. The simulation uses this file to get a detailed representation of the engine features, including: the shape of the piston head, combustion chamber volume, and the spark plug location. Accordingly, geometry-dependent calculations such as burn profile, burned zone volume, and boundary layer location may be performed with greater accuracy. This geometry data file was not generated for the 1.6L Nissan engine used in data collection for this project; a standardized file which has been used previously in other MIT research efforts was supplied to the cycle simulation instead. The impact of the lack of a tailored geometry file on calculations was considered to be insignificant for this thesis; however, since subsequent work which is to build upon this research requires a detailed representation of the engine in order to make sophisticated design decisions, use of a specialized geometry file would then be needed.

5) Inclusion of a geometry data file specific to the 1.6L Nissan engine would have made the assessment of spark plug location effects on NOx easier to perform (see Section 4.3) since only a change of the plug's coordinates within the data file would have been required. Additionally, the spark plug location examination could have been performed in three-dimensional terms with the geometry file, rather than the two-dimensions used in the procedure developed in Section 4.3.

Several assumptions were made in the physical models, their effects are discussed in Section 5.6.

The purpose of this chapter is to assess and analyze the NO predictions obtained with the MIT SI Engine Cycle Simulation. Results are discussed in two stages. In the first

stage, the sensitivity of these predictions to the inclusion of three major physically-based models (adiabatic core and boundary layer models, layered burn model, and the crevice gas model) is presented. For each model in turn, results obtained are compared to the simpler "base case" (Section 2.5) result. This procedure allows for the examination of the impact and validity of each model. The second stage of the discussion compares the computational results to the experimentally obtained engine data, for both the individual models and the entire set, grouped as the "complete physical model." This comparison to real data allows the cycle simulation to be analyzed as a design tool on a first-order level. In addition, this part offers further insight into the validity of the models and highlights areas where subsequent modeling efforts should be focused.

5.2 NO Predictions with Adiabatic Core and Boundary Layer Models

This section treats the NO predictions obtained from the MIT Cycle Simulation employing the three-zone combustion model. In this modeling procedure, which is discussed fully in Section 3.1, the cylinder contents during combustion are partitioned into three zones: unburned, adiabatic core, and thermal boundary layer. Together, the adiabatic core and thermal boundary layer together contain all burned charge present in the chamber. Of particular importance to NO predictions is that each zone is characterized by a unique temperature. The contents of the adiabatic core are at hot combustion temperatures; due to the cooler gas temperature near the cylinder wall, heat transfer rates from the cylinder are reduced which results in higher adiabatic core

temperatures [16]. The contents of the thermal boundary layer contents are at much lower temperatures than those of the adiabatic core, since the thermal boundary layer accounts for the gas cooled by the combustion chamber walls.

The effects of this temperature stratification are reflected in the NO predictions over both the equivalence ratio and EGR sweeps (Figures 5.5, 5.6). NO produced in the adiabatic core is formed according to a temperature-dependent equation (Equation 3.4), which indicates that the higher the temperature, the more NO that is produced. The NO concentration in the boundary layer develops strictly as a result of mass transfer from the adiabatic core. The NO levels in the boundary layer are frozen at the levels they are at at the time of transfer. Because of the low temperatures of the boundary layer region, these concentrations are much higher than would be expected if the NO reactions had been able to proceed to equilibrium.

With the simpler two-zone combustion model, where the cylinder contents are separated only into burned and unburned zones, NO production is governed by the temperature-dependent equations of Section 2.4. Note that the burned zone is characterized by a single mean temperature. In contrast, with the adiabatic core and boundary layer models, two unique temperatures are needed to characterize the burned zone. Corresponding to this temperature stratification, NO predictions with the three-zone combustion modeling increased over those from the less physically realistic two-zone model across the entire equivalence ratio and EGR sweeps. This is shown in terms of magnitude through ISNO (indicated specific NO) in Figures 5.23 and 5.29 for the equivalence ratio and EGR sweeps, respectively. The change in ISNO from the two-zone to the three-zone combustion model from $0.62<\phi<1.15$ varies between 0.3 to 3.3 g/kW-

hr. The change in ISNO from 0%<EGR<30% varies between 2 g/kW-hr @ EGR = 0% and 0.0 @ EGR = 30%. These predictions are also illustrated on a relative basis, using the ratio of NO predicted with the enhanced model and the NO predicted with the base model. This is shown for the equivalence ratio sweep in Figure 5.24 and for the EGR sweep in Figure 5.30. The ISNO ratio varies between 1.5 and 1.2 for $0.63<\phi<1.15$, with the results being lowest at $\phi=0.9$ and $\phi=1.0$. Away from these operating points, less NO is produced and the percentage change of NO predictions associated with the improved modeling increases. The same holds true for EGR, in which the ratio varies from 1.0 to 1.5.

Several factors explain the sweep-wide increase in NO when the more advanced physical model is included. Larger concentrations of NO are produced in the adiabatic core due to its higher temperature (as opposed to the mean temperature of the two-zone model). The mass in the lower-temperature boundary layer is frozen at concentrations much higher than those which would have been reached had the reactions been allowed to proceed to equilibrium. The results follow expected trends. For the lean and dilute regions of operation, where lower temperatures are attained in the engine cylinder overall, less NO is predicted. For the rich region, less NO is predicted than at the stoichiometric operating point since less air is available to combust with the fuel causing lower combustion temperatures to be reached.

5.3 NO Predictions with Layered Model

As was discussed in Section 3.2, the adiabatic core may be modeled in an "unmixed" or "layered" fashion, in order to more appropriately model burned zone development. As the flame propagates through the chamber, the mass which was burned during a particular timestep forms a "layer" or "slice". There is no heat transfer between subsequently formed layers. One result of this model, critical to NO predictions, is that an early formed layer will be subsequently compressed by the expansion of the gases of the combusting slice. Hence, the mass in this layer reaches a temperature higher than it normally would have then by combustion alone. The "first-to-burn" slice reaches higher temperatures and attains higher concentrations of NO than later burning slices (Figure 5.7).

The layered burn model is applicable only to gases away from the combustion chamber walls since heat transfer interactions with the walls would interfere with its adiabatic requirements. Therefore, to employ the layered burn model, a thermal boundary layer must also be used to ensure that the unmixed model approach is physically justifiable. Accordingly, this layered modeling may apply only to the adiabatic core region. As a result, for the completeness of this analysis, NO predictions with the layered model are compared to two cases – results generated with the base model and with the three-zone model approach. By comparing results with the three-zone model having a layered adiabatic core to results with the unlayered three-zone model, effects of the layered burn model may more clearly be seen. However, it is also important to compare layered burn predictions to those from the base model for consistency with the rest of the chapter.

Figure 5.25 shows NO predictions for the equivalence ratio sweep in terms of ISNO. For $\phi < 0.8$, inclusion of the layered model increases NO predictions; for $\phi > 0.8$, they are decreased. This trend was also observed by Raine, et al. [34]. For the ratio of ISNO predicted with the enhanced model to NO predicted with the base model between $0.62<\phi<1.15$, the result varies between 3.2 and 1.0 (Figure 5.26). This NO ratio is a minimum at $\phi=1.0$. Likewise, for the ratio of ISNO predicted with the enhanced model to NO predicted with the unlayered three-zone model between $0.62<\phi<1.15$, the result varies between 2.11 and 0.8.

For the EGR sweep, EGR values of 0, 10, 20, 25, and 30% were tested. For EGR of 0% and 10%, inclusion of the layered model causes a prediction of less ISNO than the adiabatic core/boundary layer model alone, with differences of 2.6 and 0.4 g/kW-hr, respectively (Figure 5.31). In contrast, for EGR = 20, 25, and 30%, the enhanced model predicts more than the adiabatic core/boundary layer model alone, with maximum differences of 0.2, 0.2, and 0.1 g/kW-hr, respectively. The ratio of NO predictions with the enhanced model to that of the base model varies between 0.9 and 2.5 for the EGR sweep (Figure 5.32). The minimum ratio result of 0.9 is at @ EGR = 0% and the maximum of 2.5 is found @ EGR = 25%. As far as the comparison between the enhanced model (layered three-zone model) and the unlayered three-zone model (burned zone separation into the adiabatic core and boundary layer with no layering) is concerned, the ratio increases from 0.7 @ EGR = 0% to 2.0 @ EGR=30%.

Results with the layered burn model vary between comparisons with the base case and the three-zone model for several reasons. First, recall that the compression of the slices

causes an additional temperature increase above that generated by combustion alone. As before, NO production increases with increasing temperature. Hence, with the layered burn model, a "NO stratification" is established in the burned zone that is very different from the uniform NO distribution of the base case. Second, The NO concentration distribution (and the overall NO concentration) is related to the shape of the burn profile. Recall that one layer is formed per timestep. Depending upon the shape of the burn profile modeled by the Wiebe function (Section 2.3), the amounts of mass in early and late slices may vary widely between each other. For example, an initially fast burning process could have larger amounts of mass in its early-to-burn slices than in its late-to-burn slices. This means that greater amounts of high temperature burned mass are able to experience the additional compression and corresponding raise in temperature – translating to high NO concentrations in those early-to-burn slices. If the burn profile depicted an initially slow burning process, early slices would contain less burned mass (with lower NO concentrations) than their counterparts in the initially fast burning process. Thirdly, it is important to realize that the boundary layer grows through its receipt of mass from the adiabatic core. A slice which burns early could feasibly donate more mass to the boundary layer than a late burning slice, depending upon burn rate. This means two things: i) the early burning slices, which are at the highest temperatures (and are therefore generating the most NO of all the layers) could potentially get "eaten" by the growing boundary layer. Hence, our high NO generators could cease to exist (the first few layers have been around longer so they get eaten by the growing boundary layer); ii) as stated, the mass going into the boundary layer from the adiabatic core becomes frozen in concentration. Therefore, not only is the mass in the boundary layer frozen at

NO levels higher than would be the case if it was allowed to go to equilibrium, but this mass is coming from the compressed layers that have augmented NO levels due to the temperature augmentation from compression. Final NO predictions result from the interplay between these items.

5.4 NO Predictions with Crevice Gas Model

The crevice gas model is intended to account for effects caused by fuel-air mixture pushed into narrow regions adjacent to the combustion chamber during compression. The flame is quenched at the entrance of these regions, so the mixture is "hidden" during its tenure in the crevices and does not participate in the combustion process as it normally would have done if the crevices had not been present (see Section 4.1). However, the existence of the crevices does not mean that this "hidden" gas will completely escape combustion. Rather, this gas could participate in combustion later than it normally would have. In addition, it is important to remember that crevice gas composition is dependent upon several factors, including burn profile and spark plug location (Section 4.3). Hidden unburned mixture is what has significant impact on combustion (and therefore NOx generation). Since less combustible mixture is present in the chamber before expansion then there would be without crevices, peak pressures and temperatures in the chamber are decreased. As has been discussed in previous sections, lower temperatures translate into lower NO concentrations.

It is meaningful to reiterate the major modeling assumptions made for the crevice gas model. Crevice gas pressure is taken to be equal to the cylinder pressure. The crevice

volume is constant throughout the cycle, at 2% of the displacement volume. For the 1.6L Nissan engine studied, this translates to a crevice volume of 0.89 cm^3. The crevice gas temperature was also assumed to remain constant (see Equation 4.1), which had a value of 383 K.

One simplification made in the development of the crevice model for computational simplicity should be noted. A careful accounting was made of mass flowing into and out of the crevices throughout the cycle, and the unburned and burned mass portions associated with that mass flow. However, the NO fraction associated with that mass flow was not determined. The ideal case would have been that for the mass flowing into the crevice at a particular time step, the corresponding NO in that mass "packet" to have been known. This value would then be tabulated with the rest of the NO in the crevices. When mass started to return to the cylinder as the cylinder pressure decreased, those mass packets would return to the cylinder with the NO fraction associated with it from the crevices. This NO would then be tabulated appropriately with the rest of that associated with the cylinder charge. Currently, there is no NO associated with the crevice flows. This could either inflate or deflate the in-cylinder NO concentration, depending upon which part of the cycle is being examined. As an example, more NO could have entered the crevice in a particular packet than could have exited (the levels of NO in the cylinder at the time of exit of that packet were lower).

For both the Equivalence ratio and EGR sweeps, inclusion of the crevice gas model caused an increase in NO predictions. For the equivalence ratio sweep (Figures 5.27 and 5.28), the maximum change between the crevice model prediction and the base model prediction was 5.1 g/kW-hr at ϕ=0.92 and the minimum difference was 0.3 g/kW-hr at

ϕ=0.6. For the EGR sweep (Figures 5.33 and 5.34), the maximum difference was 3.3 g/kW-hr at an EGR of 0% and the minimum difference was 0 g/kW-hr at an EGR of 30%. When calculating the ratio of NO predicted using the crevice model and using the base model, the maximum was found to be 1.6 at ϕ=0.73 and ϕ=1.15. The minimum ratio value was 1.3 at ϕ = 1.0. For the EGR sweep, the maximum ratio was 2.0 at an EGR of 25% and 1.0 at an EGR of 30%.

It was stated earlier that, due to the presence of crevices, cylinder temperatures (and therefore NOx production) would decrease. As Figures 5.28 and 5.34 show, this is clearly not the case; inclusion of the crevice model increases NO predictions between 30-60% for the equivalence ratio sweep and 35-100% for the EGR sweep. Taking the method of the cycle simulation operation in account, this trend is not unexplainable – and it reveals some important information. Since IMEP was the variable which was matched throughout each of the model additions (thermal boundary layer and adiabatic core, layered burn) to a specified base value of IMEP, the inclusion of the crevice model required an increase in inlet manifold pressure in order to attain the required IMEP value. Good agreement with location of peak pressure follows with this fact. The end result was that in order to match cylinder conditions for the base case, the crevice model runs had to have a higher inlet manifold pressure and therefore more mass inducted into the cylinder. This is also reflected in the residual fraction calculations. It has been demonstrated that residual gas fraction decreases because of increases in inlet pressure [23, 16]. This behavior is likewise seen with the MIT cycle simulation, as presented in Figures 5.35-5.38. Indeed, as the crevice volume is increased, requiring higher and higher inlet manifold pressures to reach the IMEP of the base case, residual fraction decreases.

Residual fraction essentially acts as an "internal" EGR [4], diluting the fresh fuel/air mixture with the burned gases remaining in the cylinder. EGR reduces NO (see Section 1.3). Hence, the more residual, the less NO. This trend is reflected in the results – the largest crevice volume (4% of the clearance volume) has a smaller residual than the 1% crevice volume by approximately 26%, and likewise has a higher NOx prediction than the 1% by approximately 60%.

5.5 Impact of Key Assumptions

Several assumptions were required to reasonably attach the modeling requirements of this research. Four such assumptions are examined in this section: crevice gas temperature, crevice size, gas property determination, and EGR temperatures. While details surrounding these issues were not the only assumptions made to arrive at the physical models, an examination of the relative importance these assumptions had on the models still serves a twofold purpose: to benchmark the performance of the models and to bring insight as to where future modeling efforts should be placed.

5.5.1 Impact of Crevice Gas Temperature

The temperature of the gas in the crevices is calculated as the mean of the piston and cylinder wall temperatures. This is illustrated in Equation 4.1, repeated here for clarity:

$$T_{crv} = \frac{T_{piston} + T_{wall}}{2}$$

For this research, the cycle simulation was used with T_{piston} as 403 K and T_{wall} as 363 K, making the crevice gas temperature, T_{crv}, to be constant at 383 K throughout a run of the

cycle simulation. The values used were educated guesses – data for these temperatures corresponding to the Ford data set was not available. To determine if model sensitivity to the crevice gas temperature merited more accuracy, comparison runs using data from the literature was used [1], with T_{crv} being set to 430 K, and T_{piston} and T_{wall} remaining as they were at 403 K and 363 K, respectively.. The effect of crevice gas temperature on NO production could then be examined; the entire equivalence ratio sweep was investigated. Results are plotted in Figures 5.17 and 5.18. Figure 5.17 demonstrates that NO predictions with the higher crevice temperature were lower, with the largest ISNO difference being 0.8 g/kW-hr at an equivalence ratio of 0.81. The decrease associated with the higher crevice gas temperature is expected – higher temperatures mean that the gas has expanded and is less dense, causing less gas to be "hidden" in the crevices during the combustion processes. The effective size of the crevices is essentially smaller. The increase in crevice gas temperature from 383 K to 430 K (a difference of 47 K) created a percentage change ranging from 0 to 6% in ISNO (Figure 5.18).

5.5.2 Impact of Crevice Size

The size of the crevices, discussed in terms of a parameter called crevice volume, is assumed to remain constant in the calculation set. In reality, the crevice volume will decrease or increase corresponding to thermal expansion of the piston and cylinder liner depending on their temperature. While these change with load and speed, minimal changes in size associated with this phenomenon make the constant crevice volume assumption reasonable. However, since the selection of crevice volume at 2% of the cylinder clearance volume was an arbitrary one, the effects of doubling and halving the

from the "base case" value of 2% was examined. A crevice volume of 4% of the clearance volume is excessive – values of 1-2% have been reported in the literature [7] – but it was of interest to see the impact of a complete range of crevice sizes. Calculations were performed for the entire equivalence ratio sweep; results are shown in Figures 5.19 and 5.20. With respect to the 2% base volume, doubling caused an increase in ISNO production ranging from 1.7x to 1.2x (corresponding change in ISNO of 4.03 and 5.7 g/kW-hr). The reduction to a 1% volume caused a reduction in ISNO ranging from 0.78x to 0.88x, which translates into a change of ISNO of 0.2 g/kW-hr and 1.6 g/kW-hr, respectively. As subsequent research requires more detailed models, as accurate an estimate of crevice size as possible is merited.

5.5.3 Impact of Property Calculation Methods

As is discussed more completely in Chapter 2, thermodynamic properties of burned gases and unburned gases in the engine cylinder are calculated using different procedures. However, while both burned and unburned gases are present in the crevices simultaneously, separate burned and unburned zones are not developed in the crevices as they are in the engine cylinder. Consequently, the property routines for unburned gases are used to calculate the thermodynamic properties of crevice gas. It should be noted that a careful accounting of burned and unburned gas in the crevices is still maintained; only for the thermodynamic property calculations is the crevice gas assumed to be completely unburned. To test the sensitivity of ISNO predictions to this assumption, the cycle simulation was run at an equivalence ratio of 1.0 with 0% EGR, for each of the spark plug positions (center, midway, and side). No change in ISNO was found when using the

unburned property calculation procedure (i.e., assuming the crevice gas to be unburned for property calculation purposes, as was done throughout this research) or when using the burned property routines (i.e., assuming the crevice gas to be completely burned for thermodynamic property calculation purposes). Hence, ISNO predictions are not sensitive to the property methodology for the crevices, and division of the crevices into burned and unburned zones would not have had any significant impact on this research.

5.5.4 Impact of EGR Temperature

The data sets supplied by Ford include EGR temperatures for the complete EGR sweep. These temperatures are shown in Figure 5.22. The cycle simulation runs were performed using the supplied EGR values. However, it was decided to investigate the effect of EGR temperature on ISNO predictions. Accordingly, two other sweeps of EGR were performed – one using an EGR temperature of 360 K throughout the entire sweep, and the other using 300.15 K throughout the entire sweep. The 360 K value was chosen since it represents the upper range of reasonable EGR values; 300.15 was chosen since it represents the lowest reasonable value. Results are shown in Figure 5.21. To more completely assess the impact of EGR temperature, sweeps were performed using the base model, and then with the full physical model (boundary layer, layered adiabatic core, and crevices) discussed in this thesis. In both cases, the N_2O mechanism was included for the calculations. The base model showed slightly greater sensitivity in ISNO calculations to EGR temperature, with the greatest sensitivity for both being at an EGR of 25%. The unexplainable deviation at the 25% EGR mark is by far the largest at 1.5; ISNO sensitivity at the four other EGR levels varied from 1 to 1.16. Hence any inaccuracies in

the EGR data values used in the cycle simulation to get NO predictions would not have any severe detrimental impact on the results.

5.6 NO Predictions with the Complete Physical Model

This section examines the impact on NO prediction by the inclusion of the complete physical model. The term "complete physical model" includes the treatment of the burned zone divided into an adiabatic core and a thermal boundary layer, the layered burn treatment of the adiabatic core, and the crevice gas model. From a kinetic standpoint, NO formation is assumed to be governed by the extended thermal Zeldovich mechanism augmented by the N_2O mechanism. Reaction rates for these mechanisms are as presented in Section 2.4.

Importantly, this section also begins a comparison of the computational results to engine data provided by Ford Motor Company (Section 5.1). This serves to help benchmark where the computational results lie against experimental data. This also serves to help guide the development of the Cycle Simulation as a design tool, providing guidance as to where further modeling development efforts should be expended and how to best use results as they stand now.

5.6.1 Kinetics Revisited

Two major kinetics issues were explored in Chapter 2: which mechanisms were to be used to describe NO formation in the engine cylinder, and what reaction rates were to be used in conjunction with the reactions of these mechanisms. Though these topics were thoroughly explored in Chapter 2, a similar examination was performed using the

complete physical model in the Cycle Simulation (rather than just that of the base case) for completeness. This procedure was not intended to serve as a replacement for the work of Chapter 2 -- it is not as extensive. Rather, the goal was to document that the results of the examinations of Chapter 2 are still valid when the full physical model is included.

The results generated with the complete physical model and the baseline model were extremely similar. The sensitivity of NO predictions to the inclusion of the N_2O mechanism with the extended thermal Zeldovich mechanism varied between 1.01 and 1.2 times larger than predictions without the N_2O mechanism for the equivalence ratio sweep – exactly the same range as when the base case was used (Figures 5.8 and 5.9). Likewise for the EGR sweep, this ratio varied between 1.0 and 1.02 with the complete physical model – for the base case model the ratio of NO predictions with N2O and without N2O was between 1.0 and 1.03 (Figures 5.10 and 5.11). The effect of reaction rates on NO predictions with the full physical model was also investigated for the equivalence ratio sweep (Figure 5.12). Halving the reaction rates caused NO predictions to have differences between 0.65x (lean) to 0.88x (rich) - the corresponding calculations with the base model produced a range of ~0.58-0.69. When the reaction rates were doubled, NO formation with the complete physical model caused a typical corresponding change of ~1x to ~1.5x. Likewise, the base model produced changes in NO predictions ranging from 1.2x - 1.8x. Hence, the conclusions of Chapter Two are still valid when he full physical model is used in the Cycle Simulation, rather than the simpler physics of the base case.

5.6.2 Impact of Thermal State Representation

A summary of the trends associated with the physical models discussed in Sections 5.2 to 5.4 is presented below. The terms "increase" and "decrease" with their associated percentages refer to NO predictions using a particular physical model as compared to experimentally obtained NO engine data.

Table 5.2: Assessment of the impact of enhanced physical models on NO predictions through comparison with experimentally obtained engine data

[illegible]	BASE	BL	LASER BL	CREVICE	CREVICE BL	FUEL MODEL
0.62	Decrease 78%	Increase 50%	Decrease 30%	Decrease 67%	Decrease 56%	Decrease 11%
0.73	Decrease 55%	Increase 39%	Decrease 24%	Decrease 27%	Decrease 4%	Increase 6%
0.81	Decrease 31%	Increase 34%	Decrease 13%	Increase 7%	Increase 34%	Increase 23%
0.92	Increase 0.3%	Increase 23%	Decrease 2%	Increase 36%	Increase 56%	Increase 33%
1.0	Decrease 2%	Increase 19%	Decrease 7%	Increase 27%	Increase 42%	Increase 25%
1.15	Decrease 58%	Increase 39%	Decrease 48%	Decrease 42%	Decrease 16%	Decrease 25%

EGR [%]	BASE	BL	LAYER +BL	CREVICE	CREVICE +BL	FULL MODEL
0%	Increase 6%	Increase 28%	Decrease 0.1%	Increase 43%	Increase 61%	Increase 38%
10.1%	Decrease 34%	Decrease 12%	Decrease 20%	Increase 5%	Increase 32%	Increase 15%
20%	Decrease 72%	Decrease 59%	Decrease 49%	Decrease 54%	Decrease 35%	Decrease 26%
24.8%	Decrease 86%	Decrease 79%	Decrease 66%	Decrease 72%	Decrease 66%	Decrease 52%
29.6%	Decrease 89%	Decrease 89%	Decrease 78%	Decrease 89%	Decrease 78%	Decrease 67%

An obvious question is how can one consider these physical model additions a meaningful "enhancement" since they cause the ISNO calculations to deviate further away from the data than the base case for some operating points, particularly around stoichiometric. The answer lies in the matching, or calibrating, of the other models (such as heat transfer, valve lift, etc.) present in the MIT Cycle Simulation. Of these, perhaps the model requiring the most attention would be the heat transfer model [29]. Three constants are involved in this model; a closer match of them to represent conditions for the Nissan 1.6L could reveal that the baseline model did not hit the data as well as it currently appears. Matching the heat transfer model would have much less of an effect on the lean regions and high EGR regions; since cylinder temperatures are cooler, the heat

transfer between the chamber and surroundings is less significant. Hence, the results (which show the additional modeled physics bringing the calculations closer to the data) would not be significantly impacted. For the rich region of the equivalence ratio sweep, unmodeled physics is affecting the results. Formation of NO within the flame front NO (Section 1.6), which is unaccounted for, could be a significant factor.

5.6.3 Assessment of the NO Predictions with the Complete Physical Model

Continuing the model "matching" discussion of Section 5.6.2, it is important to note that even though the complete physical model was "unmatched" (making some of the base case predictions lay closer to data points than those of the complete physical model) it still performed better than the base case model across the full sweeps. This can be shown in terms of RMS (root mean squared) error. Parameter E_N is defined as:

$$E_N = \frac{Model_N - Data_N}{Data_N}$$

and RMS error is defined as:

$$RMS\ Error = \frac{\sqrt{E_1^{\,2} + E_2^{\,2} + E_3^{\,2} + \cdots + E_N^{\,2}}}{N}$$

where N is the number of points in either the equivalence ratio sweep or the EGR sweep. For the equivalence ratio sweep, the base case had a RMS error of 19.3% while the complete physical model had a RMS error of 9.2%. For the EGR sweep, the base case had a RMS error of 24.6% while the complete physical model had a RMS error of 19.4%. The complete physical model performed significantly better (e.g. NO predictions were closer to the experimentally obtained NO data values) than the base case model over

these sweeps, particularly for equivalence ratio. When more appropriate "matching" is performed, the complete physical model is expected to perform even better.

Specifically, over the equivalence ratio sweep the NO predictions with the full enhanced model and the base case differed by a maximum increase of 6.8 g/kW-hr at ϕ=0.8 and a minimum of 1.4 at ϕ=1.15 (Figure 5.13). The ratio of NO predictions with the enhanced model and NO predictions with the base model ranged from 1.28 at ϕ=1 and 4 at ϕ=0.62 (Figure 5.14). For EGR, the maximum increase with the full physical model was 2.9 g/kW-hr at EGR=0% and a minimum of 0.2 g/kW-hr at EGR = 30% (Figure 5.15). The ratio of NO predictions with the full physical model to those with the base model ranged from 1.3 at EGR = 0% to 3.5 at EGR = 25% (Figure 5.16).

5.7 Illustration of the Cycle Simulation as a Design Tool

Though the MIT SI Engine Cycle Simulation is only in the initial phase of its development as a design tool, its utility is already able to be documented. Two examples of the Cycle Simulation used in this capacity are presented in this section. The first example demonstrates how engine manufacturers may employ the Cycle Simulation to help make a hardware design decision. The second example illustrates how optimal operating conditions may be found with Cycle Simulation for a specific engine or particular set of engine characteristics, leading to the determination of corresponding design requirements.

Spark plug location was discussed in conjunction with the crevice gas model in Section 4.3. Three spark plug positions were examined: side, midway and center (in terms of the

chamber diameter). The effect of spark plug location on NO production is a question that would clearly be of interest to an auto manufacturer. At the equivalence ratio ϕ=1 and an EGR of 0% with the 1.6 L Nissan engine characteristics, there was no difference in the ISNO prediction of the Cycle Simulation. Of course, a more sophisticated computation model and a more extensive range of points would have to be made before the designers could make a final decision about spark plug location. However, these simple tests do demonstrate that at least for this operating point spark plug location should not greatly affect NO emissions generation. At the least, it indicates to the modeler who is concerned with NO predictions that his focus may be better applied elsewhere before applying extensive effort to improving the spark plug location modeling for this operation point.

Another example is the tradeoff between leaning the air/fuel mixture or adding more EGR to dilute the cylinder mixture. Both have had some success in reducing NO emissions, but neither method is without drawbacks. For example, the more lean the mixture, the greater the fuel efficiency, since there is more air present in the cylinder to expand and help push the piston down. However, an ultra-lean mixture (or mixture diluted with EGR) is also synonymous with poor combustion quality. Such issues have been and continue to be widely discussed in the literature [16]. With respect to the Cycle Simulation, entire sweeps throughout the complete range of equivalence ratio and EGR may be easily performed, as demonstrated throughout this thesis. With such information, attainable faster and cheaper than experimental results could ever be, a designer is able to evaluate optimal operation for fixed set of parameters, or explore advantages and tradeoff

over many variables ad infinitum. Though ISNO was the focus of this research, any variable could be substituted for the discussion, such as fuel economy or hydrocarbon emissions generation.

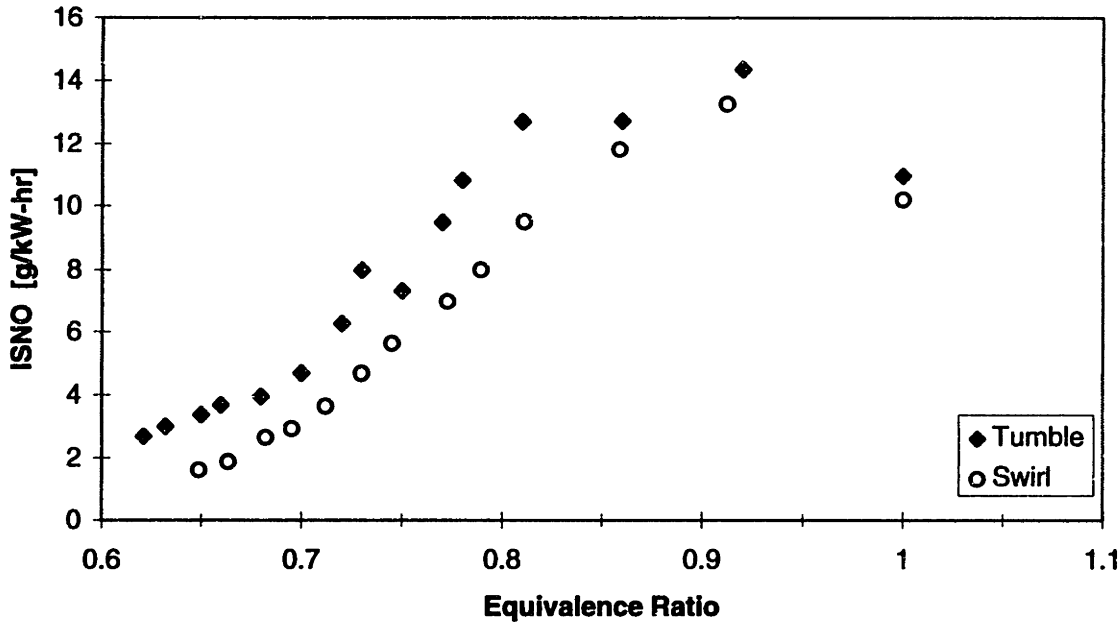

Figure 5.1: Tumble and Swirl Data for the Equivalence Ratio Sweep

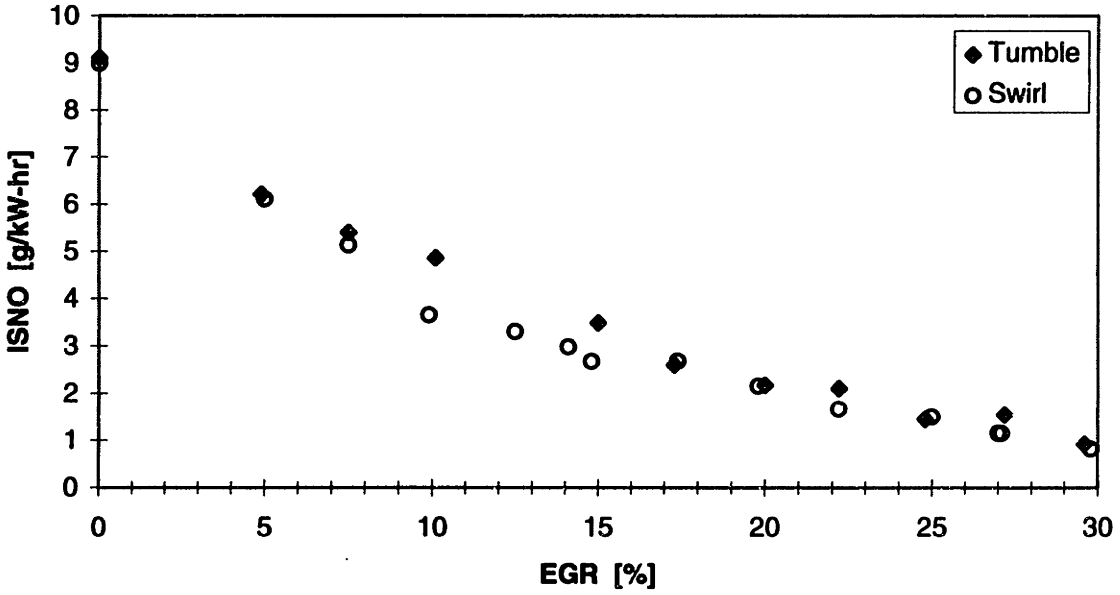

Figure 5.2: Tumble and Swirl Data for the EGR Sweep

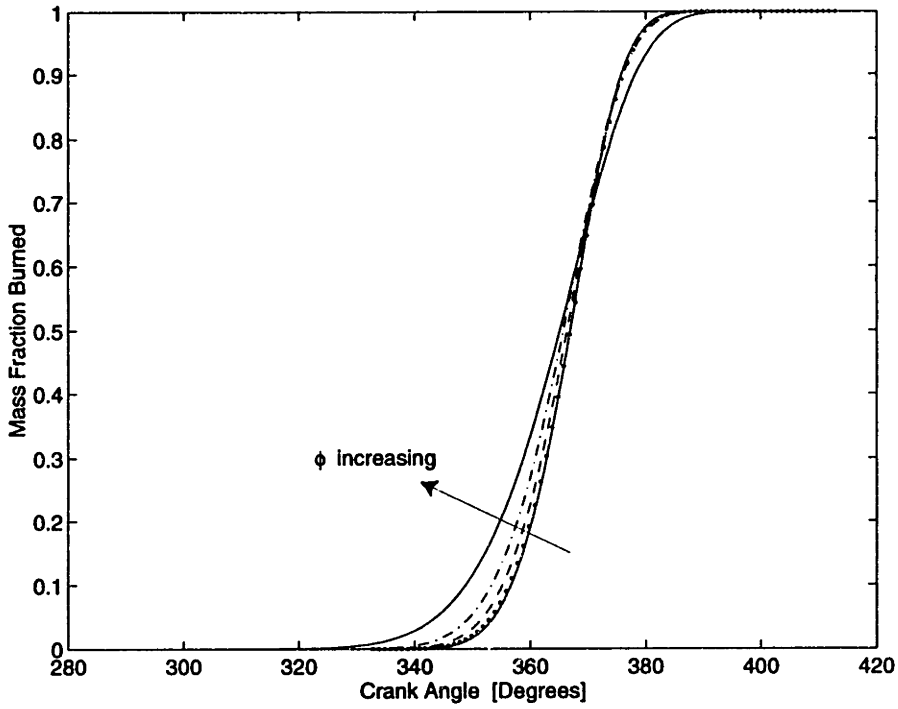

Figure 5.3: Burn Profile Variation with Equivalence Ratio

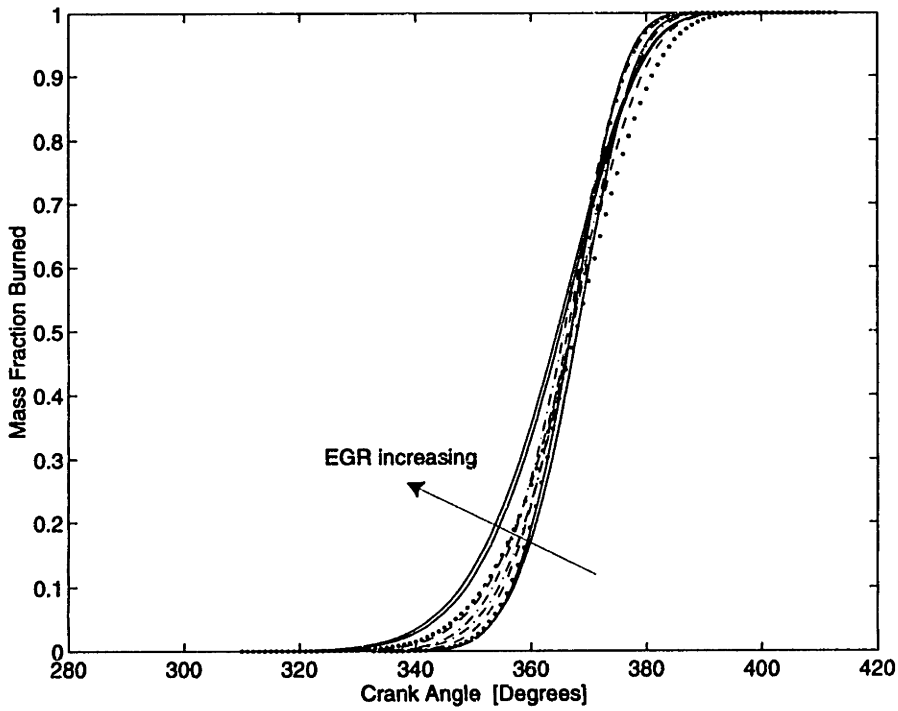

Figure 5.4: Burn Profile Variation with EGR

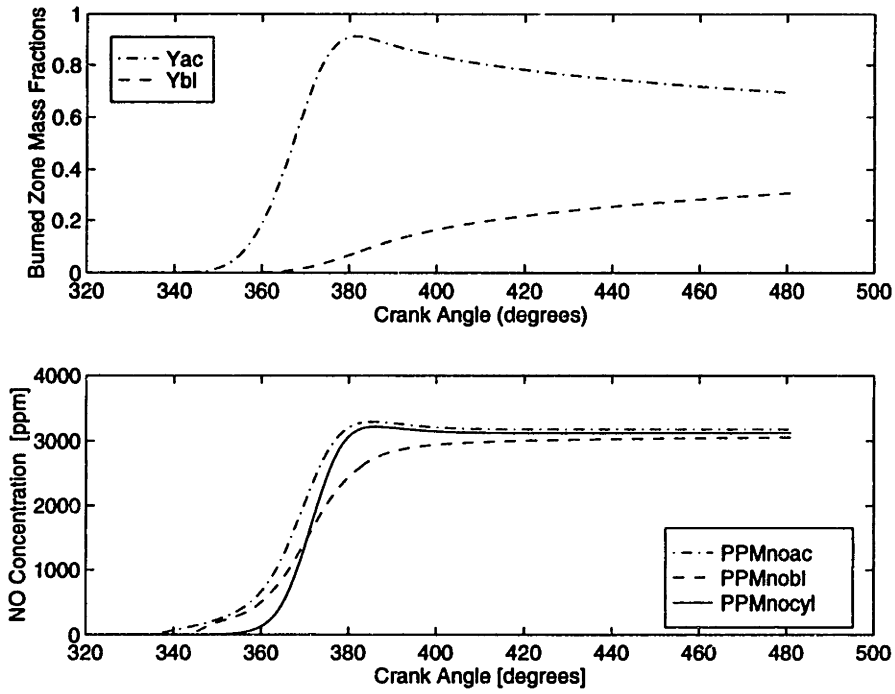

Figure 5.5: Adiabatic Core and Boundary Layer Model Results

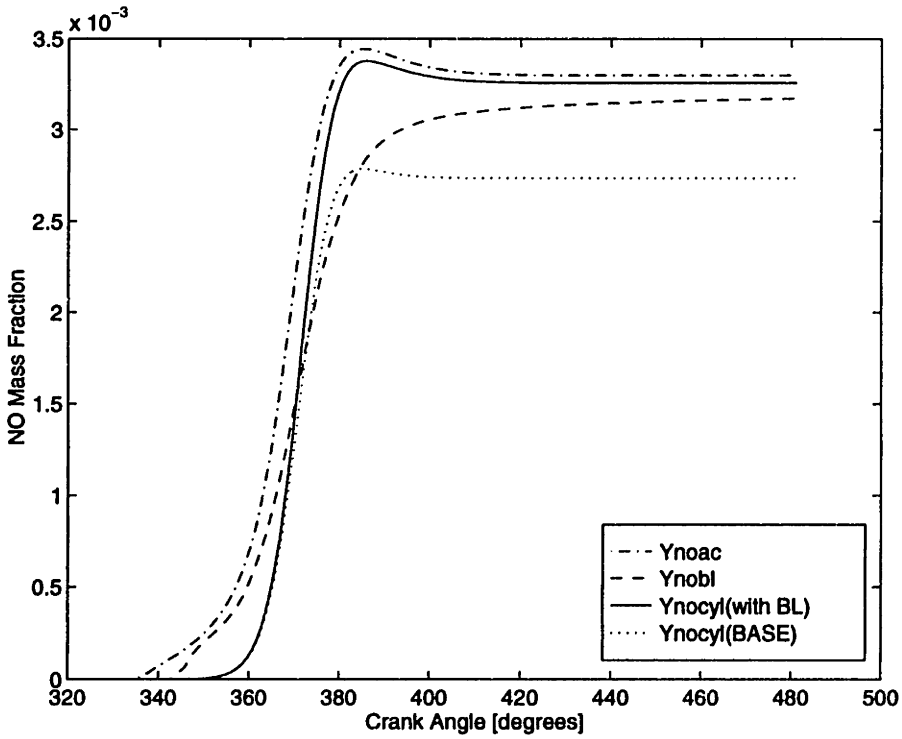

Figure 5.6: Comparison Between Base and Boundary Layer Model Results

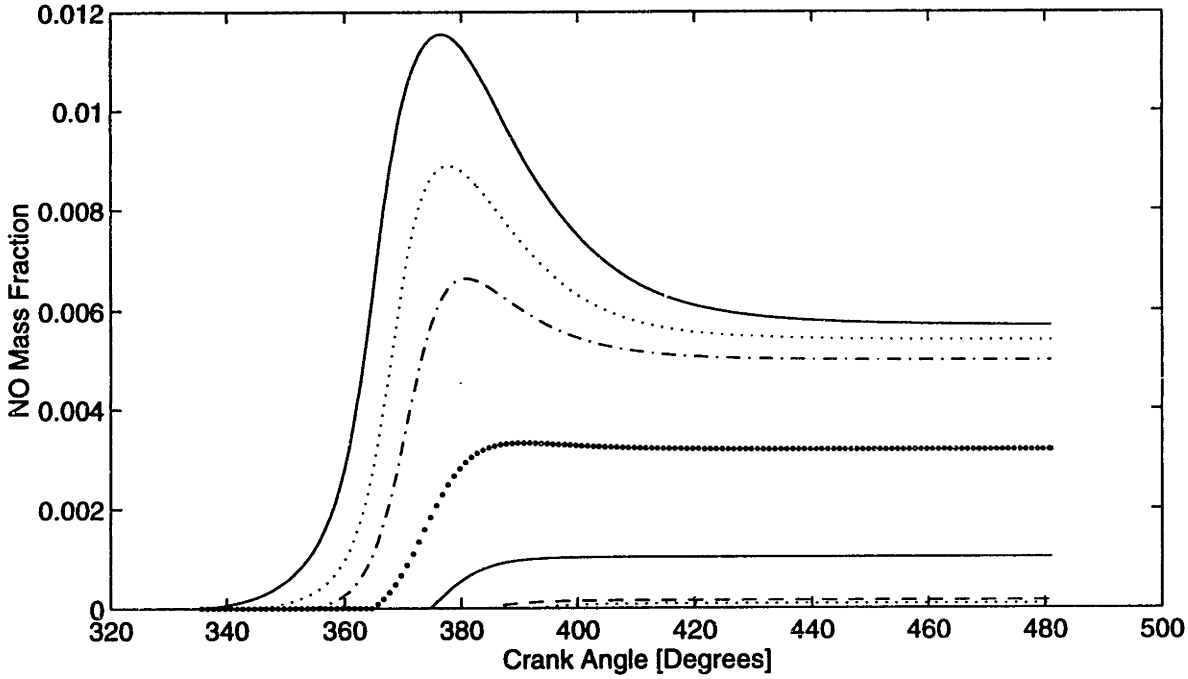

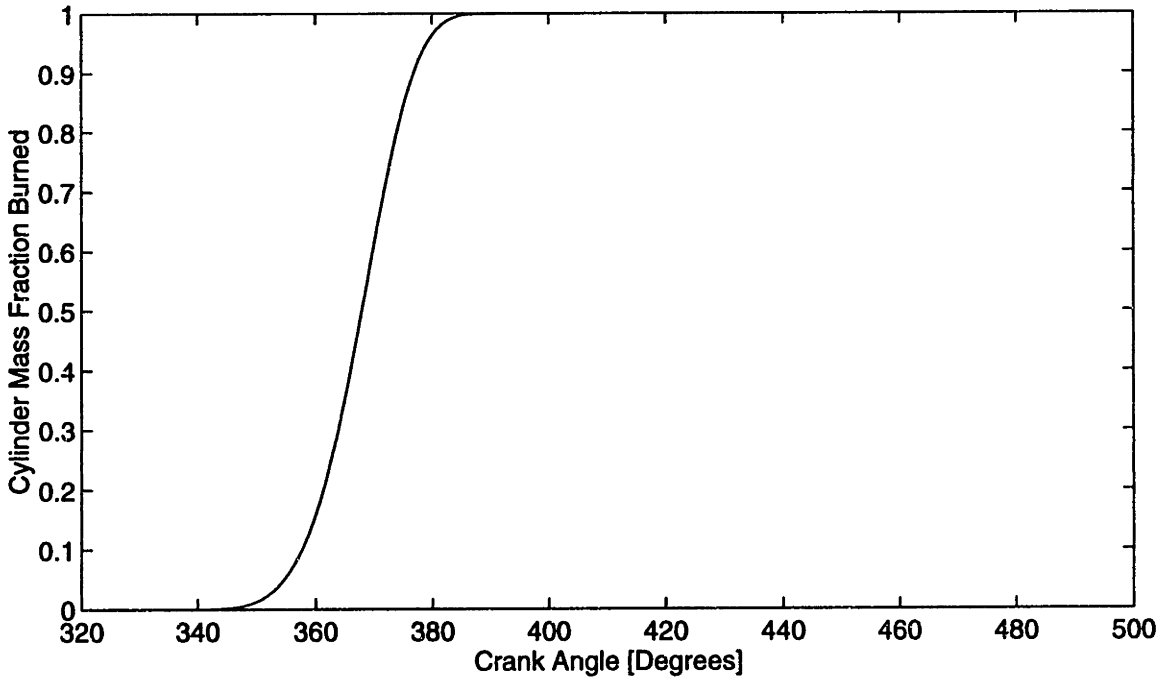

Figure 5.7: Layered Burn Model Results

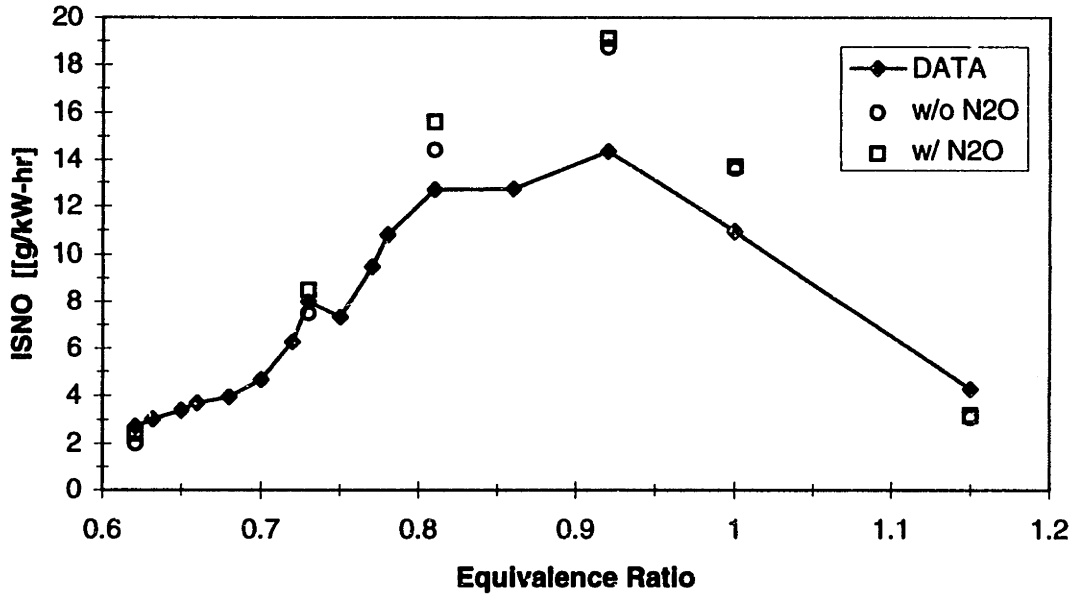

Figure 5.8: Complete Physical Model Computational NO Formation Results for cases with and without N_2O mechanism Over Equivalence Ratio

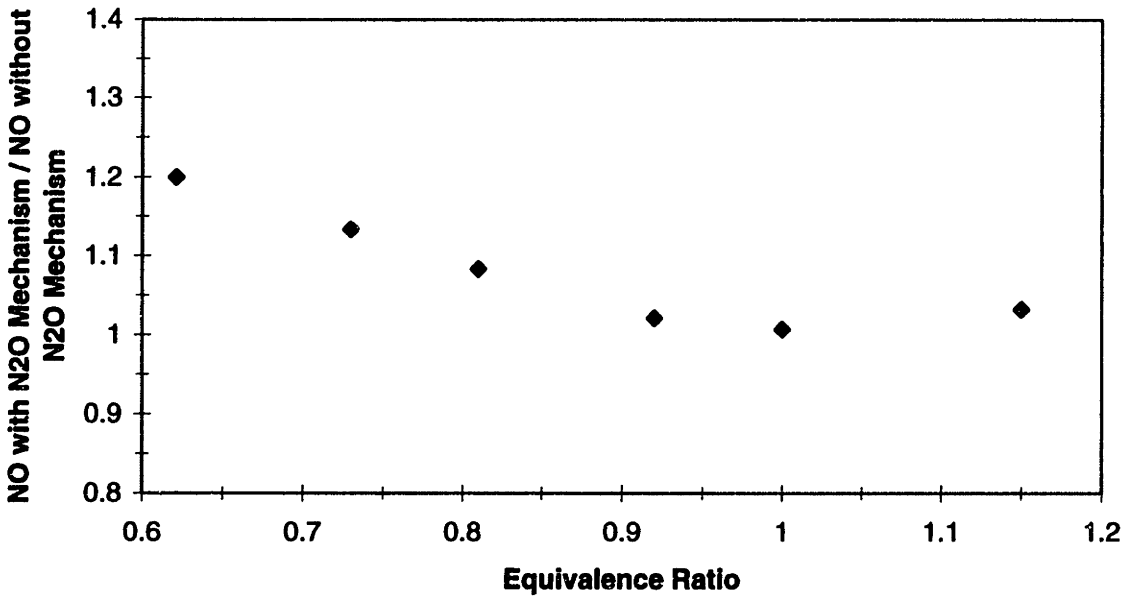

Figure 5.9: Effect of N_2O Mechanism with the Complete Physical Model Over Equivalence Ratio

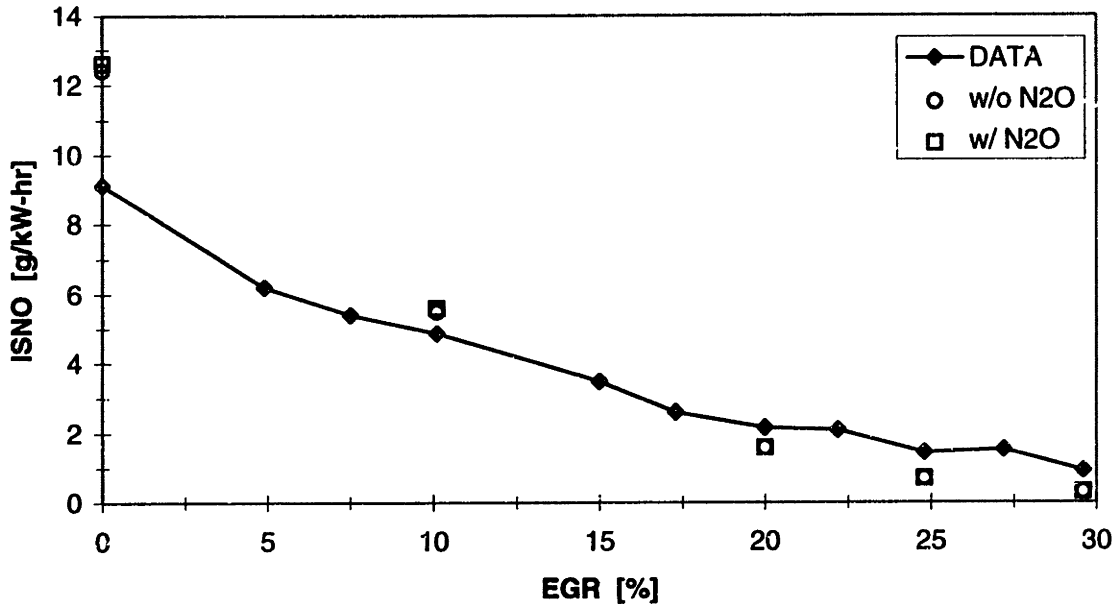

Figure 5.10: Effect of N_2O Mechanism with the Complete Physical Model Over EGR Sweep

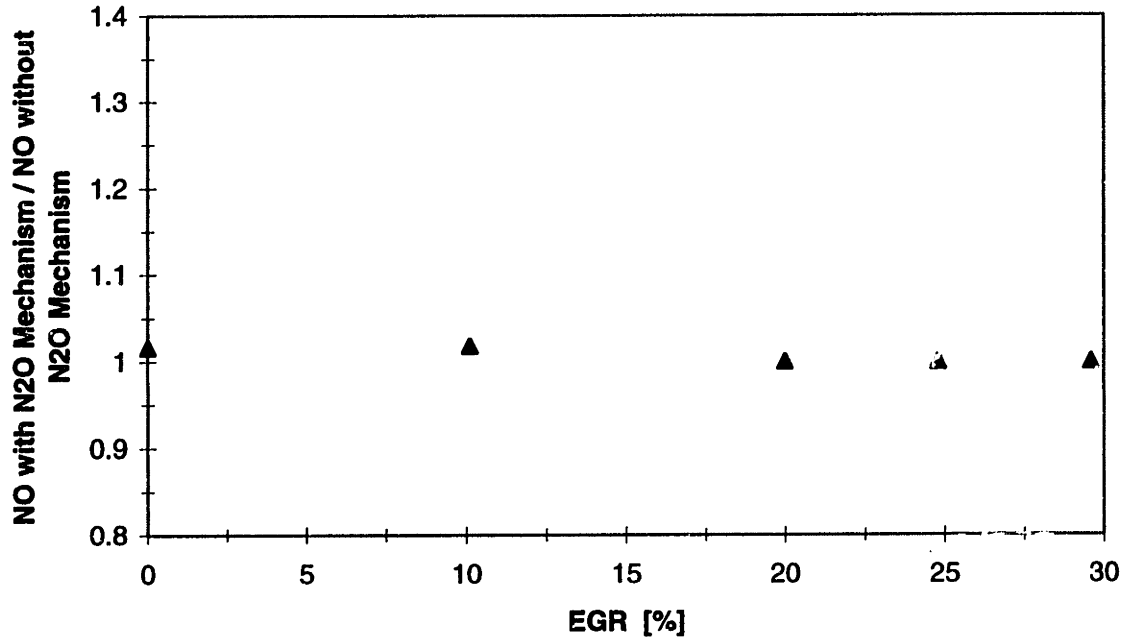

Figure 5.11: Effect of N_2O Mechanism with the Complete Physical Model Over EGR Sweep

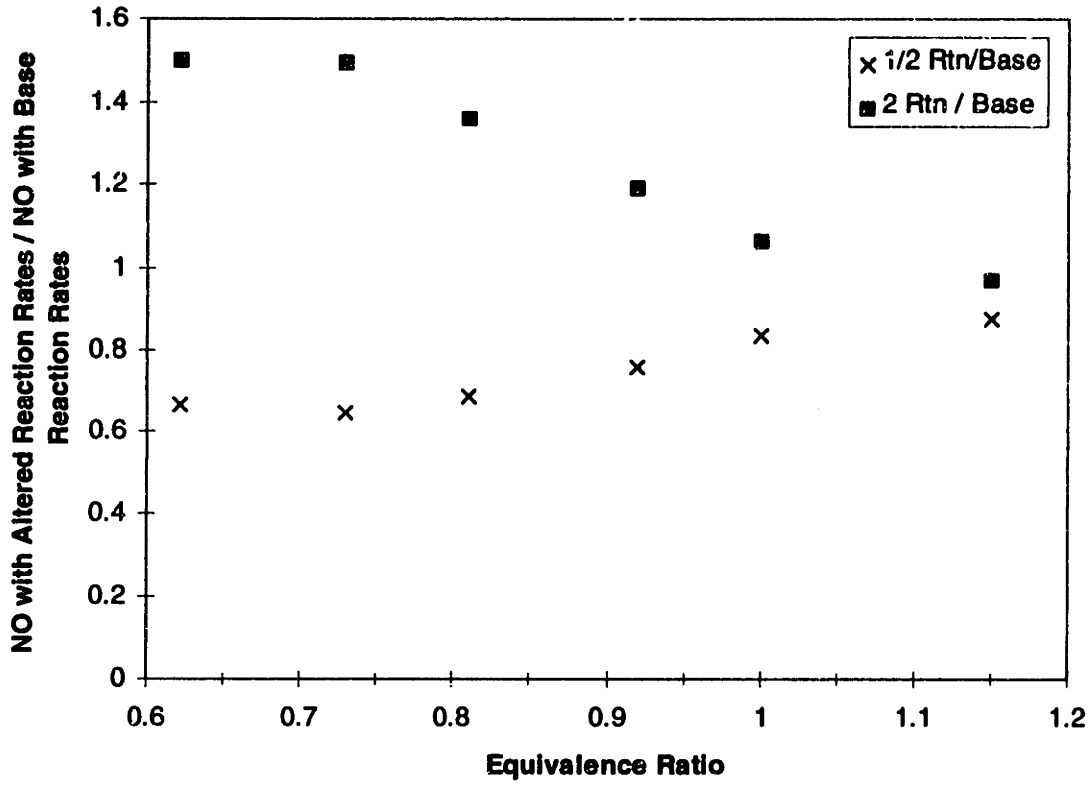

Figure 5.12: Effect of Changing the Reaction Rates for the Complete Thermal Zeldovich Mechanism over Equivalence Ratio, Using the Complete Physical Model

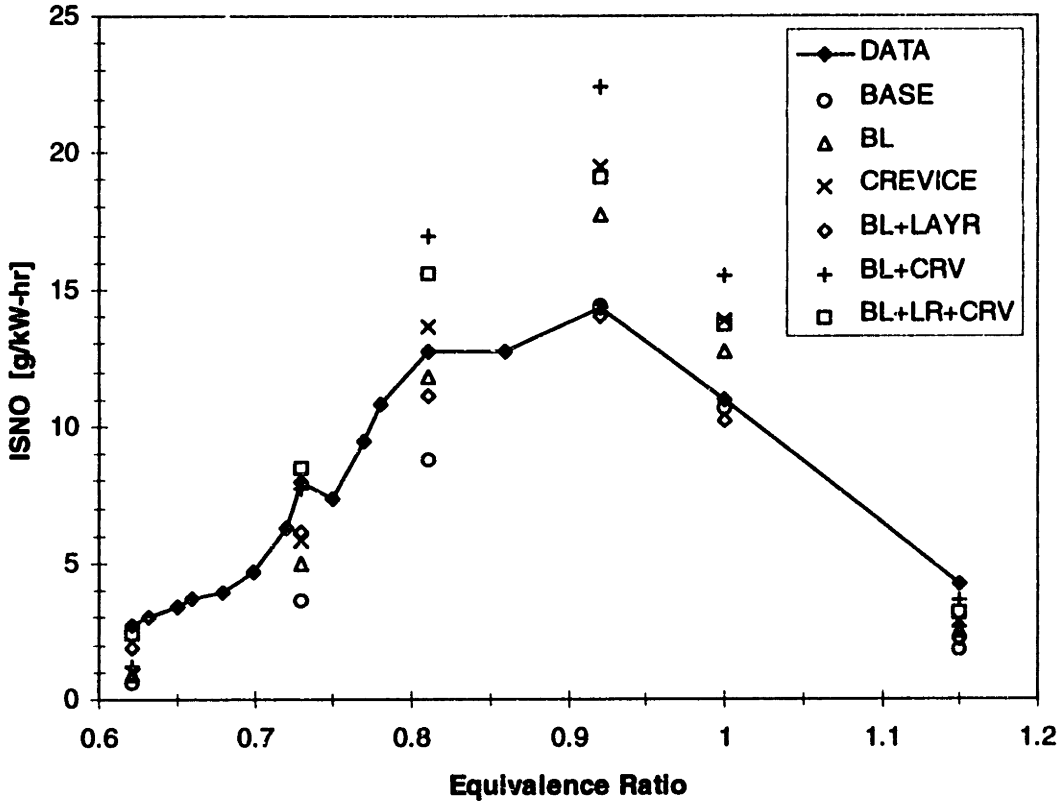

Figure 5.13: Impact of Enhanced physical modeling on NO predictions for the equivalence ratio sweep

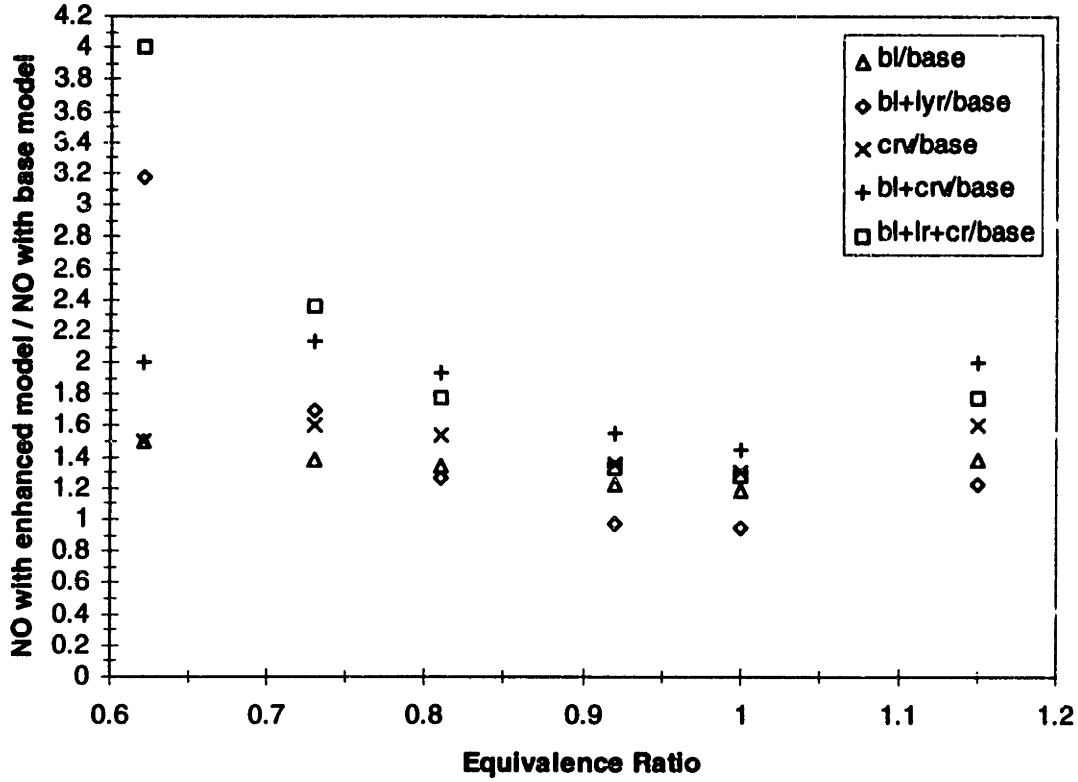

Figure 5.14: Sensitivity of NO Predictions to enhanced modeling over the equivalence ratio sweep

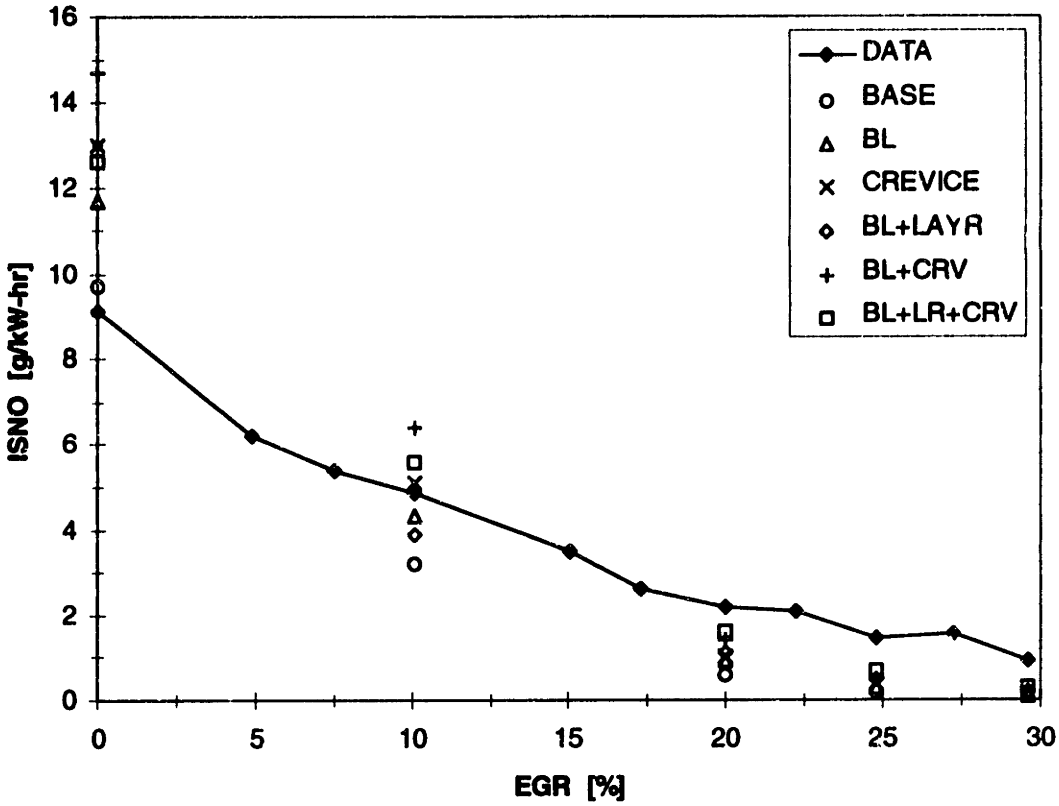

Figure 5.15: Impact of Enhanced physical modeling on NO predictions--EGR sweep

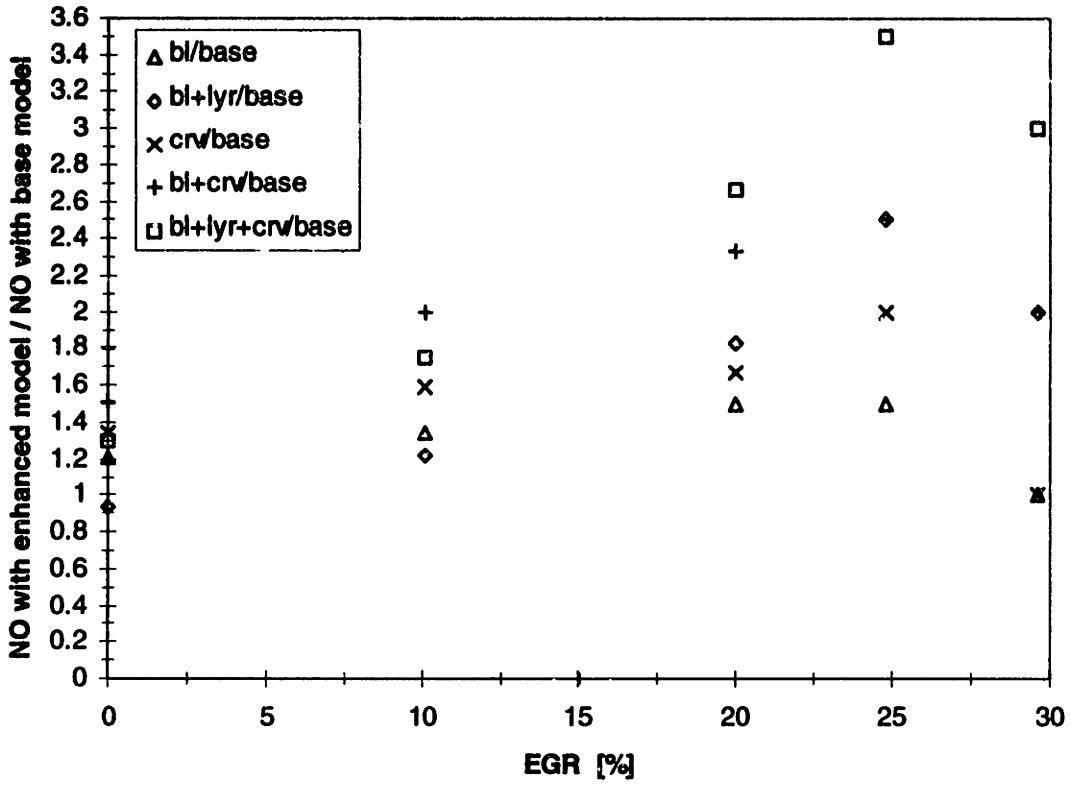

Figure 5.16: Sensitivity of NO Predictions to enhanced modeling over EGR

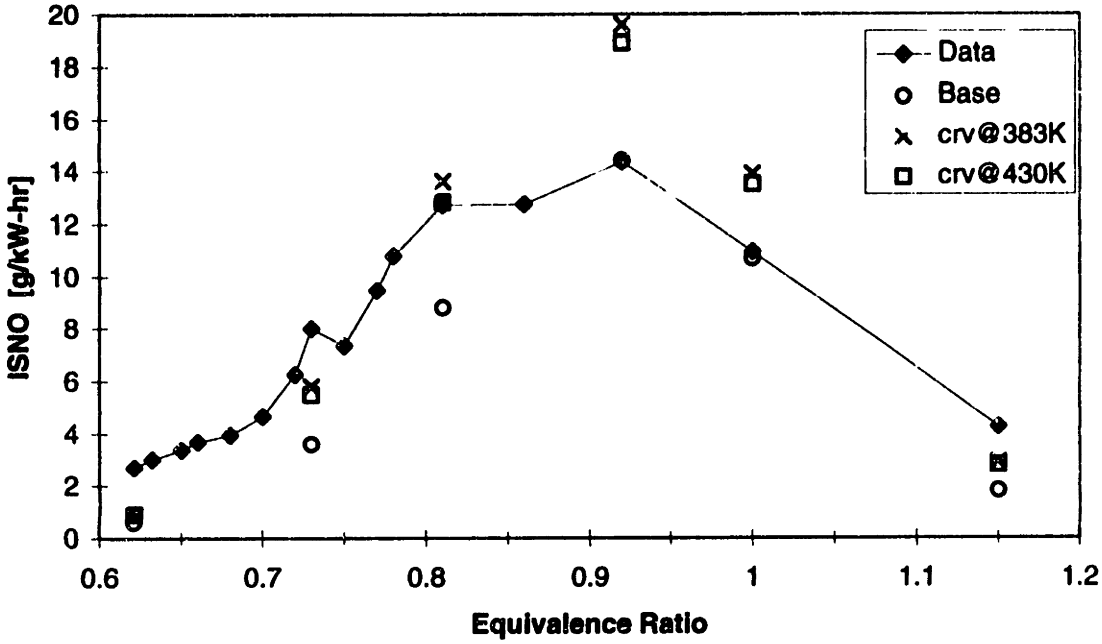

Figure 5.17: Impact of Crevice Gas Temperature on NO predictions

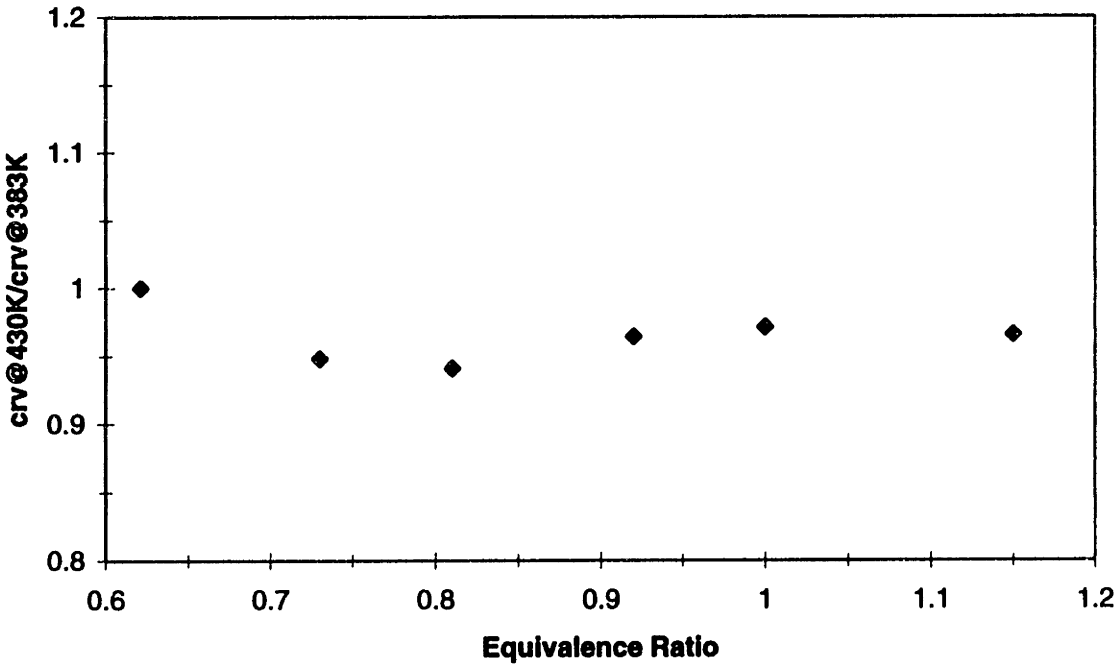

Figure 5.18: Sensitivity of NO Predictions to Crevice Gas Temperature

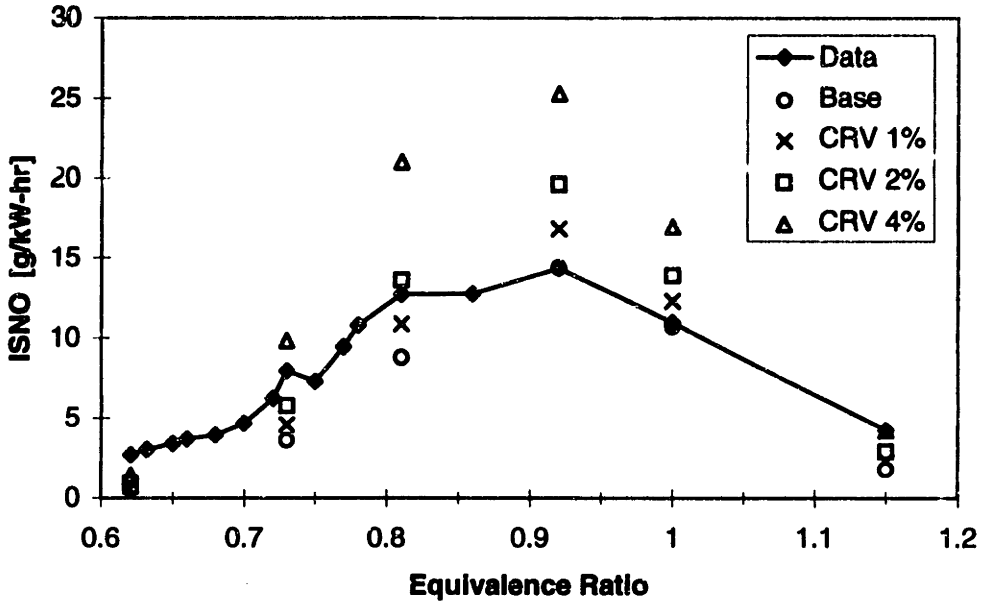

Figure 5.19: Impact of Crevice Volume on NO predictions

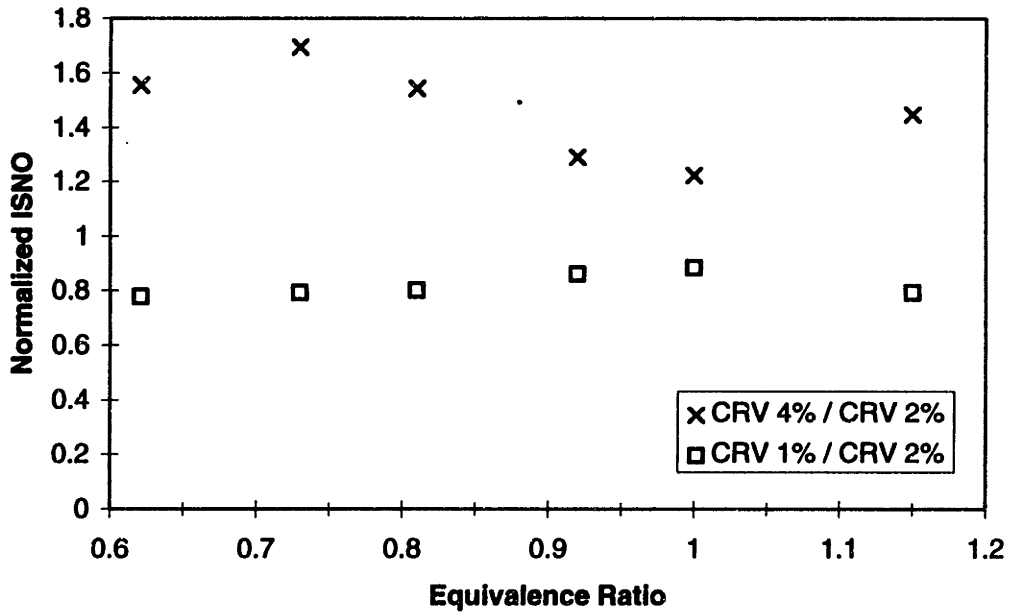

Figure 5.20: Sensitivity of NO Predictions to Crevice Volume

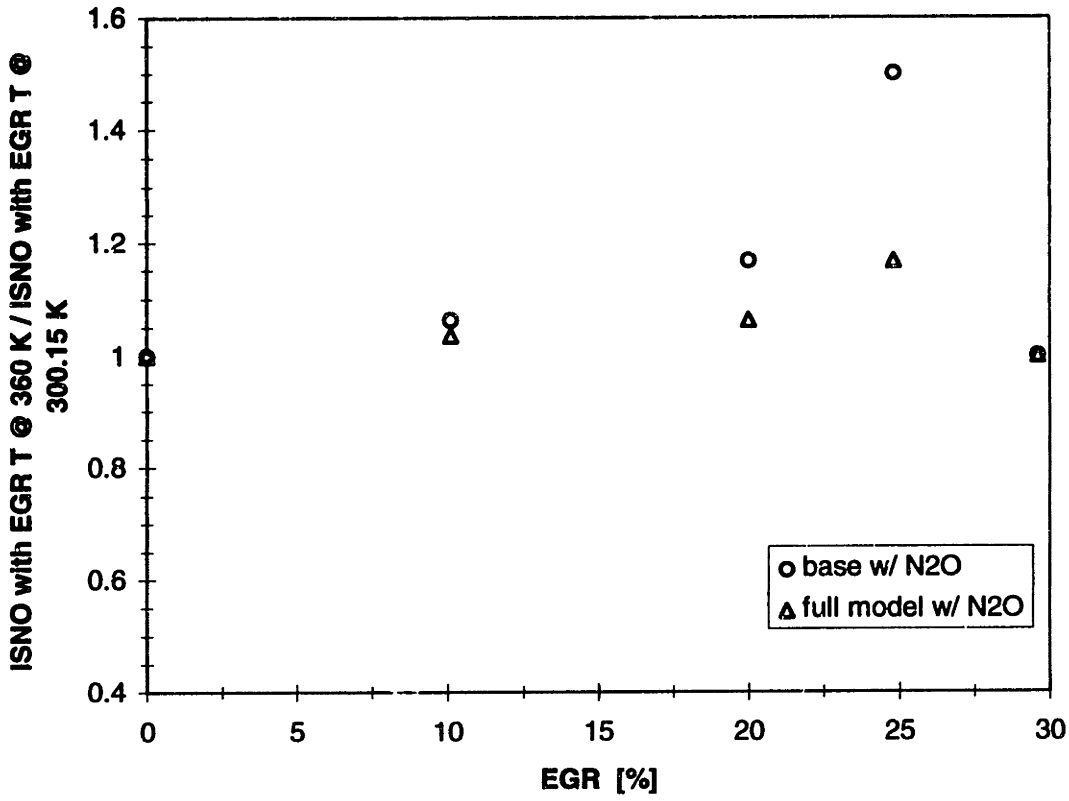

Figure 5.21: Sensitivity of NO Predictions to EGR Temperature

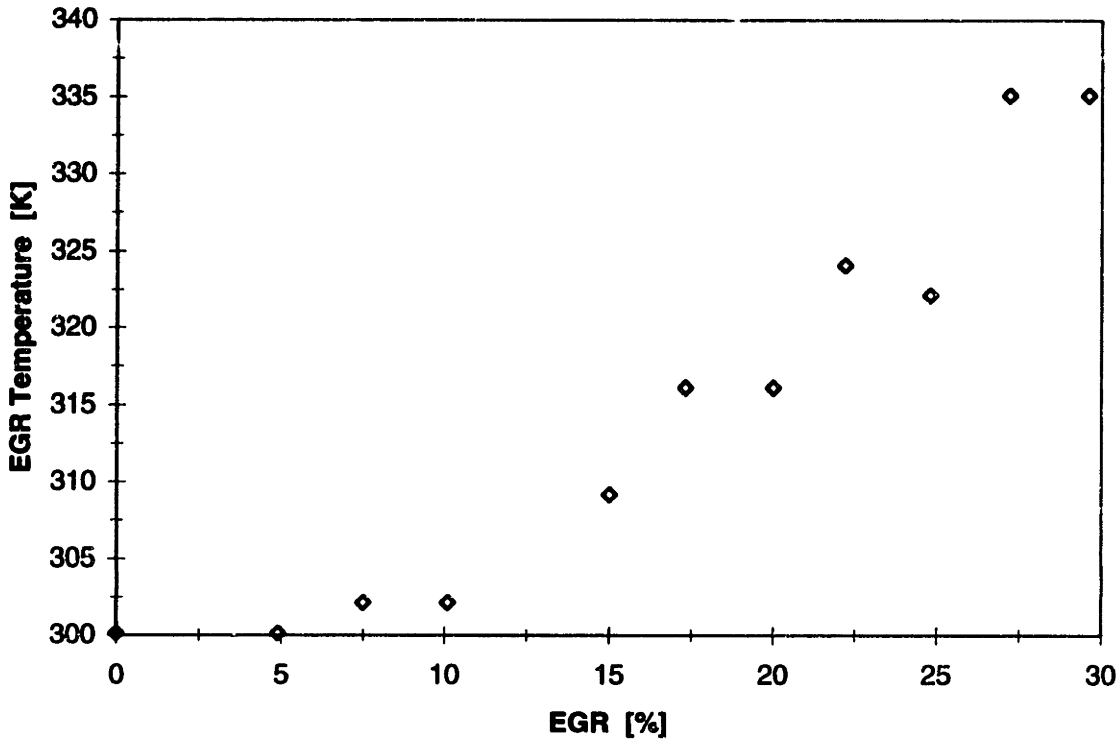

Figure 5.22: EGR Temperatures Matched in Computational Runs

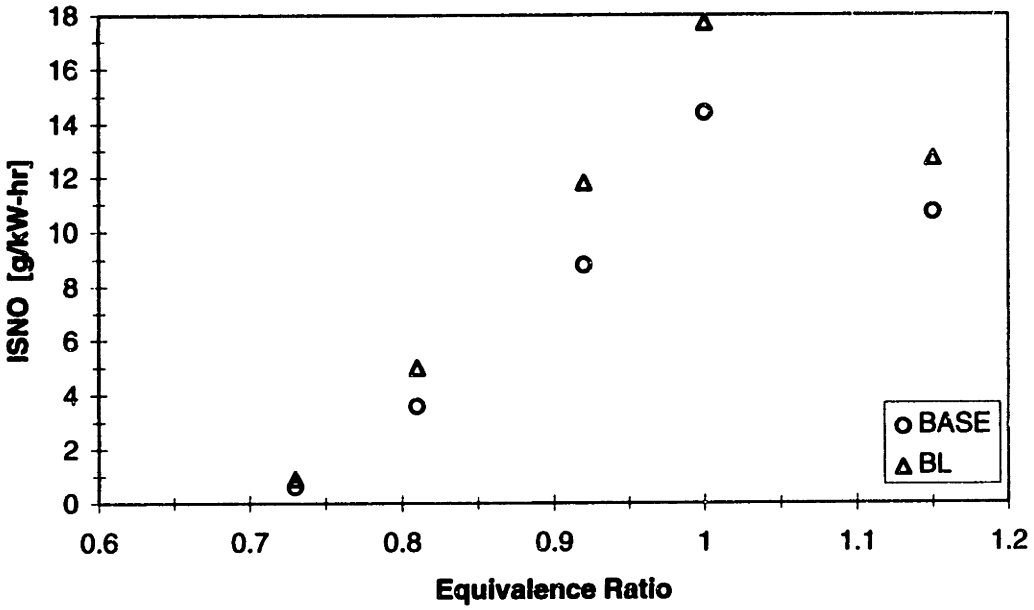

Figure 5.23: Effect of Boundary Layer/Adiabatic Core Model on NO predictions – Equivalence Ratio Sweep

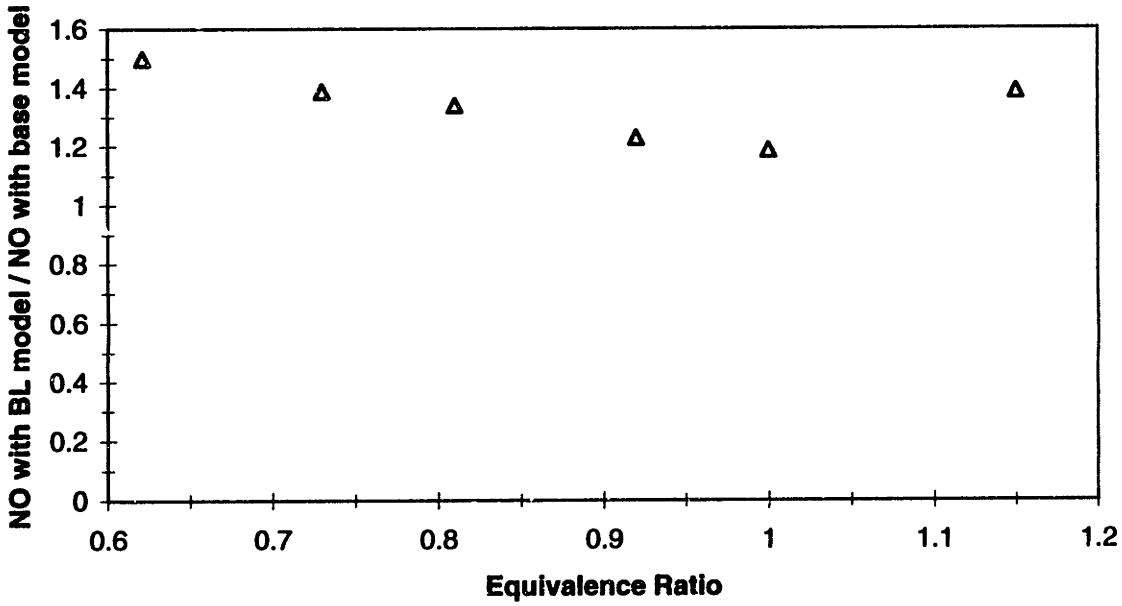

Figure 5.24: Sensitivity of NO Predictions to Boundary Layer/Adiabatic Core Model – Equivalence Ratio Sweep

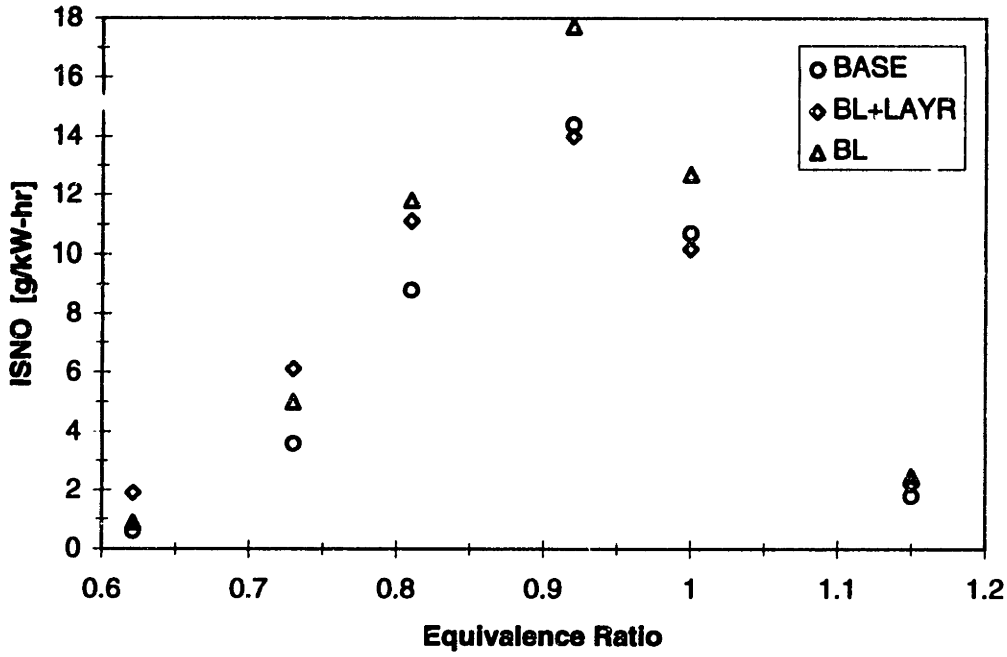

Figure 5.25: Effect of the Layered Burn and Boundary Layer Models on NO Predictions – Equivalence Ratio Sweep

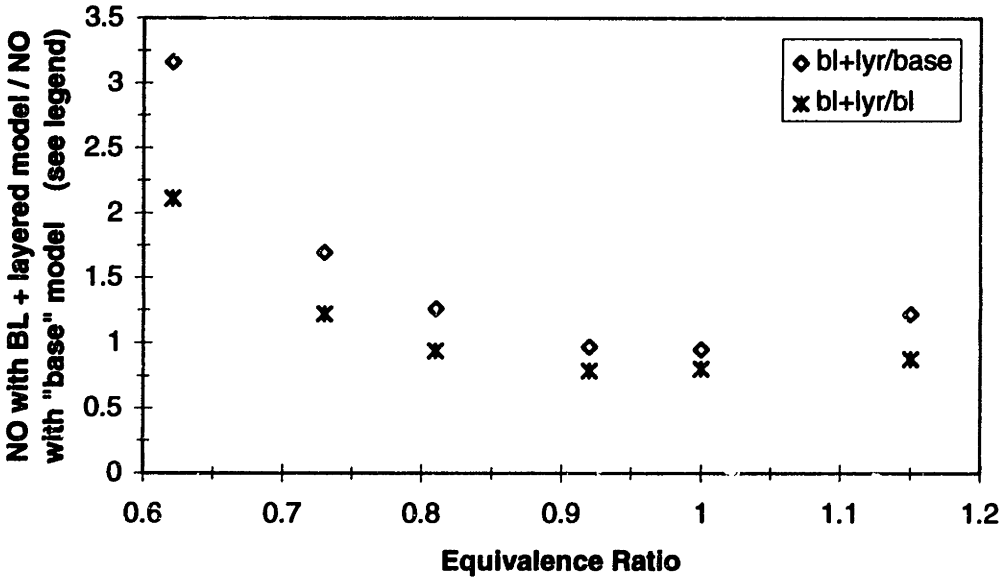

Figure 5.26: Sensitivity of NO Predictions to the Layered Burn and Boundary Layer Models – Equivalence Ratio Sweep

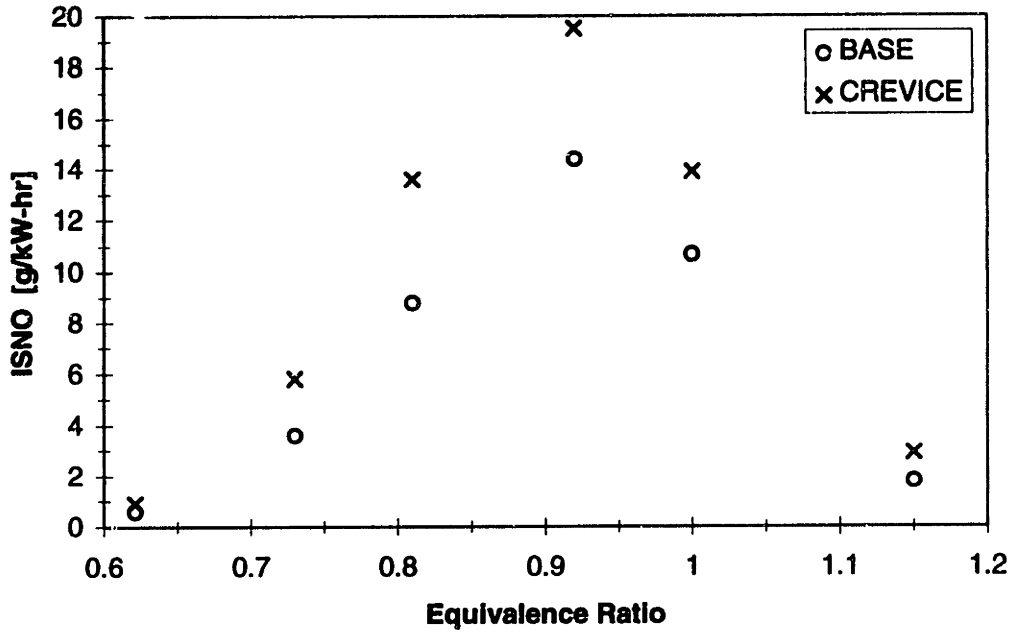

Figure 5.27: Effect of the Crevice Gas Model on NO Predictions – Equivalence Ratio Sweep

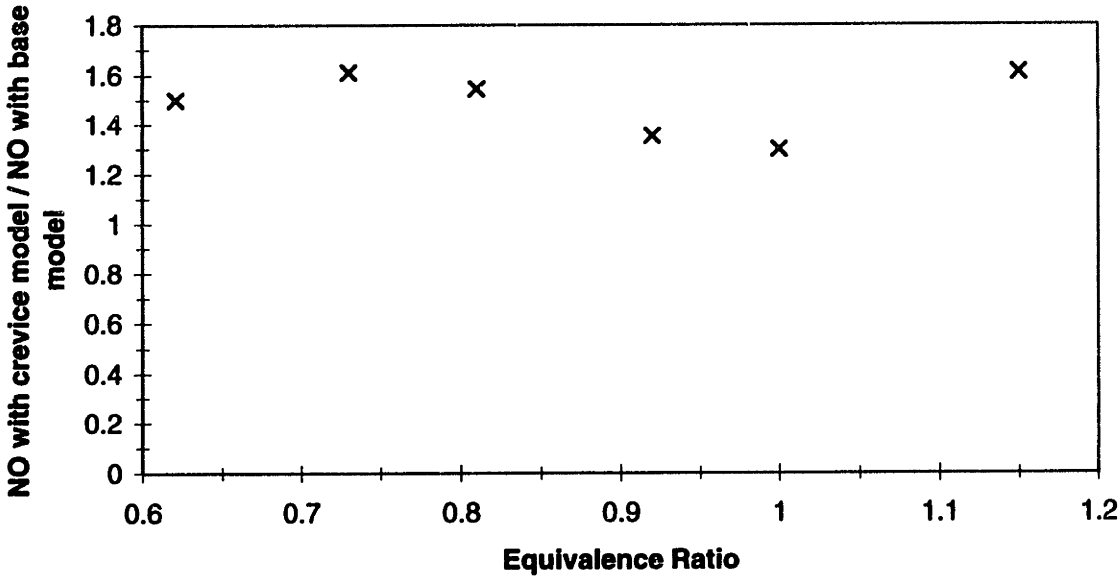

Figure 5.28: Sensitivity of NO Predictions to the Crevice Gas Model – Equivalence Ratio Sweep

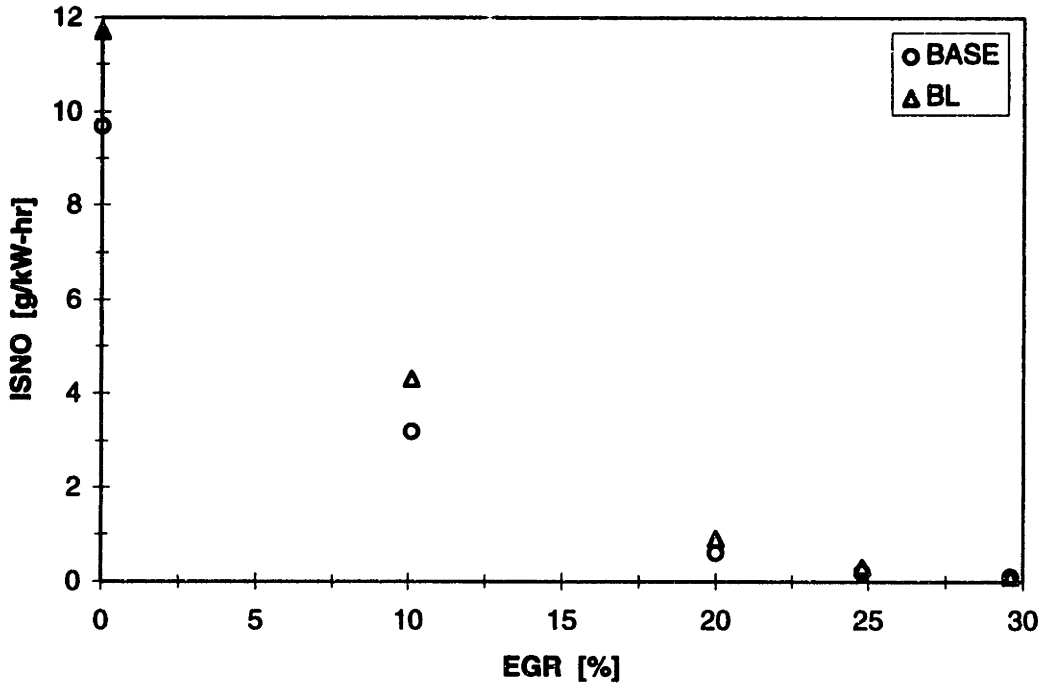

Figure 5.29: Effect of Boundary Layer/Adiabatic Core Model on NO predictions – EGR Sweep

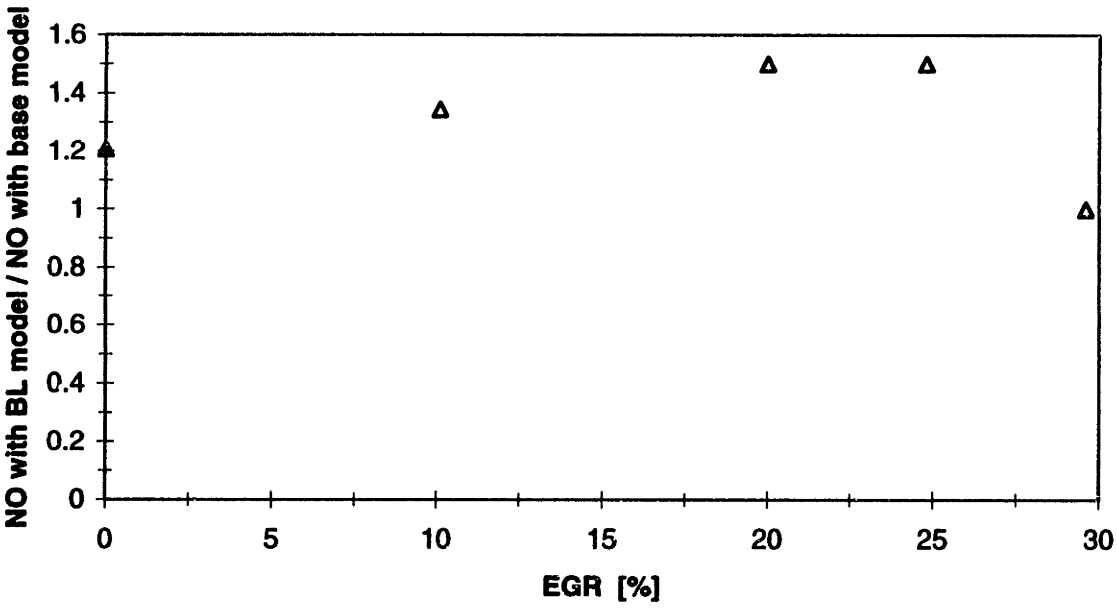

Figure 5.30: Sensitivity of NO Predictions to Boundary Layer/Adiabatic Core Model – EGR Sweep

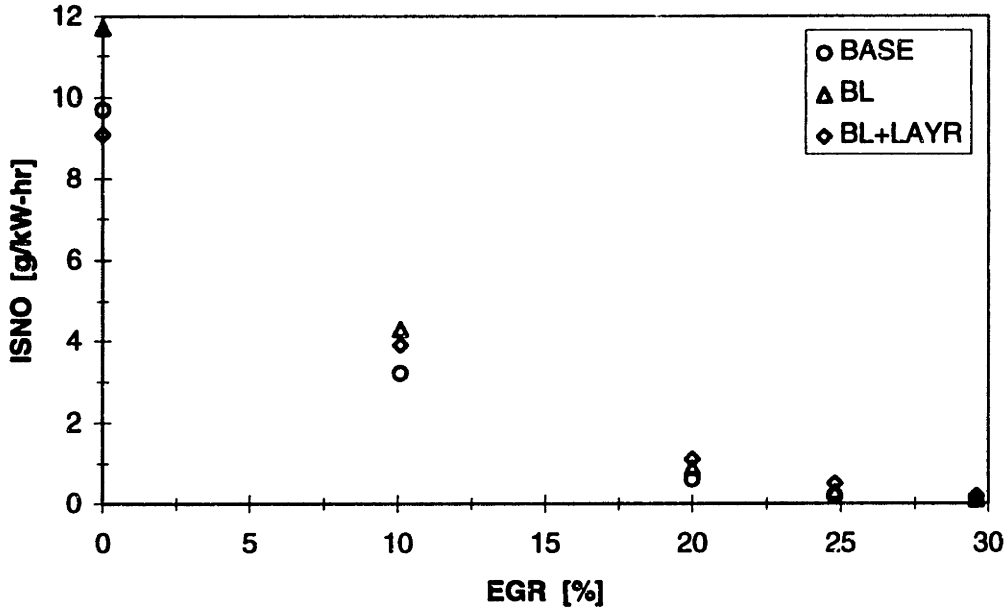

Figure 5.31: Effect of the Layered Burn and Boundary Layer Models on NO Predictions – EGR Sweep

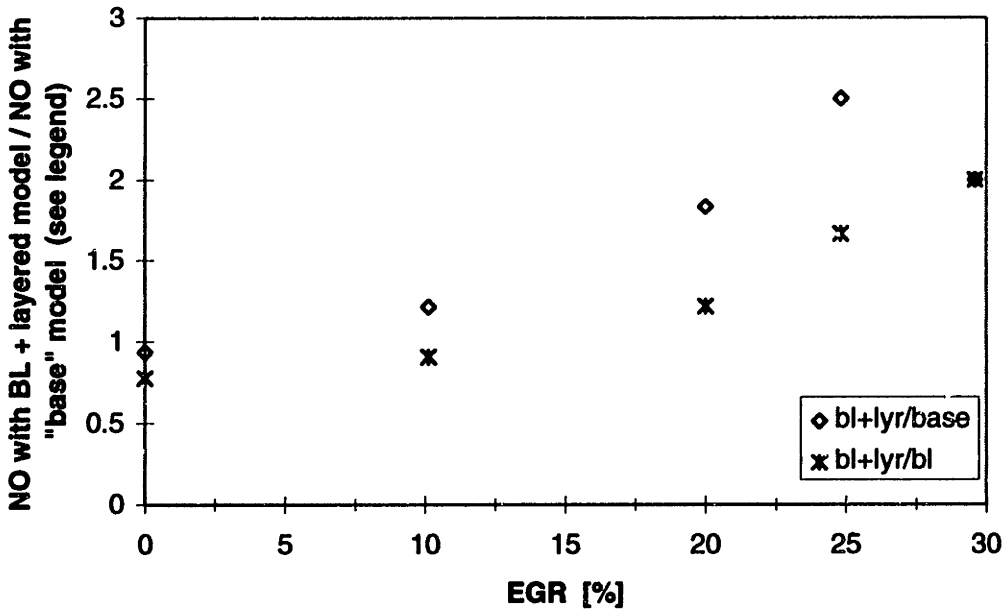

Figure 5.32: Sensitivity of NO Predictions to the Layered Burn and Boundary Layer Models – EGR Sweep

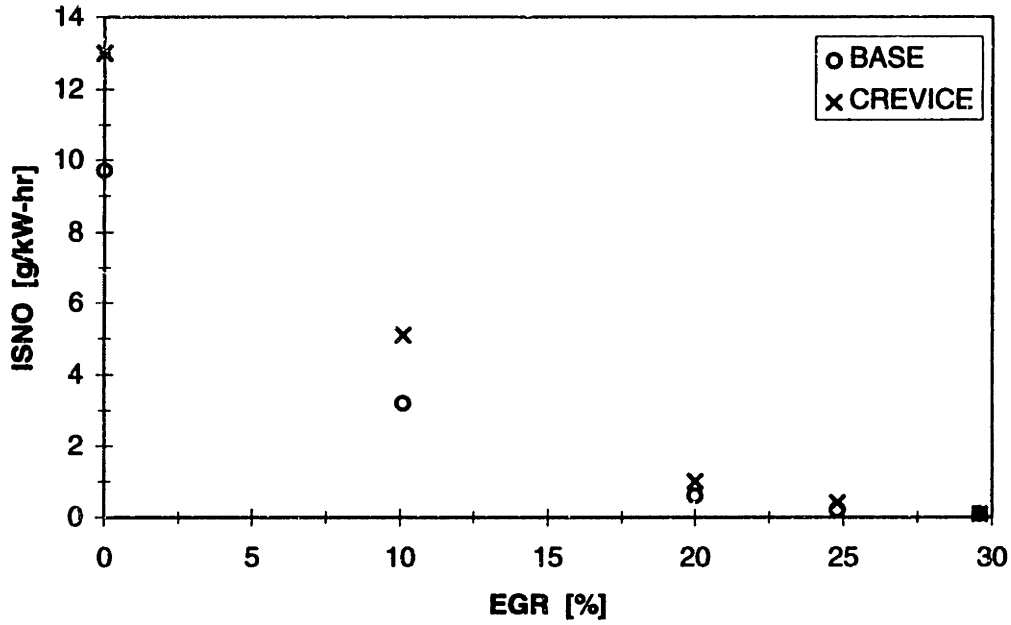

Figure 5.33: Effect of the Crevice Gas Model on NO Predictions – EGR Sweep

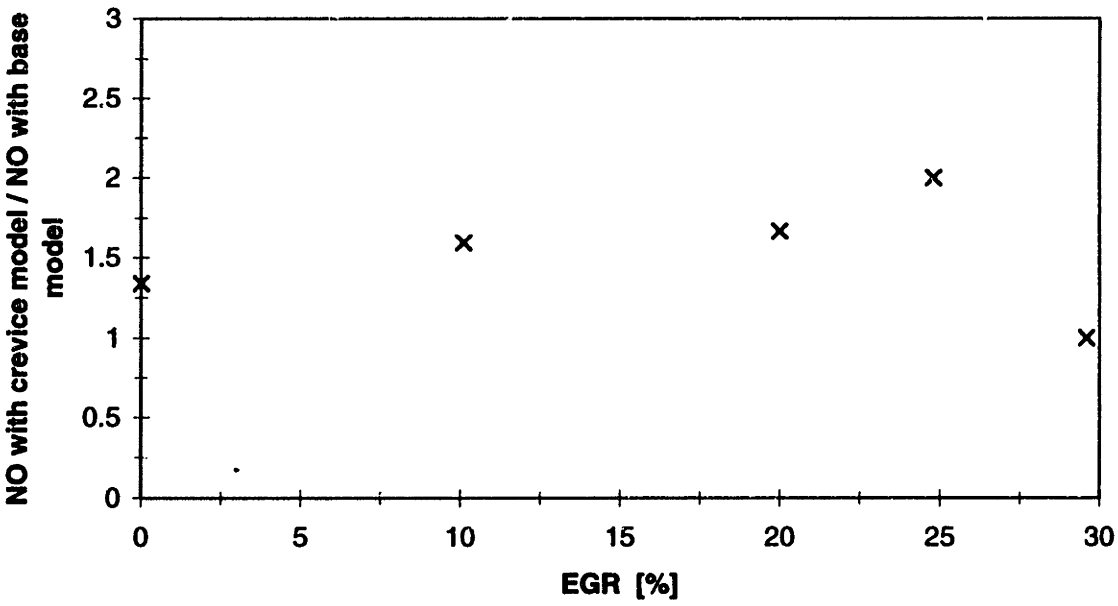

Figure 5.34: Sensitivity of NO Predictions to the Crevice Gas Model – EGR Sweep

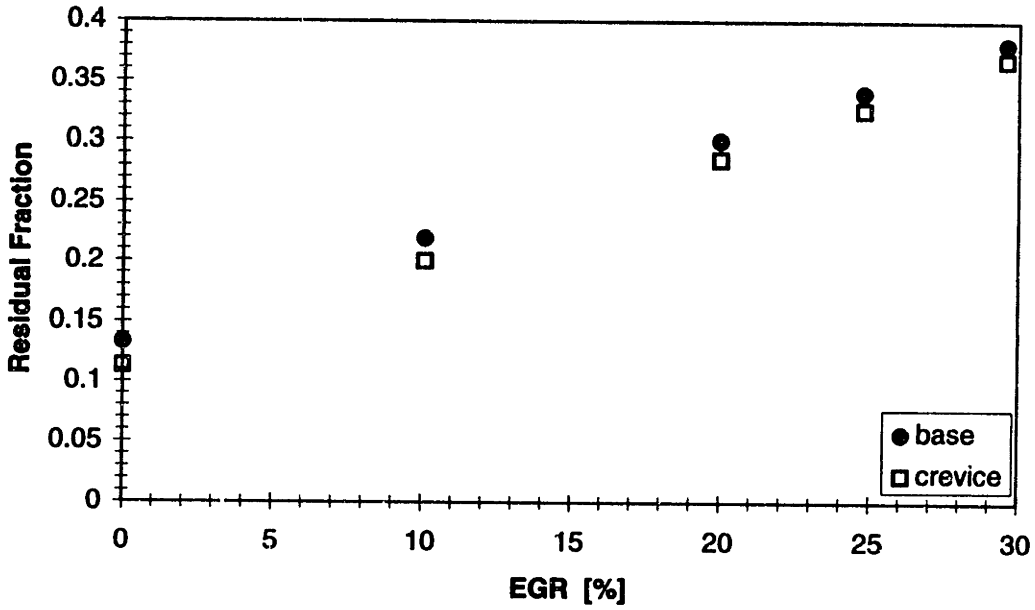

Figure 5.35: Residual Fraction Results using the crevice gas model and the base case – EGR sweep

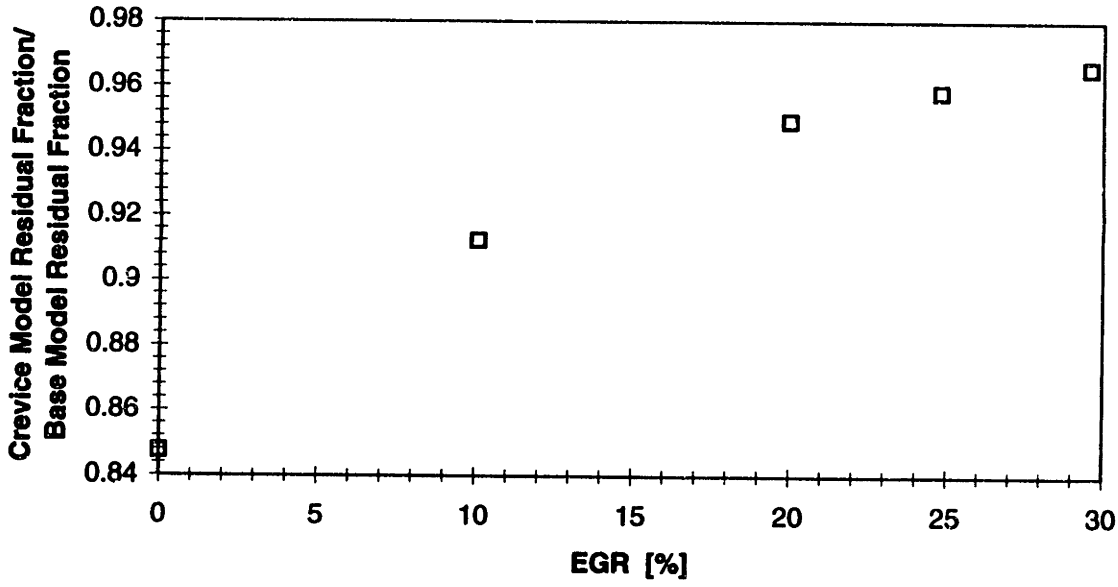

Figure 5.36: Comparison of residual fraction computations between those of the crevice gas model and the base case – EGR Sweep

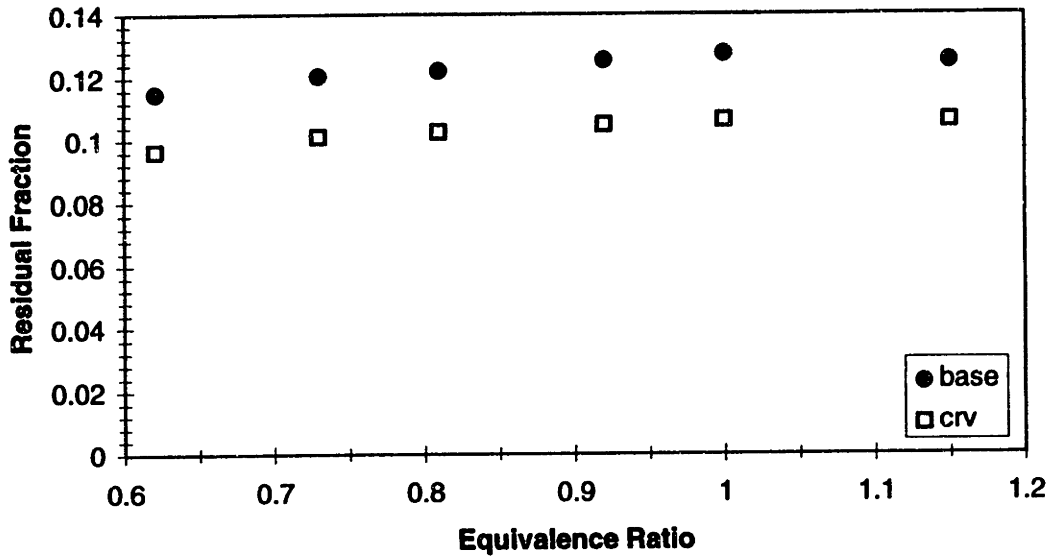

Figure 5.37: Residual Fraction Results using the crevice gas model and the base case – Equivalence Ratio sweep

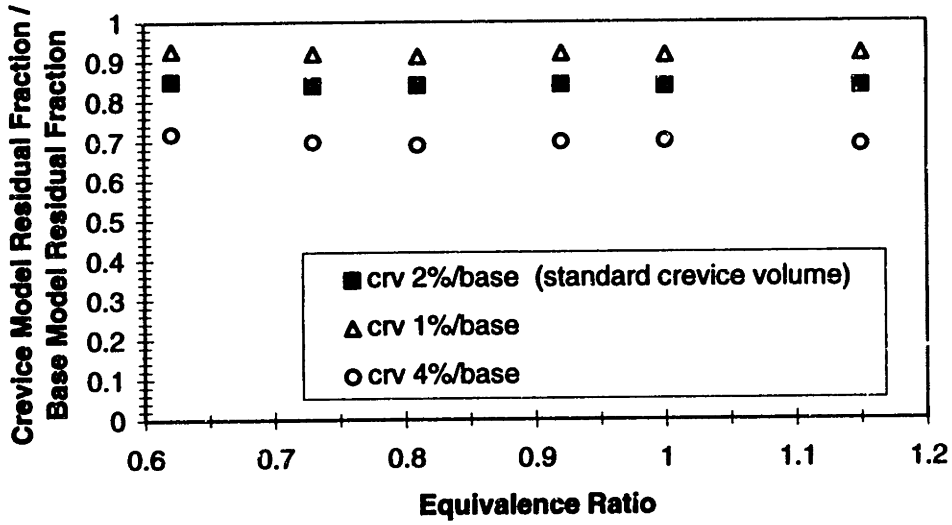

Figure 5.38: Comparison of residual fraction computations between those of the crevice gas model and the base case – Equivalence Ratio Sweep

6. Conclusions

6.1 Summary of Conclusions

Current spark ignition engine cycle simulation codes do not adequately predict NOx formation for automotive engine development and design purposes. Such computational models are critical in the automotive industry's successful response to the challenges of increasingly stringent Federal emissions regulations, time constraints imposed by heightened competition, and tighter budgets. The automotive industry requires a NOx generation model that provides accurate, reliable results over the complete range of engine operating conditions.

The framework which was developed in this thesis to improve NOx modeling addressed two critical factors of NOx formation: the "thermal state" of the engine in-cylinder burned gases and NOx chemical kinetics. The thermal boundary layer/adiabatic core, layered burn, and crevice gas models were used to improve the thermal state representation of the burned zone; chemical reactions and their associated rate constants were used to improve NOx formation chemistry.

The results may be summarized as follows:

1) The addition of the N_2O mechanism to the well established Zeldovich mechanism is only significant for very lean and dilute operation.

2) Rate constant uncertainty (of ± a factor of 2) causes NOx prediction uncertainty of approximately ±20%. The first reaction of the extended Zeldovich mechanism is most significant.

3) Adding additional physics to the simulation, through the boundary layer/adiabatic core, burned gas layering during combustion, and crevice models to account for fuel storage during combustion has a significant impact on NOx predictions and should be included. On average, it brings predictions significantly closer to data.

4) As NOx predictions are required to be more accurate, sensitivity of these predictions to model parameters will become increasingly important. Crevice volume was seen to be such a parameter. The primary effect of adding the crevice model is that at constant IMEP, the intake pressure must be increased so the residual gas concentration goes down.

5) Very lean and dilute conditions may require more sophisticated chemistry modeling of the flame region with its non-equilibrium radical concentrations.

6) Though the cycle simulation is still in its early stages of development, it has already proven its utility in design procedures. Two practical examples were presented.

6.2 Recommendations for Future Work

The next steps in the development of the cycle simulation as a design tool entail:

1) Integration of the enhanced models with the other physical models that impact these predictions. Specifically, a careful "matching" or "calibration" must be performed in order to properly assess the relationship of data to computational predictions for a particular engine.

2) Flame-zone chemistry modeling must be improved. This requires the evaluation and implementation of pertinent non-equilibrium flame chemistry, with particular attention to NO formation within the flame.

3) Further model validation against data should be undertaken that encompasses not only ultra lean and dilute, but also rich, operating points.

Bibliography

[1] Alkidas, A. C., Drew, R. J., and Miller, W. F., "Effects of Piston Crevice Geometry on the Steady-State Engine-Out Hydrocarbons Emissions of a S. I. Engine," SAE Paper 952537, 1995

[2] Benson, J. D. and Stebar, R. F., "Effects of Charge Dilution on Nitric Oxide Emission from a Single-Cylinder Engine," SAE Paper 710008, 1971.

[3] Blumberg, P. N., Lavoie, G. A., and Tabaczynski, R. J., "Phenomenological Models for Reciprocating Internal Combustion Engines," *Prog. Energy Combust. Sci.*, Vol. 5, pp. 123-167, 1979.

[4] Blumberg, P. and Kummer, J. T., "Prediction of NO Formation in Spark-Ignited Engines—An Analysis of Methods of Control," *Combustion Science and Technology*, Vol. 4, pp. 73-95, 1971.

[5] Blumberg, P. N., "Nitric Oxide Emissions From Stratified Charge Engines: Prediction and Control," *Combustion Science and Technology*, Vol. 8, pp. 5-24, 1973.

[6] Bowman, C. T., "Kinetics of Pollutant Formation and Destruction in Combustion," *Prog. Energy Combust. Sci.*, Vol. 1, pp. 33-45, 1975.

[7] Cheng, W. K., Hamrin, D., Heywood, J. B., Hochgreb, S., Kyoungdoug, M., Norris, M., "An Overview of Hydrocarbon Emissions Mechanisms in Spark-Ignition Engines," SAE Paper 932708, 1993.

[8] Crandall, R.W., et al., Regulating the Automobile, The Brookings Institution, Washington D.C., 1986.

[9] Dai, W., Davis, G. C., Hall, M. J., and Matthews, R. D., "Diluents and Lean Mixture Combustion Modeling for SI Engines with a Quasi-Dimensional Model," SAE paper 952382, 1995.

[10] Eyzat, P. and Guilbet, J. C., "A New Look at Nitrogen Oxides Formation in Internal Combustion Engines," SAE Paper 680124, 1968.

[11] Flagan, R.C. and Seinfeld, J.H., Fundamentals of Air Pollution Engineering, Prentice-Hall, Inc., Englewood Cliffs, New Jersey, 1988.

[12] Hamrin, D. A., and Heywood, J. B., "Modeling for Engine-Out Hydrocarbon Emissions for Prototype Production Engines," SAE Paper 950984, 1995.

[13] Heywood, J. B. and Keck, J. C., "Formation of Hydrocarbons and Oxides of Nitrogen in Automobile Engines," *Environmental Science and Technology*, Vol. 7, pp. 216-222, 1973.

[14] Heywood, J. B. and Watts, P. A., "Parametric Studies of Fuel Consumption and NO Emissions of Dilute Spark-Ignition Engine Operation Using a Cycle Simulation," *I. Mech. E.*, pp. 117-127, 1979.

[15] Heywood, J. B., "How Clean A Car?," *Technology Review*, Vol. 73, 1971.

[16] Heywood, J. B., Internal Combustion Engine Fundamentals, McGraw-Hill Book Co., New York, 1988.

[17] Hires, S. D., Ekchian, A., Heywood, J. B., Tabaczynski, R. J. and Wall, J. C., "Performance and NOx Emissions Modeling of a Jet Ignition Prechamber Stratified Charge Engine," SAE Paper 760161, 1976.

[18] Hulls, T. A. and Nickol, H. A., "Influence of Engine Variables on Exhaust Oxides of Nitrogen Concentrations from a Multi-Cylinder Engine," SAE Paper 670482, 1967.

[19] Komiyama, K. and Heywood, J. B., "Predicting NOx Emissions and Effects of Exhaust Gas Recirculation in Spark-Ignition Engines," SAE Paper 730475., 1973.

[20] Lavoie, G. A., and Blumberg, P. N., "A Fundamental Model for Predicting Fuel Consumption, NOx and HC Emissions of the Conventional Spark-Ignited Engine," *Combustion Science and Technology*, Vol. 21, pp. 225-258, 1980.

[21] Lavoie, G. A., and Blumberg, P. N., "Measurements of NO Emissions From a Stratified Charge Engine: Comparison of Theory and Experiment," *Combustion Science and Technology*, Vol. 8, pp. 25-37, 1973.

[22] Lavoie, G. A., Heywood, J. B., and Keck, J. C., "Experimental and Theoretical Study of Nitric Oxide Formation in Internal Combustion Engines," *Combustion Science and Technology,* Vol. 1, pp. 313-326, 1970.

[23] Martin, M. K. and Heywood, J. B., "Approximate Relationships for the Thermodynamic Properties of Hydrocarbon-Air Combustion Products," *Combustion Science and Technology,* Vol. 15, pp. 1-9, 1976.

[24] McLellan, D.R., "The Automobile Industry and Government: Their Perceptions Of One Another and the Influence This Has On Public Policy," S.M. Thesis, Massachusetts Institute of Technology, 1974.

[25] Miller, J.A. and Bowman, C.T., *Prog. Ener. Combust. Sci.*, Vol 15. Pgs. 287-338, 1989.

[26] Min, K. and Cheng, W. K., "In-Cylinder Oxidation of Piston-Crevice Hydrocarbon in SI Engines," The Third International Symposium on Diagnostics and Modeling of Combustion in Internal Combustion Engines, 1994.

[27] Namazian, M. and Heywood, J. B., "Flow in the Piston-Cylinder-Ring Crevices of a Spark-Ignition Engine: Effect on Hydrocarbon Emissions, Efficiency, and Power," SAE Paper 820088, 1982.

[28] Norman, T. J., "A Performance Model of a Spark-Ignition Wankel Engine: Including the Effects of Crevice Volumes, Gas Leakage, and Heat Transfer," S. M. Thesis, Massachusetts Institute of Technology, 1983.

[29] Poulos, S.G., "The Effect of Combustion Chamber Geometry On S.I. Engine Combustion Rates – A Modeling Study, " S. M. Thesis, Massachusetts Institute of Technology, 1982.

[30] Poulos, S. G. and Heywood, J. B., "The Effect of Chamber Geometry on Spark-Ignition Engine Combustion," SAE Paper 830334, 1983.

[31] Prigent, M. and De Soete, G., "Nitrous Oxide N2O in Engines Exhaust Gases—A First Appraisal of Catalyst Impact," SAE Paper 890492, 1989.

[32] Quader, A. A., "Why Intake Charge Dilution Decreases Nitric Oxide Emission from Spark Ignition Engines," SAE Paper 710009, 1971.

[33] Quader, A. A., "Effects of Spark Location and Combustion Duration on Nitric Oxide and Hydrocarbon Emissions," SAE Paper 730153, 1973.

[34] Raine, R. R., Stone, C. R. and Gould, J., "Modeling of Nitric Oxide Formation in Spark Ignition Engines with a Multizone Burned Gas," *Combustion and Flame*, Vol. 102, pp. 241-255, 1995.

[35] Roberts, J. A., Norman, T. J., Ekchian, J. A., Heywood, J. B., "Computer Models for Evaluating Premixed and Disc Wankel Engine Performance," SAE Paper 860613, 1986.

[36] Rose, Frederick. "California Eases Environmental Rules For Introduction of Zero-Emission Autos". *The Wall Street Journal*, April 1, 1996.